Cocrystals, salts and eutectics of anti-tuberculosis medicines

Tsebang Alice Matlapeng

Dissertation presented for the degree of Master of Science
in the Department of Chemistry
Rhodes University

February 2024

Supervisor: Dr V. Smith
Co-supervisors: Prof R.B. Walker and
Dr T. Geswindt

Table of contents

Additional files (.sup files) for crystallographic structures can be found on the following Google drive link and can be viewed on notepad: https://drive.google.com/drive/folders/1-2ZdIPODx7JTDR2NW-cpvdFSRxscRySL?usp=sharing

The files have been named the same way as the structures have been referred to in the dissertation.

ACKNOWLEDGEMENTS

A special thanks to my supervisor, Dr Vincent J. Smith, for his academic, emotional and financial support throughout this journey, from *"start to finish,"* and for guiding me through the data interpretation and image preparation.

My co-supervisors:
Prof R.B. Walker, thank you so much for supplying the anti-TB API and for constantly asking "so what's new?" It certainly inspired me to work hard so that I had something to report to you every time we met. Dr T. Geswindt, thank you for your support, academic, emotional, and financial. I really appreciate it and you.

Profs Watkins and Krause thank you for your advice and interest in this work and for listening attentively during our group meetings.

Dr Baa thank you for being a mentor during this research, helping with single crystal X-ray data collections and providing insightful feedback while writing this dissertation. Patience Matsika for your contribution in the work.

I am immensely grateful to my family for their love, support, for constantly having my back and supporting my dreams.

To my sister, '*Manapo Margret Maoeng*, who was my biggest cheerleader until her very last days – thank you cannot express how I feel. As hard as it was, the motivation to complete this work after your sudden passing inspired me to make you proud and to prove to myself that I am capable of pushing through in spite of everything.

My friends, Bongeka Mngwengwe, Elisabeth Ndjengue Mindang, Dimpho Paledi, Kefuoe Matsepe, Mookho Ntene, Obonabulumko Mbili, Nkareng Matsepe, Lerato Nthabi, Alina Hakane, Pontsó Khalane, Mpoetsi Nketsi, Sekeleme Shakhola and Mojahi Motaung. Thank you for supporting me through this journey, your love, motivation, and ability to hold me accountable to the goals I set helped finish this work.

To Velisani Vangile and Thandolwethu Njili, thank you for being my personal chauffeurs, those late nights would have not been possible without you. And for constantly checking up on me to make sure I was okay and everything was going well and on track.

To my colleagues in the SMALL research group, Bongeka Mngwengwe, Binita Manilal, Tristan Harakraj and Paula Maseko, thank you for the motivation and always making sure that we are pushing each other to get the work done.

Special shout out to Dr Kemboi, Dr Ndagano and Dr Mafokwana for being great academic mentors, friends and helping kick-start the writing process.

Last but not least, Prof Klein for the moral support and always making time to listen to my problems – eternally grateful.

Rhodes University and the Sandisa Imbewu bursary for financial support.

Abstract

Tuberculosis remains as a prominent cause of death worldwide. This infectious disease is treated with first and second line drugs. However, challenges of multi drug resistant tuberculosis and adverse side effects such as depletion of essential B group vitamins in the body by first line drugs, as well as poor physicochemical properties of second line drugs persist. Cocrystallisation of anti-tubercular drugs with various coformers has therefore been used as an alternative method to improve the physicochemical properties of active pharmaceutical ingredients (API) while maintaining their efficacy. The main objective of this study was to carry out cocrystal screening of anti-tubercular API and vitamin B coformers to make drug-drug or drug-vitamin multicomponent complexes.

Preparation of the multicomponent complexes was carried out by mechanochemical grinding (neat grinding (NG), liquid assisted grinding (LAG) and slow evaporation. All complexes were characterised using Fourier-transform infrared spectroscopy (FTIR), powder X-ray diffraction (PXRD), differential scanning calorimetry (DSC), thermogravimetric analysis (TGA) and crystal structures were elucidated using single-crystal X-ray diffraction (SCXRD).

The cocrystal screening resulted in the formation of various solid forms, which included cocrystals, salts and eutectic products. Two cocrystals of 4-aminosalicylic acid (PAS) were isolated and characterised. The cocrystal of PAS with isoniazid (INH) demonstrated similar characteristics for both the bulk crystalline material and milled materials. The cocrystal of PAS and pyrazinamide (PYR) prepared using mechanochemical synthesis was met with challenges, while difficulties were also encountered in obtaining suitable crystals for SCXRD analysis. The ground and recrystallised samples of the PAS and pyrazinecarboxylic acid (PCBA) showed distinct differences in their thermal behaviour, with SCXRD revealing the decomposition product phenolammonium-pyrazinecarboxylate salt *'sans'* the CO_2 moiety.

Salt formation involving pyridoxine (PN) yielded a salt hydrate with PAS (PN-PAS) and an anhydrous salt with PCBA (PN-PCBA). Both salts exhibited very complex packing arrangements with equally complex thermal behaviour depending on the solvent used during preparation, and the method of preparation.

Three eutectic systems involving INH with PYR, PN and pyridoxine hydrochloride (PN·HCl) were identified, and their phase diagrams were constructed from DSC data. The eutectic compositions obtained were 1:1 for INH:PYR, 1:1 for INH:PN and 6:4 for INH:PN·HCl.

Finally, a total of eight multicomponent complexes were prepared using selected API and vitamin B_6 components. The results presented here provide motivation for further investigation and evaluation of the pharmacochemical properties of these API.

Chapter 1: Introduction

1.1. Supramolecular chemistry

Supramolecular chemistry stems from the work of Emil Fischer who, in 1894, proposed the lock-and-key hypothesis for enzyme-substrate interactions. This hypothesis is based on the idea that the active site of an enzyme is specifically designed to fit only one specific substrate.[1] It is from this idea that the principles of molecular recognition and supramolecular function for supramolecular chemistry emerged. The term supramolecular chemistry was coined by Jean-Marie Lehn in 1969, who was later awarded the 1987 Nobel Prize in Chemistry alongside Charles Pedersen and Donald Cram, establishing supramolecular chemistry as an independent field of research.[1] Supramolecular chemistry is commonly referred to as "chemistry beyond the molecule", and is defined by Lehn as "the chemistry of molecular assemblies and intermolecular bonds".[2]

Supramolecular chemistry can be divided into two broad categories *viz*., host-guest chemistry and self-assembly. Host-guest chemistry occurs when one molecule is significantly larger (the host) than the other (the guest) enclosing the smaller molecule, in a host-guest relationship. In contrast, self-assembly occurs when there is no significant difference in size between molecules and the molecules spontaneously join together producing large non-covalently bound aggregates.[3] These two approaches lead to the formation of supramolecular compounds, which are held together by non-covalent interactions such as van der Waals forces, π-π interactions, hydrogen bonding and other non-covalent interactions.[2] It is from the formation of these supermolecules that researchers seek to understand intermolecular interactions and recognition phenomena in the context of crystal packing. This approach is called crystal engineering. The aim of crystal engineering is to utilise '*this'* understanding to develop principles in the design of new solids that exhibit specific physical and chemical properties.[4]

Supramolecular chemistry is used in a variety of applications and its utilization in the pharmaceutical industry has seen incredible growth in recent years since the formation of solids with properties tailored for specific purposes are possible. From the use of large host molecules such as cyclodextrins and cucurbit[*n*]urils for drug delivery and formulation[5], the use of chemical self-assembly to make nanoparticles, hydrogels, coating films, and other solids have the potential to be used in medical research.[6] Research has also shown that the properties of active pharmaceutical ingredients (API) can be improved by supramolecular modification resulting in drugs with improved physicochemical properties. This study aims to explore the preparation of pharmaceutical cocrystals with compounds used for the treatment of tuberculosis (TB) *via* supramolecular self-assembly.

1.2. Solid-state forms

Most API are solids that may be categorised according to their phase (illustrated in **Scheme 1**). For instance, polymorphism occurs when a molecule has more than one crystal structure (or crystal phase), with each crystal phase possessing different physicochemical properties.[7] Amorphous materials do not exhibit long range order while solvated materials have solvent molecule(s) included in the crystal structure. If the crystal structure is retained following the removal of solvent from the material it is referred to as the apohost phase. When the phase changes or there is a rearrangement after solvent removal it is referred to as the desolvated phase.[7,8] Hydrates are a subclass of solvates where the solvent included is water.[8] In the solid-state, salts are formed when complete proton transfer between an acid and a base occurs, leading to an ionic interaction between the acid and the base.[9] Finally, cocrystals are, "solid crystalline single phase materials composed of two or more different molecular compounds generally in a stoichiometric ratio, which are neither solvates nor simple salts".[10]

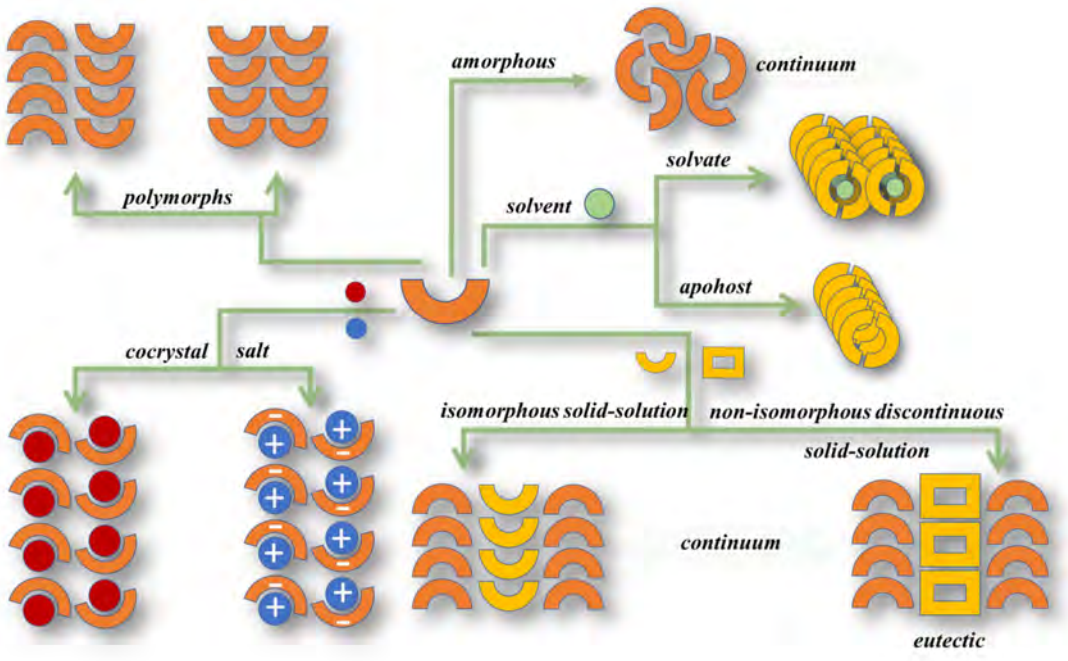

Scheme 1: Schematic illustration of the differences between solid forms, adapted from Cherukuvada *et al.* [11]

Apart from the formation of cocrystals, other entities may result from cocrystallisation experiments such as the formation of solid solutions, eutectics or simple physical mixtures of the starting materials. Solid-solutions and eutectics are similar in that they are held together by cohesive (homomolecular) interactions with comparable lattice structures to those of the starting components.[12] The difference between eutectics and solid solutions is eutectics consist of non-isomorphous compounds while solid-solutions consist of isomorphous or isostructural materials.[11] Salts and cocrystals result in lattice structures that are different from the structure of the starting materials.

1.2.1. Selection of coformers

A coformer, also known as a cocrystal former, is described as "a component that interacts non-ionically with an API in the crystal lattice, that is not a solvent and is typically non-volatile".[13] In the synthesis of cocrystals, compounds that are commonly used as coformers are API, excipients, food additives or substances that have been listed on the "generally regarded as safe" (GRAS) list or from the "everything added to food in the US" (EAFUS) list or more recently, from the "substances added to food" list that comprises both the GRAS and the EAFUS lists.[14] Cocrystals hold several advantages over other solid forms in that they exist in a stable crystalline form and are more readily characterized by powder X-ray diffraction (PXRD). Additionally, the stoichiometric quantity of coformers removes the need for excess use of excipients and additives.[15] Cocrystal formation does not require an API to have ionizable groups to form an interaction, which is a prerequisite for salt formation. Compared to polymorphic forms, for which the stability can be influenced by external factors such as temperature and pressure, the properties of cocrystals can be controlled by careful selection of the coformer used, known to result in more stable and chemically inert compounds.[8] Cocrystals can also be tailored to enhance the processability of API in medicine manufacture.[13]

A full proof method, systematic or other, for selecting a suitable coformer does not exist however; there are some theoretical and experimental approaches that may be used as guidelines for the selection of coformers for cocrystal screening/preparation activities. These include the pK_a rule,[16,17] supramolecular synthon approach,[18–21] and computational approaches accessible from the suite of programmes available in the Cambridge Structural Database (CSD).[22]

1.2.1.1. pK_a rule

Salt formation is characterised by proton transfer between an acid and a base while for cocrystals proton transfer does not occur. For multicomponent crystals a generally accepted guideline is used to predict whether the product of a cocrystallisation experiment will be a salt or a cocrystal. The approach is based on the difference between the pK_a of the acid and base constituents used in the cocrystallisation experiment. Known as the pK_a 'rule' it is based on ΔpK_a, where ΔpK_a = pK_a (base) - pK_a (acid). When $\Delta pK_a > 4$ the cocrystallisation attempt is most likely to lead to salt formation, whereas a value of $\Delta pK_a < -1$ may lead to cocrystal formation. If the value of ΔpK_a falls between -1 and 4, then either a salt or cocrystal may result.[16] Recently, Cruz-Cabeza *et al.*,[17] expanded the pK_a rule by taking into account the crystal composition by considering solvated versus unsolvated forms. Their work demonstrated that the crystal composition has an important influence on the pK_a rule as it shifts the ΔpK_a value at which there is an equal likelihood for formation of either a salt or cocrystal. This approach is narrow as the data reported in the literature is limited to aqueous pK_a values, crystal structures without defects and crystals grown from a limited selection of solvents, therefore, there is still a need for more research before it can be established as an actual "rule".[16]

1.2.1.2. Supramolecular synthon approach

Supramolecular synthons were defined by Desiraju as structural units within supermolecules that can be formed and/or assembled by known intermolecular interactions such as hydrogen bonding, van der Waals forces, π – π stacking or other non-covalent interactions.[18] Supramolecular synthons can be categorized as homosynthons and heterosynthons. Homosynthons are made of identical functional groups such as carboxylic acid or amide dimers and heterosynthons are made of different complementary functional groups such as acid-pyridine or hydroxyl-amide moieties as depicted in **Figure 1**.[19]

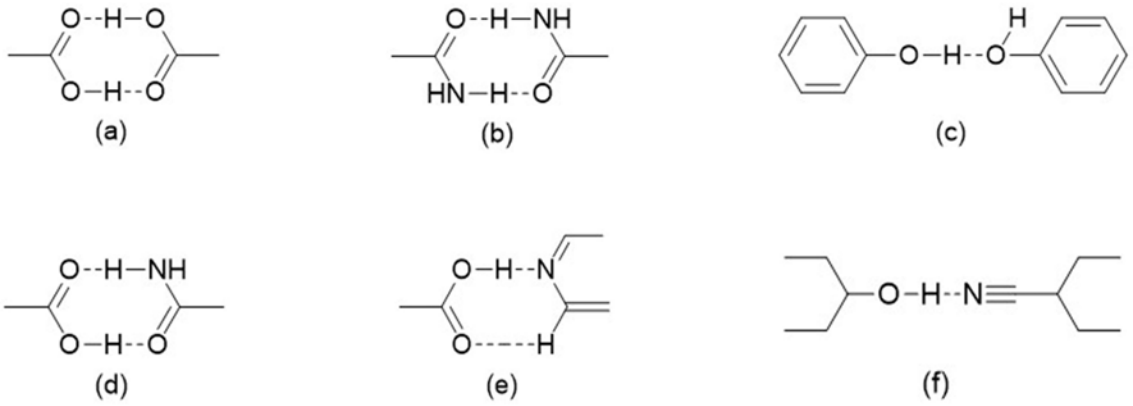

Figure 1: Common supramolecular synthons in crystal engineering, (a-c) are supramolecular homosynthon dimers while (d-f) are supramolecular heterosynthons.[19]

Of the non-covalent interactions in supermolecules, hydrogen bonding is the strongest and most common intra- and intermolecular interaction found in cocrystals. The functional groups commonly involved in hydrogen bonding are carboxylic acids, amides and alcohols.[20] The general rules for hydrogen bond formation, postulated by Etter in 1991, are that i) the best proton donors and acceptors are used first, ii) six membered ring intramolecular hydrogen bonds form in preference to intermolecular hydrogen bonds, and iii) the best proton donors and acceptors remaining after intramolecular hydrogen bond formation will form intermolecular hydrogen bonds to one another.[21]

1.2.1.3. The Cambridge Structural Database (CSD)

The CSD repository is a validated curated resource with over one million experimental three-dimensional structures generated through crystallographic analyses.[22] The interface contains a wide range of organic and organometallic molecules from which a supramolecular library of cocrystal formers was developed. It can be used for virtual screening to identify potential cocrystal forming pairs through molecular modelling.[19]

The suite of programmes such as Isostar,[23] Mercury,[24] and Conquest,[25] to mention but a few, available in the CSD, permits for calculations that provide a quantitative measure of the likelihood of interactions to occur between two components or to search for the best cocrystal forming pairs.

Examples of such are the molecular complementarity analysis of coformers and hydrogen bonding propensity calculations that can be carried out using the molecular complementarity tool (MCT)[26] and logit hydrogen bonding propensity (LHP)[25]. Different sets of cocrystal forming structures can be uploaded and the MCT programme can be used to predict appropriate cocrystal forming pairs or to find pairs of molecules that have the potential to form cocrystals in the case of LHP. Results from these calculations can be used to direct cocrystal screening experiments.

Other, relatively newer, methods include lattice energy calculations, conductor-like screening models for real solvents (COSMO-RS), virtual screening based on molecular electrostatic potential surfaces-MEPS, thermal analysis, measuring saturation temperature and the Kofler contact method and matching.[27] All these methods are not fool proof; however, they do reduce the time and process of using a "blind" trial and error approach.

1.3. Mechanochemistry

Mechanochemistry refers to reactions or chemical transformations that occur on input of mechanical energy into a system by means of manual grinding using a mortar and pestle, or through the use of automated ball milling systems.[28] Mechanochemistry has not been treated with significant regard compared to conventional solution-based methods of synthesis. However, the push towards greener methods of production has recently led to the reinvigoration of the technique. There has been rapid growth in the application of mechanochemistry to inorganic compounds, polymers and alloying, synthesis of organic compounds, catalysis, cocrystal formation and some pharmaceutical applications.[29] The advantages of this approach are that it offers stoichiometric control for a reaction and facilitates the synthesis of precise, targeted stoichiometrically different products such as cocrystals or coordination polymers through control of the composition of reaction mixtures.[30] The process offers a cleaner route of synthesis as it uses very little or no solvent at all and permits for the synthesis of poorly soluble substances under ambient conditions. Lastly, the technique can be used to control polymorphism *via* liquid-assisted grinding (LAG), thereby permitting the synthesis of selective polymorphs by using different liquid additives.[31] The methods used in the application of mechanochemistry are described in section 1.3.1.

1.3.1. Cocrystal preparation methods

The most common routes of cocrystal formation are solid-state or mechanosynthesis and solution-based methods. As previously mentioned, solid-state methods make use of little or no solvent, which may result in higher yields when compared to solution-based methods, as product loss is limited.[32] However, many different methods have been reported that describe the preparation of cocrystals and a selection of these methods is reported here, commencing with solid-state methods (1.3.1.1.).

- Contact cocrystallisation describes the spontaneous formation of cocrystals by mixing of the pure components under controlled atmospheric conditions without application of any

mechanical force. In some cases, limited grinding of the individual pure components is required before mixing.[32–34]

- Neat grinding involves combining the components in the dry solid-state after which they are ground either manually, using a mortar and pestle, or mechanically, using a ball or vibrational mill.[35]
- Liquid assisted grinding involves the addition of a small volume of solvent to the dry solid components prior to milling. The solvent is thought to act as a catalyst accelerating cocrystal formation.[32]
- The extrusion method of preparation involves combining components in a bespoke extruder and there are at least two approaches by which this can be implemented:
  a) Twin screw extrusion (TSE) which is operated at temperatures lower than the melting points of both starting materials using a twin screw extruder. The extruder consists of two co-counter-rotating screws in a single barrel and screw action provides concurrent mixing and movement of the material along the length of the barrel.[32]
  b) Hot melt extrusion (HME) makes use of a heated screw extruder that facilitates the simultaneous melting and mixing of the starting materials. The advantages of using HME are that it eliminates the need for organic solvents, is rapid, waste is reduced and conversion rates are increased.[32]
- High shear wet granulation involves the agglomeration of powder particles *via* a liquid medium in the presence of a binder. The procedure is carried out in a high shear granulator which imparts shear to the powder mixture with an impeller and/or a chopper.[32]

1.3.1.2. Solution-based methods use a single or mixture of solvents to dissolve the starting materials for cocrystal formation. The driving force behind this approach is the supersaturation of the cocrystal while the reactants are saturated or under-saturated under experimental conditions.[36] Solution-based methods are of importance as they lead to formation of cocrystals that can be evaluated using single-crystal X-ray diffraction (SCXRD) to elucidate the cocrystal structure. These methods can be performed in a variety of ways.

- Solvent evaporation involves dissolving starting materials in a suitable solvent or mixture of solvents and then allowing the solution to evaporate slowly. In order to produce clean cocrystals, the crystal sample should be collected before the solution evaporates to dryness.[27]
- Antisolvent addition involves the reduction of the cocrystal solubility by the addition of an antisolvent that promotes supersaturation and leads to crystal precipitation.[37]
- Reaction crystallisation is a process in which the reactants in non-stoichiometric ratios are mixed to form a supersaturated cocrystal solution that subsequently leads to cocrystal precipitation. This method is suitable when the cocrystal components have different

solubilities in such a way that one component is more soluble in a chosen solvent than the other.[36]

- Cooling crystallisation involves mixing the reactants and solvent in a reactor that is subsequently heated to achieve total dissolution of both components after which cooling promotes supersaturation and formation of the cocrystals.[35]
- Slurry conversion is a process that involves excess addition of the cocrystal components to a solvent. Each component is individually dissolved according to its solubility to form a complex solution that promotes nucleation and crystal growth.[36]
- Ultrasound-assisted solution cocrystallisation method involves the application of ultrasound to a solution. The ultrasonic waves provide cavitation energy that induces nucleation at lower supersaturation levels. This technique may also be paired with slurry conversion.[37,38]

1.3.1.3. Supercritical fluid technology is an alternative method that has been used to produce cocrystals. A supercritical fluid (SCF) exhibits the combined properties of both gases and liquids which has an advantage of enhanced atomization, ability to dissolve a wide range of components and miscibility with organic liquids.[37] These properties form the basis for cocrystal formation, based on SCF technology.

- Cocrystallisation with supercritical solvent (CSS) occurs when pure solid compounds are dissolved in a vessel in supercritical CO_2 and supersaturation is induced by depressurization.[37]
- Supercritical antisolvent cocrystallisation (SAS) is based on the principle that the solubility of the cocrystal components is reduced in a SCF, allowing them to precipitate together as cocrystals.[32]
- Rapid expansion of supercritical solvents (RESS) involves saturation of the SCF with the solid cocrystal components prior to depressurization of the SCF phase sprayed through a nozzle into a drying chamber at atmospheric pressure.[32]
- Supercritical CO_2-assisted spray drying uses the SCF as an atomization enhancer where the solution containing the cocrystal components is sprayed through a nozzle with supercritical CO_2 into a drying chamber at atmospheric pressure.[32]

Other methods used in cocrystal formation include laser irradiation,[39] electrochemically induced cocrystallisation,[40] spray drying,[41] resonant acoustic mixing,[42] freeze-drying[43] and electrospray technology.[44] In a recent publication by Martinez and co-workers,[45] they demonstrated the latest advances in mechanochemical synthesis by milling/grinding; the milling is combined with different energy sources that are usually used in solution-based methods. These techniques include thermo-, sono-, electro- and photo-mechanochemistry approaches and point to a whole new level of solid-state reactivity.

1.4. Pharmaceutical cocrystals

Cocrystallisation of active pharmaceutical ingredients (API) with judiciously identified and selected coformers has attracted substantial interest owing to the facile manner in which physicochemical properties may be improved. As previously mentioned, coformers may be selected from the "substances added to food" list which comprises both the GRAS and the EAFUS lists.[14]

Compared to the more traditional ways of tailoring drug properties, cocrystallisation has the advantage that the physicochemical properties of a compound may be altered without affecting the pharmacological properties of that compound. The formation of cocrystals is proven as a means of improving characteristics such as solubility, stability, melting point, hygroscopicity, and flow properties. Lastly, cocrystals have the potential to shorten drug product development timelines and solid-state synthesis techniques offer a green synthetic route with high yields, little to no solvent use and very few by-products that contributes to a reduced cost of production.[15,27]

1.4.1. Active Pharmaceutical Ingredients and Water

Solid API are likely to be exposed to water during processing and storage, or in dosage forms consisting of materials that contain water that could transfer to other components of the formulation.[46] Water incorporation can occur via solid surface adsorption where no water penetrates into the bulk phase (**Figure 2 (a)**), by formation of condensed liquid water on the solid surface (**Figure 2 (b)**), adsorption into crystal defects and disordered regions of the solid (**Figure 2 (c)**), and/or by absorption into the crystal structure to form a hydrate (**Figure 2 (d)**).[47]

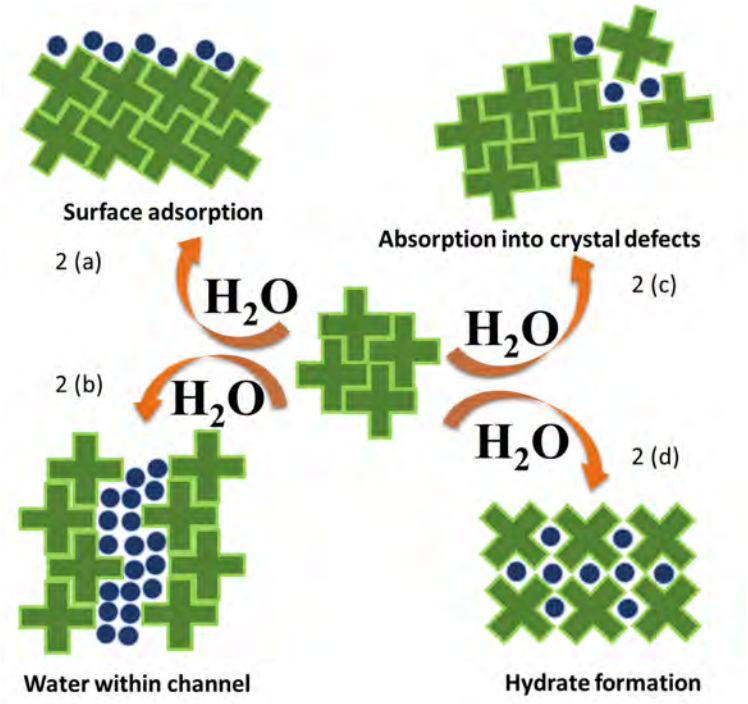

Figure 2: Schematic representation of water vapour interaction with crystalline solids. Adapted from Urbanus *et al.*, 2010.[40]

Water is a pharmaceutically acceptable solvent that is able to participate in hydrogen bonding as both a hydrogen bond donor and acceptor. Hydrate formation may lead to physicochemical and mechanical properties of a solid, that differ from the anhydrous forms.[47,48] It may also alter the thermodynamic activity of pharmaceutical solids, which affects solubility, dissolution rate and phase stability. These changes may alter bioavailability and ultimately product performance.[46, 48] The impact of water on the formation of pharmaceutical cocrystals are numerous and some of these are depicted in **Figure 3.** Not all the effects of water inclusion are negative and there are well documented reports in which cocrystals are reported to exist because of the inclusion of water. An example of this is the cocrystallisation of the anti-retroviral medicines (ARVs), lamivudine and zidovudine. The cocrystal only forms when there is water present as the ARV are hydrogen bonded to each other *via* the water molecule and all attempts to make the cocrystals from water-free media led to no cocrystal formation.[49]

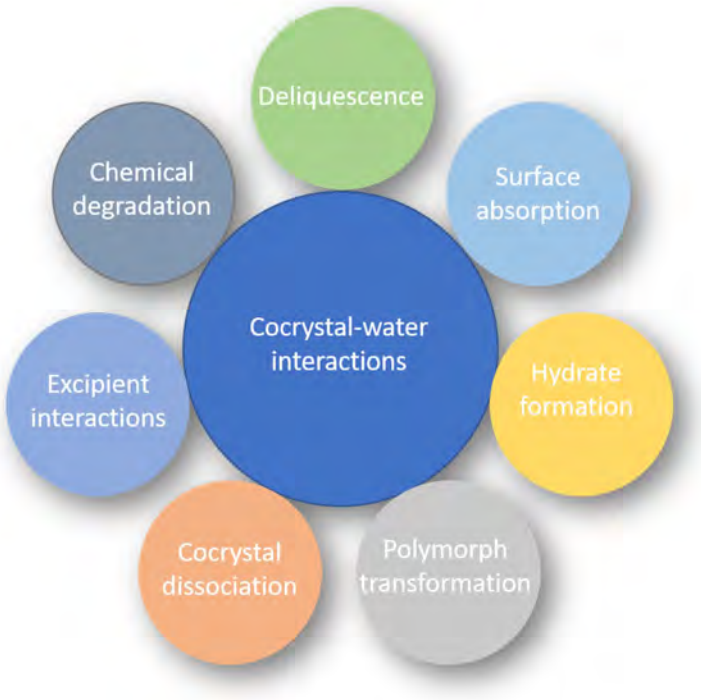

Figure 3: The resultant effects of water on cocrystals and other solid-phase materials, adapted from Emami *et al.*[47]

1.5. Tuberculosis

Tuberculosis (TB) is a bacterial infection caused by *Mycobacterium tuberculosis* and according to the World Health Organization (WHO), tuberculosis is the second most infectious disease after COVID-19 and is ranked as the 13th leading cause of death worldwide.[50] Globally, an estimated 10.6 million people contracted TB in 2021 while about 1.6 million TB related deaths were reported over the same period. The COVID-19 pandemic had a negative impact on the management of TB and led to a decline in case reporting between 2020 and 2022 (**Figure 4)**. The pandemic had a major impact on

access to and provision of TB services. The main consequence is an increase in the number of people with undiagnosed and untreated TB, which may lead to greater transmissions and long term negative effects in the fight against the disease.[50]

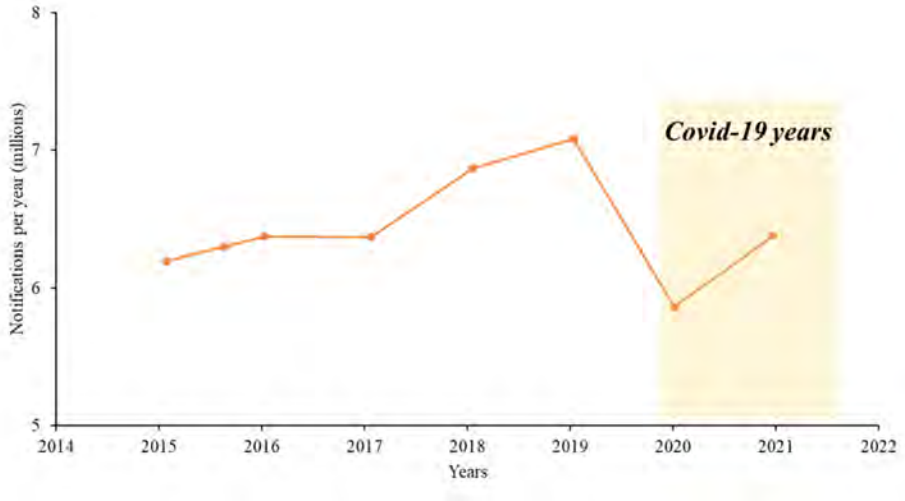

Figure 4: Global trend in case notifications of people newly diagnosed with TB between 2015 and 2021, adapted from the WHO, Global report on tuberculosis.[50]

1.5.1. Treatment of TB

The first recorded drug used for the successful treatment of TB was streptomycin, which was followed by first line treatment using isoniazid, rifampicin, ethambutol, and pyrazinamide between 1950 and 1970.[51] These drugs proved effective but exhibit significant side effects and subsequently development of bacterial resistance. Multi-drug treatment was subsequently introduced to circumvent this challenge. It has been observed that poor patient adherence to TB treatment regimens, health care providers prescribing the wrong treatment and unavailability of drugs in some communities are the major contributors to development of multi-drug resistant tuberculosis (MDR-TB).[52] MDR-TB is the resistance to at least isoniazid and rifampicin and it is one of the biggest challenges when treating TB.[50] The occurrence of MDR-TB led to the introduction of second line drugs such as ethionamide, cycloserine and the fluoroquinolones to treat MDR-TB. However, these second line drugs exhibit toxicity, poor solubility and permeability and are chemically labile.[54, 55] These issues have led to the development, repurposing and reuse of API in an attempt to define new treatment regimens. Drug development is a tedious and complicated process that often may take about 10-15 years for a new drug product to achieve market authorisation; however, new approaches such as cocrystallisation show a lot of promise for shorter development times at reduced cost. With the existing drug molecules, research has been focused on improving properties such as solubility, permeability, stability, and bioavailability without compromising efficacy, through cocrystallisation.[27]

1.6. Anti-TB drugs selected

The choice of coformers for this study was based on several ideas. The first of which is the supramolecular synthon approach which takes into account the functional groups present in the main API, 4-aminosalicylic acid (PAS), secondly, using existing API that are concurrently administered to treat TB with complementary functional groups suitable for hydrogen-bond formation and lastly, non-API coformers such as the B group vitamins that have antimycobacterial properties and which possess functional groups that are suitable for hydrogen bond formation.[55] Furthermore, TB medicines affect the metabolism of vitamins, particularly B vitamins, resulting in severe vitamin B deficiency, necessitating the concomitant administration of supplements with API to prevent such deficiencies.[56,57] A list of the coformers used in this investigation is summarized in **Table 1**.

Table 1: List of coformers used in the course of this work.

Coformers	Melting point (°C)	Aqueous solubility (g/L)	API/Excipient	Refs
4-aminosalicylic acid	135-145	2	API	[58]
Isoniazid	171-173	125	API	[59]
Pyrazinamide	189-191	50	API	[60]
Pyrazinecarboxylic acid	222-225	Soluble in cold water	API	[61]
Isonicotinamide	155-157	191.7	Excipient	[62]
Nicotinamide	128-131	691	Supplement	[63]
Caffeine	234-236	20	Excipient	[64]
Pyridoxine	159-162	100	Supplement	[65]
4-hydroxybenzoic acid	213-217	5	Excipient	[66]
Isonicotinic acid	310	5.2	API	[67]
Nicotinic acid	236-239	1-5 g/100 mL	Supplement	[68]
Pyridoxine hydrochloride	214-215	0.1 g/mL	Supplement	[69]

Aims and objectives

The aims of the project described here is to prepare solid forms of selected anti-TB API using mechanochemical and co-precipitation methods. The specific objectives were as follows:

1. Preparation of different multicomponent forms of the selected API.
2. The use of neat, liquid assisted grinding and solvent based 'slow' evaporation methods to obtain multicomponent materials.
3. Bulk characterisation of the supramolecular complexes using Fourier-transform infrared spectroscopy, differential scanning calorimetry, thermogravimetric analysis and powder X-ray diffraction.
4. Finally, characterise all crystalline multicomponent crystals using single-crystal X-ray diffraction.

References

(1) Desiraju G. R. Chemistry beyond the Molecule. *Nat.* **2001**, *412* , 397–400.

(2) Varshey D. B., Sander J. R. G., Friščić T. and MacGillivray L. R. Supramolecular Interactions. In *Supramolecular Chemistry: From molecules to nanomaterials*; John Wiley&Sons, Ltd: United Kingdom, 2012, 1,9–24.

(3) Steed J. W., Turner D. R. and Wallace K. J. *Core Concepts of in Supramolecular Chemistry and Nanochemistry*, 1st ed.; John Wiley&Sons, Ltd: England, 2007.

(4) Desiraju G. R. Crystal Engineering: A Holistic View. *Angew. Chem. Int. Ed.* **2007**, *46*, 8342–8356.

(5) Kolesnichenko I. V. and Anslyn E. V. Practical Applications of Supramolecular Chemistry. *Chem. Soc. Rev.* **2017**, *46*, 2385–2390.

(6) Lu R., Zhang X., Cheng X., Zhang Y., Zan X. and Zhang L. Medical Applications Based on Supramolecular Self-Assembled Materials From Tannic Acid. *Front. in Chem.* **2020**, *8*, 1–25.

(7) Byrn S. R., Pfeiffer R. R., Stephenson G., Grant D. J. W. and Gleason W. B. Solid-State Pharmaceutical Chemistry. *Chem. Mater.* **1994**, *6*, 1148–1158.

(8) Aitipamula S., Zaiqun Y., Chow P. S. and Tan R. B. H. Pharmaceutical Co-Crystals-Molecular Design and Process Development. In *Co-crystals; Preparation, Characterization and Applications*; The Royal Society of Chemistry, 2018, Vol. 24,194–230.

(9) Aitipamula S., Banerjee R., Bansal A. K., Biradha K., Cheney M. L., Choudhury A. R., Desiraju G. R., Dikundwar A. G., Dubey R., Duggirala N., Ghogale P. P., Ghosh S., Goswami P. K., Goud N. R., Jetti R. R. K. R., Karpinski P., Kaushik P., Kumar D., Kumar V., Moulton B., Mukherjee A., Mukherjee G., Myerson A. S., Puri V., Ramanan A., Rajamannar T., Reddy C. M., Rodriguez-Hornedo N., Rogers R. D., Row T. N. G., Sanphui P., Shan N., Shete G., Singh A., Sun C. C., Swift J. A., Thaimattam R., Thakur T. S., Kumar Thaper R., Thomas S. P., Tothadi S., Vangala V. R., Variankaval N., Vishweshwar P., Weyna D. R. and Zaworotko M. J. Polymorphs, Salts, and Cocrystals: What's in a Name? *Cryst. Growth Des.* **2012**, *12*, 2147–2152.

(10) Duggirala N. K., Perry M. L., Almarsson Ö. and Zaworotko M. J. Pharmaceutical Cocrystals: Along the Path to Improved Medicines. *Chem. Commun.* **2016**, *52*, 640–655.

(11) Cherukuvada S. and Nangia A. Eutectics as Improved Pharmaceutical Materials: Design, Properties and Characterization. *Chem. Commun.* **2014**, *50*, 906–923.

(12) Cherukuvada S. and Guru Row T. N. Comprehending the Formation of Eutectics and Cocrystals in Terms of Design and Their Structural Interrelationships. *Cryst. Growth Des.* **2014**, *14*, 4187-4198.

(13) Food and Drug Administration. Regulatory Classification of Pharmaceutical Co-Crystals Guidance for Industry, 2018. https://www.fda.gov/files/drugs/published/Regulatory-Classification-of-Pharmaceutical-Co-Crystals.pdf (accessed 2023-03-21).

(14) Food and Drug Administration. Substances Added to Food (Formerly EAFUS). *FDA* **2018**.

(15) Bolla G. and Nangia A. Pharmaceutical Cocrystals: Walking the Talk. *Chem. Commun.* **2016**, *52*, 8342–8360.

(16) Cruz-Cabeza A. J. Acid–Base Crystalline Complexes and the p*Ka* Rule. *CrystEngComm* **2012**, *14*, 6362-6365.

(17) Cruz-Cabeza A. J., Lusi M., Wheatcroft H. P. and Bond A. D. The Role of Solvation in Proton Transfer Reactions: Implications for Predicting Salt/Co-Crystal Formation Using the $\Delta p K_a$ Rule. *Faraday Discuss.* **2022**, *235*, 446–466.

(18) Desiraju G. R. Supramolecular Synthons in Crystal Engineering—A New Organic Synthesis. *Angew. Chem. Int. Ed. Engl.* **1995**, *34*, 2311–2327.

(19) Kumar S. and Nanda A. Approaches to Design of Pharmaceutical Cocrystals: A Review. *Mol. Cryst. Liq. Crystals* **2018**, *667*, 54–77.

(20) Sarma B., Chen J., Hsi H.-Y. and Myerson A. S. Solid Forms of Pharmaceuticals: Polymorphs, Salts and Cocrystals. *Korean J. Chem. Eng.* **2011**, *28*, 315–322.

(21) Etter M. C. Hydrogen Bonds as Design Elements in Organic Chemistry. *J. Phys. Chem.* **1991**, *95*, 4601–4610.

(22) Ferrence G. M., Tovee C. A., Holgate S. J. W., Johnson N. T., Lightfoot M. P., Nowakowska-Orzechowska K. L. and Ward S. C. *CSD Communications* of the Cambridge Structural Database. *IUCrJ.* **2023**, *10*, 6–15.

(23) Novikov A. S. IsoStar Program Suite for Studies of Noncovalent Interactions in Crystals of Chemical Compounds. *Crystals.* **2021**,11, 162-163.

(24) Macrae C. F., Sovago I., Cottrell S. J., Galek P. T. A., McCabe P., Pidcock E., Platings M., Shields G. P., Stevens J. S., Towler M. and Wood P. A. *Mercury 4.0* : From Visualization to Analysis, Design and Prediction. *J. Appl. Cryst.* **2020**, *53*, 226–235.

(25) Galek P. T. A., Fabian L., Motherwell W. D. S., Allen F. H. and Feeder N. Knowledge-Based Model of Hydrogen-Bonding Propensity in Organic Crystals. *Acta Cryst.* **2007**, *B63*, 768–782.

(26) Cappuccino C., Cusack D., Flanagan J., Harrison C., Holohan C., Lestari M., Walsh G. and Lusi M. How Many Cocrystals Are We Missing? Assessing Two Crystal Engineering Approaches to Pharmaceutical Cocrystal Screening. *Cryst. Growth Des.* **2022**, *22*, 1390–1397.

(27) Nanda A. Pharmaceutical Cocrystals: An Overview. *Indian J. Pharm. Sci.* **2017**, 858-871.

(28) James S. L., Adams C. J., Bolm C., Braga D., Collier P., Friščić T., Grepioni F., Harris K. D. M., Hyett G., Jones W., Krebs A., Mack J., Maini L., Orpen A. G., Parkin I. P., Shearouse W. C., Steed J. W. and Waddell D. C. Mechanochemistry: Opportunities for New and Cleaner Synthesis. *Chem. Soc. Rev.* **2012**, *41*, 413–447.

(29) Baláž P., Baláž M. and Bujňáková Z. Mechanochemistry in Technology: From Minerals to Nanomaterials and Drugs. *Chem. Eng. Technol.* **2014**, *37*, 747–756.

(30) Do J.-L. and Friščić T. Mechanochemistry: A Force of Synthesis. *ACS Cent. Sci.* **2017**, *3*, 13–19.

(31) Friščić T. Mechanochemistry in Co-Crystal Synthesis. In *Co-crystals: Preparation., Characterization and Applications (Monographs in Supramolecular Chemistry)*; Royal Society of Chemistry, 2018; Vol. 24, pp 147–193.

(32) Karimi-Jafari M., Padrela L., Walker G. M. and Croker D. M. Creating Cocrystals: A Review of Pharmaceutical Cocrystal Preparation Routes and Applications. *Cryst. Growth Des.* **2018**, *18*, 6370–6387.

(33) Maheshwari C., Jayasankar A., Khan N. A., Amidon G. E. and Rodríguez-Hornedo N. Factors That Influence the Spontaneous Formation of Pharmaceutical Cocrystals by Simply Mixing Solid Reactants. *CrystEngComm* **2009**, *11*, 493–500.

(34) Ervasti T., Ketolainen J. and Aaltonen J. Spontaneous Formation of Theophylline–Nicotinamide Cocrystals. *Sci. Pharm.* **2010**, *78*, 622–622.

(35) Qiao N., Li M., Schlindwein W., Malek N., Davies A. and Trappitt G. Pharmaceutical Cocrystals: An Overview. *Int. J. of Pharm.* **2011**, *419*, 1–11.

(36) Guo M., Sun X., Chen J. and Cai T. Pharmaceutical Cocrystals: A Review of Preparations, Physicochemical Properties and Applications. *Acta Pharm. Sin. B.* **2021**, *11*, 2537–2564.

(37) Rodrigues M., Baptista B., Lopes J. A. and Sarraguça M. C. Pharmaceutical Cocrystallization Techniques. Advances and Challenges. *Int. J. Pharm.* **2018**, *547*, 404–420.

(38) Aher S., Dhumal R., Mahadik K., Paradkar A. and York P. Ultrasound Assisted Cocrystallization from Solution (USSC) Containing a Non-Congruently Soluble Cocrystal Component Pair: Caffeine/Maleic Acid. *Eur. J. Pharm. Sci.,* **2010**, *41* , 597–602.

(39) Titapiwatanakun V., Basit A. W. and Gaisford S. A New Method for Producing Pharmaceutical Co-Crystals: Laser Irradiation of Powder Blends. *Cryst. Growth Des.* **2016**, *16*, 3307–3312.

(40) Urbanus J., Roelands C. P. M., Mazurek J., Verdoes D. and ter Horst J. H. Electrochemically Induced Co-Crystallization for Product Removal. *CrystEngComm* **2011**, *13*, 2817–2819.

(41) Matsuda Y., Kawaguchi S., Kobayashi H. and Nishijo J. Physicochemical Characterization of Spray-Dried Phenylbutazone Polymorphs. *J. Pharm.Sc.,* **1984**, *73*, 173–179.

(42) am Ende D. J., Anderson S. R. and Salan J. S. Development and Scale-Up of Cocrystals Using Resonant Acoustic Mixing. *Org. Process Res. Dev.* **2014**, *18*, 331–341.

(43) Eddleston M. D., Patel B., Day G. M. and Jones W. Cocrystallization by Freeze-Drying: Preparation of Novel Multicomponent Crystal Forms. *Cryst. Growth Des.* **2013**, *13*, 4599–4606.

(44) Patil S., Ujalambkar V. and Mahadik A. Electrospray Technology as a Probe for Cocrystal Synthesis: Influence of Solvent and Coformer Structure. *J. Drug Deliv. Sci. Technol*. **2017**, *39*, 217–222.

(45) Martinez V., Stolar T., Karadeniz B., Brekalo I. and Užarević K. Advancing Mechanochemical Synthesis by Combining Milling with Different Energy Sources. *Nat. Rev. Chem.* **2023**, *7*, 51–65.

(46) Khankari R. K. and Grant D. J. W. Pharmaceutical Hydrates. *Thermochim. Acta* **1995**, *248*, 61–79.

(47) Emami S., Ghafari R. and Manafzadeh E. Solid-State Interaction of Pharmaceutical Cocrystals with Water Vapor. *Cryst. Growth Des.* **2021**, *21*, 4805–4820.

(48) Jurczak E., Mazurek A. H., Szeleszczuk L., Pisklak D. M. and Zielinska-Pisklak M. Pharmaceutical Hydrates Analysis-Overview of Methods and Recent Advances. *Pharmaceutics* **2020**, *12*, 1–25.

(49) Bhatt P. M., Azim Y., Thakur T. S. and Desiraju G. R. Co-Crystals of the Anti-HIV Drugs Lamivudine and Zidovudine. *Cryst. Growth & Des.* **2009**, *9*, 951–957.

(50) World Health Organization. Global Tuberculosis Report **2022**.

(51) Murray J. F., Schraufnagel D. E. and Hopewell P. C. Treatment of Tuberculosis. A Historical Perspective. *Annals ATS.* **2015**, *12*, 1749–1759.

(52) Center for Disease Control and Prevention. *Tuberculosis (TB) - Drug-Resistant TB*. Centers for Disease Control and Prevention. https://www.cdc.gov/tb/topic/drtb/default.htm (accessed 2023-04-07).

(53) Caminero J. A. and Scardigli A. Classification of Antituberculosis Drugs: A New Proposal Based on the Most Recent Evidence. *Eur. Respir. J.* **2015**, *46*, 887–893.

(54) Rendon A., Tiberi S., Scardigli A., D'Ambrosio L., Centis R., Caminero J. A. and Migliori G. B. Classification of Drugs to Treat Multidrug-Resistant Tuberculosis (MDR-TB): Evidence and Perspectives. *J. Thorac. Dis.* **2016**, *8*, 2666–2671.

(55) Tyagi G., Singh P., Varma-Basil M. and Bose M. Role of Vitamins B, C, and D in the Fight against Tuberculosis. *Int. J. Mycobacteriol.* **2017**, *6*, 328.

(56) Gupta K. B., Gupta R., Atreja A., Verma M. and Vishvkarma S. Tuberculosis and Nutrition. *Lung India.* **2009**, *26*, 9-16.

(57) Shvets O., Shevchenko O., Piskur Z., Stepanenko G. and Pogorelova O. Vitamins B1 and B12 deficiency as a predictor of tuberculosis severity and peripheral nervous system damage. *Inter. Collegas.* **2020**, *7*, 184–187.

(58) *4-Aminosalicylic acid 65-49-6*. Chemical Book. https://www.chemicalbook.com/ChemicalProductProperty_EN_CB9679687.htm (accessed 2023-04-11).

(59) *Isoniazid, Chemical Information Search*. https://www.chemicalbook.com/ProductList_en.aspx?kwd=Isoniazid (accessed 2023-04-11).

(60) *Pyrazinamide, Chemical Information Search*. https://www.chemicalbook.com/ProductList_En.aspx?kwd=pyrazinamide (accessed 2023-04-11).

(61) *2-Pyrazinecarboxylic acid, Chemical Information Search*. https://www.chemicalbook.com/ProductList_En.aspx?kwd=pyrazinecarboxylic%20acid (accessed 2023-04-11).

(62) *Isonicotinamide, Chemical Information Search*. https://www.chemicalbook.com/ProductList_En.aspx?kwd=isonicotinamide (accessed 2023-04-11).

(63) *Nicotinamide, Chemical Information Search*. https://www.chemicalbook.com/ProductList_En.aspx?kwd=nicotinamide (accessed 2023-04-11).

(64) *Caffeine, Chemical Information Search*. https://www.chemicalbook.com/ProductList_En.aspx?kwd=caffeine (accessed 2023-04-11).

(65) *Pyridoxine, National Library of Medicine*. https://pubchem.ncbi.nlm.nih.gov/compound/Pyridoxine#section=Information-Sources (accessed 2024-02-04).

(66) *4-Hydroxybenzoic acid CAS#: 99-96-7*. https://www.chemicalbook.com/ProductChemicalPropertiesCB1412080_EN.htm (accessed 2023-11-29).

(67) *Isonicotinic acid, Chemical Information Search*. https://www.chemicalbook.com/ProductList_En.aspx?kwd=isonicotinic%20acid (accessed 2023-11-29).

(68) *Nicotinic acid, Chemical Information Search*. https://www.chemicalbook.com/ProductList_En.aspx?kwd=nicotinic%20acid (accessed 2023-11-29).

(69) *Pyridoxine hydrochloride CAS#: 58-56-0*. https://www.chemicalbook.com/ProductChemicalPropertiesCB8853882_EN.htm (accessed 2023-12-18).

Chapter 2: Experimental

2.1. Materials

All API, excipients and vitamins used were purchased from Sigma Aldrich except for isoniazid which was obtained from BDH laboratories. The solvents were at least of reagent grade and obtained from Tag Solvent Products (PTY) LTD (Gqeberha, South Africa). Ultrapure water was produced using RephiLe® Direct-Pure UP Ultrapure and RO water system (Microsep®, Johannesburg, South Africa). All reagents (summarised in **Table 1**) were used as received. The highlighted API/supplements are the chemicals whose combinations will be fully analysed in this dissertation.

Table 1: List of reagents, their purity and country of origin.

Reagent	% Purity (%)	Country of origin
Ultrapure water	18.2 MΩ at 19.3°C	-
Methanol	99.99	-
Acetonitrile	99.5	-
Ethyl acetate	99.8	-
Ethanol	99.9	-
4-aminosalicylic acid	99	India
Isoniazid	99	England
Pyrazinamide	99	Germany
Pyridoxine	98	Germany
Pyrazinecarboxylic acid	99	China
Pyridoxine hydrochloride	99	South Africa
Isonicotinamide	99	France
Nicotinamide	99	India
Caffeine	99	Switzerland
4-hydroxybenzoic acid	99	China
Isonicotinic acid	99	Germany
Nicotinic acid	99	India

2.2. Cocrystal preparation

Attempts to cocrystallise combinations of API and coformer were undertaken using the three methods; neat grinding (NG), liquid assisted grinding (LAG) and slow evaporation (SE). The grinds were performed using a mechanical ball mill constructed from a Makita Jigsaw (Makita Corporation Japan) that had a ball milling capsule attached to it. The milling media were 4.5 mm in diameter, had

an average weight of 0.3 g and made of steel with a zinc coating. The milling capsule was made of stainless steel, 10 mm in diameter, 35 mm in height and internal volume of 274.89 mm^3.

The API and coformer were ground in a mechanical ball mill for 20 min at a frequency of 16 Hz. Neat grinding involved dry grinding the starting materials while liquid assisted grinding involved addition of three drops of solvent (about 15 μL) prior to grinding. Four different solvents viz. methanol (MeOH), water (H_2O), acetonitrile (MeCN) and ethyl acetate (EtOAc) were used in LAG experiments. For co-precipitation experiments, the API and coformer were dissolved in the minimum amount of solvent and stirred until fully dissolved. Heating was used in cases where the compounds did not dissolve at room temperature, but the solvent was never heated to, or above its boiling point. The solutions were left at room temperature in a vial covered with parafilm which had been perforated to reduce the rate of evaporation of the solvent. In general, the API and coformer were combined in a 1:1 molar ratio based on predicted supramolecular synthons that have the potential to form cocrystals.

The physical mixtures for the eutectics were made by weighing different mole fractions of both components in 9:1, 8:2, 7:3, 6:4, 5:5, 4:6, 3:7, 2:8 and 1:9 ratios of API (A):API (B). The vials with the mixtures were then shaken by hand to mix the components thoroughly and analysed using Differential Scanning Calorimetry (DSC).

2.3. Analytical instrumentation

2.3.1. Attenuated total reflectance - Fourier Transform Infra-red (ATR-FTIR) spectrometer

FTIR is used to analyse materials by recording changes in vibrational energy (vibrational mode) of chemical bonds induced by infrared radiation. The resultant “fingerprint IR” spectrum is due to the fact that different bonds and functional groups absorb infrared radiation at different frequencies.[1] FTIR was used to determine whether any changes in the vibrational modes of particular functional groups had occurred following grinding or co-precipitation. Spectra were collected using a Perkin Elmer spectrum 100 FTIR (Perkin Elmer, South Africa) fitted with attenuated total reflectance (ATR), which enables samples to be scanned directly in solid or liquid state without further preparation. Software used for data collection was Perkin Elmer spectrum software (v 10.6.2.1159). The window of collection was 4000 – 400 cm^{-1}, using 32 scans at a scan speed of 0.2 cm/s. The ground powder was scanned after grinding without any further sample preparation. Crystals were picked from the mother liquor and dried on filter paper before collection of the spectra.

2.3.2. Thermal analysis

Thermal analysis involves methods in which the physical and/or chemical properties of a sample are monitored as a function of temperature, while the sample is exposed to a controlled temperature

programme.[2] The methods used in these studies were Differential Scanning Calorimetry (DSC) and Thermogravimetric analysis (TGA).

2.3.2.1. Differential scanning calorimetry (DSC)

Power compensation DSC is a technique used to measure the energy difference input into a sample relative to an inert reference material as a function of temperature, while the sample and reference material are subjected to a controlled temperature programme. If the sample undergoes a thermal transition, a temperature difference between the sample and reference is plotted as heat flow versus temperature. This results in a DSC thermogram with peaks or troughs that indicate whether an exothermic or endothermic thermal event has occured.[3] In this work, DSC was used for determination of the melting point and to monitor polymorphic changes. All DSC analyses were performed using a TA DSC 250 (TA Instruments, New Castle, USA) by means of Trios software v 5.0.0.44608. Samples were placed in aluminium pans which were sealed with a lid, by crimping and sample size ranged between 2-5 mg. The heating rate was 10 K/min, and the purging gas was nitrogen used at a flow rate of 50 mL/min.

a) Construction of the phase diagrams

The phase diagrams in Chapter 5 were constructed using the DSC method, where the first endotherm indicates the solidus temperature and the second endotherm the liquidus temperature. In this study the onset temperatures of the first and second endotherms were used as the solidus and liquidus points, plotted against the mole fraction of one of the components. The eutectic point is the point where the solidus and liquidus lines meet and represents the eutectic composition.

2.3.2.2. Thermogravimetric analysis (TGA)

Thermogravimetry measures the change in the weight of a sample as a function of temperature or time. The weight change is plotted versus temperature to produce a thermogram that reflects the thermal stability as a function of temperature.[3] All TGA analyses were performed on a Perkin Elmer TGA 4000, purchased from Perkin Elmer (South Africa), using Pyris manager software (v 13.1.1.0160). Samples were placed in a ceramic crucible and heated at 15 K/min. The sample masses ranged between 2-5 mg. Nitrogen was used as a purging gas at a flow rate of 20 mL/min.

2.3.3. Powder X-Ray diffraction (PXRD)

Powder X-ray diffraction (PXRD) is a non-destructive method used to characterise crystalline material providing information on crystal structure, phase, preferred orientation and particle size, etc.[4] PXRD patterns were collected using a Bruker D2 phaser 2nd generation (Bruker, Karlsruhe, Germany) that is fitted with a CuKα radiation source and Lynxeye detector. The wavelength of radiation was 1.54184 Å and produced at 30 kV and 10 mA. A 2θ range of 5-60º was used with step size of 0.04º. PSD opening was set to 4.859º. A small quantity of sample was packed into a steel sample holder with a 25 mm sample cavity diameter. PXRD was used to verify cocrystallisation of the API and coformer

after grinding. This was determined by comparing the PXRD pattern of the ground powder to the sum of the PXRD patterns of the API and coformer, where the sum of the individual patterns represents the physical mixture.

2.3.4. Single-crystal X-Ray diffraction (SCXRD)

Single-crystal X-ray diffraction (SCXRD) is used to elucidate the molecular structure of a compound. Single crystals were mounted on a 35 micron MiTeGeN micro loop and coated in immersion oil (Type NVH). SCXRD data for each cocrystal was collected on Bruker D8 venture equipped with Cu and Mo micro sources (IμS), Bruker (Karlsruhe, Germany). Radiation was produced at 50 kV and 1.4 mA with wavelength of 0.71073 Å. APEX 4 software (2021.10-0) was used for single crystal data collection. Unit cell dimensions were determined at both ambient (298 ± 2 K) and low temperature (100 ± 2 K) to detect possible changes in the unit cell dimension as a result of changing temperature. All data were collected at 100 ± 2 K and the low temperature was maintained by cooling the crystals with a continuous stream of nitrogen gas at a flow rate of 20 mL/min with the help of a Cryostream cooler (Oxford Cryosystems UK). Both ϕ (phi) and ω (omega) scans were recorded.

Data reduction was carried out by means of the standard procedure using the Bruker software package SAINT[5] and absorption correction and the correction of other systematic errors was performed in SADABS[6] using the multi-scan method within APEX4.[7] The structures were solved by direct methods using SHELXT[8] and refined using SHELXL[9]. X-Seed[10,11] was used as the graphical interface for the SHEXL program suite, which was used to solve the crystal structures by direct methods and for refinement by means of least-squares minimisation. Hydrogen atoms were placed using riding model constraints. PLATON[12] was used to prepare supplementary information for each of the structures.

Mercury[13,14] (v 2020.3.0) was used for computing the powder patterns of the salts using the SCXRD data.

POV-Ray[15] is a tracer program employed here for image generation based on the crystal structure models. All molecular structural and packing diagrams were produced using POV-RAY. (http://www.povray.org/documentation/view/3.6.017/).

References

(1) Skoog D. A., West D. M., Holler F. J. and Crouch S. R. *Fundamentals of Analytical Chemistry*, 10th ed.; Saunders College, **2014**.

(2) Giron D. Applications of Thermal Analysis and Coupled Techniques in Pharmaceutical Industry. *J. Therm. Anal. Calorim.* **2002**, 68, 335-357.

(3) Mendham J., Denney R. C., Barnes J. D. and Thomas M. J. K. *Textbook of Quantitative Chemical Analysis*, 6th ed.; Pearson Education Limited: England, **2000**.

(4) *XRD*. EAG Laboratories. https://www.eag.com/techniques/spectroscopy/x-ray-diffraction-xrd/ (accessed 2023-03-06).

(5) *SAINT V8.37A*, Bruker AXS, Inc.: Madison, WI, **2016**.

(6) *SADABS*, Bruker AXS Inc.: Madison, WI, **2016**.

(7) *APEX4, SAINT, and SADABS*, Bruker AXS Inc.: Madison, WI, **2016**.

(8) Sheldrick G. M. *SHELXT* - Integrated space group and crystal structure determination. *Acta. Cryst.* **2015**, *A71*, 3–8.

(9) Sheldrick G. M. Crystal structure refinement with *SHELXL*. *Acta. Cryst.* **2015**, *C71*, 3–8.

(10) Barbour L. J. X-Seed — A Software Tool for Supramolecular Crystallography. *J. Supramol. Chem.* **2001**, *1*, 189–191.

(11) Atwood J. L. and Barbour L. J. Molecular Graphics: From Science to Art. *Cryst. Growth Des.* **2003**, *3*, 3–8.

(12) Spek A. L. Single-crystal structure validation with the program PLATON. *J. Appl. Cryst.* **2003**, *36*, 7–13.

(13) Macrae C. F., Bruno I. J., Chisholm J. A., Edgington P. R., McCabe P., Pidcock E., Rodriguez-Monge L., Taylor R., van de Streek J. and Wood P. A. *Mercury CSD 2.0* – New Features for the Visualization and Investigation of Crystal Structures. *J. Appl. Cryst.* **2008**, *41*, 466–470.

(14) Macrae C. F., Edgington P. R., McCabe P., Pidcock E., Shields G. P., Taylor R., Towler M. and Van De Streek, J. *Mercury*: Visualization and Analysis of Crystal Structures. *J. Appl. Cryst.* **2006**, *39*, 453–457.

(15) POV-RAY™ for Windows Version 3.7.0.msvc10win64 copyright © (1996-2013), Persistence of Vision Raytracer PTY. LTD.

Chapter 3: Co-crystals of 4-aminosalicylic acid

3.1. Introduction

4-aminosalicylic acid (PAS) is an effective second line anti-tuberculosis drug used in the treatment of multi-drug resistant tuberculosis (defined as resistance to at least isoniazid and rifampicin). However, it has the disadvantages of low solubility, susceptibility to thermal degradation and it is chemically unstable meaning it undergoes decarboxylation in an acidic medium forming toxic m-aminophenol.[1–3] Isoniazid (INH) and pyrazinamide (PYR) are first line drugs used in the treatment of TB and much like PAS, they also have challenges of solubility (in the case of PYR), hepatotoxicity and neuropathy induced by INH.[4,5] Pyrazinecarboxylic acid (PCBA) is the active metabolite of PYR, a compound that exhibits antimycobacterial activity, making it a suitable candidate for cocrystallisation with other active pharmaceutical ingredients (API).[6] Cocrystallisation has emerged as a suitable approach to mitigate these challenges owing to the proven ability of fine tuning the properties of the API *via* this method. Several cocrystals of 4-aminosalicylic acid, isoniazid and pyrazinamide have been reported with other API and excipients, summarized by Salem *et al.* [4] The resultant cocrystals show enhanced solubility and improved chemical properties of the APIs (including stabilization of PAS).

3.2. Present study

Cocrystal preparation of PAS with INH, PYR and PCBA was carried out by methods described previously in Chapter 2. The choice of solvents for liquid assisted grinds (LAGs) was guided by the available literature on PAS cocrystals and selecting solvents that have been shown to yield positive results, are considered to be green solvents and are pharmaceutically acceptable.[4] The same solvents were used for all subsequent liquid-assisted grinds throughout this dissertation. Two cocrystals of PAS with INH and PYR and a multicomponent product of PAS and PCBA will be analysed in this chapter; molecular structures of the starting materials are shown in **Figure 1**. Summarized in **Table 1** are the cocrystals covered in this chapter and synthetic methods.

Table 1: Summary of compounds synthesized for this work.

Compound	Nature	Synthesis methods			Reported
		Neat	LAG	Solvent recryst.	
PAS-INH	Cocrystal	✓	MeOH, H_2O, MeCN and EtOAc	MeOH	Drozd *et al.*,[1] Grobelny *et al.*,[7]
PAS-PYR	Cocrystal	✓	MeOH, H_2O, MeCN and EtOAc	MeOH	Drozd *et al.*,[1] Grobelny *et al.*,[7]
PAS-PCBA	Cocrystal/Salt?	✓	MeOH, H_2O, MeCN and EtOAc	MeOH	This work

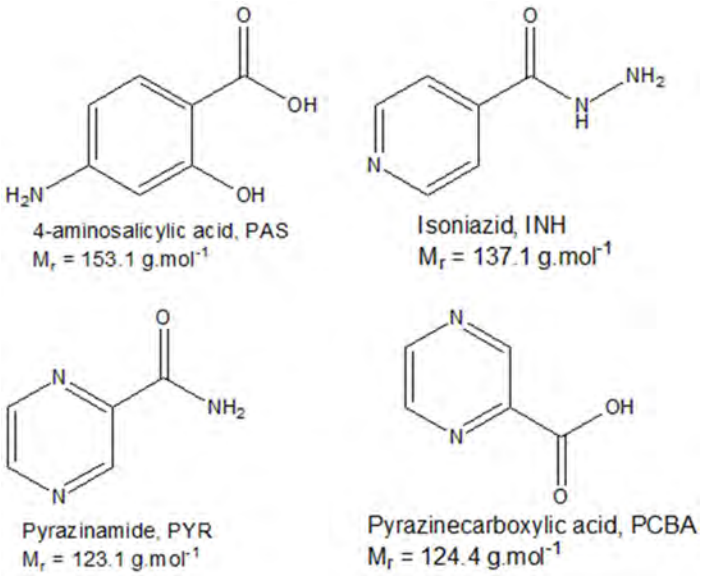

Figure 1: Molecular structures and acronyms of the compounds reported in this chapter.

3.2.1. PAS-INH cocrystal

This cocrystal has previously been synthesized[1,7] and in this work LAG experiments were conducted with two polar and two apolar solvents and a neat grind to determine if different phases could be obtained. The PAS-INH cocrystal was prepared by grinding equimolar quantities of PAS (0.1 mmol, 150 mg) and INH (0.1 mmol, 135 mg) using a mechanical ball mill. The LAG samples were prepared by adding 3 drops (~15 µL) of solvent to the mixture before grinding while neat grinding involved no addition of solvent.

3.2.2.1. Characterization

3.2.2.1. A) ATR-FTIR spectra of PAS-INH cocrystal ground samples and crystalline material

The FTIR spectra of the individual starting materials were obtained and used as reference to determine cocrystal formation. The spectra are depicted in **Figure 2** together with the spectra for NG, LAG samples and bulk crystalline material.

PAS exhibits two stretching bands for NH_2 centred at 3494 and 3387 cm^{-1}, a carbonyl stretch C=O at 1615 cm^{-1} and a broad OH band between 3095-2452 cm^{-1}. The spectrum generated by INH is characterised by two stretching bands for NH_2 at 3306 and 3108 cm^{-1} and an amide stretching carbonyl at

1663 cm^{-1}. The amines belonging to both PAS and INH have been maintained in all samples at slightly shifted peak positions due to hydrogen bonding (see **Table 2**). In the carbonyl region (1626-1680 cm^{-1}), there are three distinct peaks in all samples except for LAG_{EtOAc}, which is possibly a combination of the peaks belonging to INH and PAS. The broad OH band of PAS is less intense in all samples as a result of hydrogen bonding to the nitrogen atom in the pyridine ring of INH. The appearance of a new broad absorption peak at 1950 cm^{-1} further indicates the hydrogen bonding effect. The LAG_{EtOAc} sample shows more characteristics of PAS possibly owing to the presence of unreacted material. **Table 2** summarises the shifts in wavenumbers for the various vibrational modes.

Table 2: Summary of the band shifting in the spectra of the cocrystals obtained from the different preparation.

Vibrational Modes	PAS/cm^{-1}	INH/cm^{-1}	Neat/cm^{-1}	H_2O/cm^{-1}	MeOH/cm^{-1}	EtOAc/cm^{-1}	MeCN/cm^{-1}	SC*/cm^{-1}
νNH_2	3494, 3387	-	3493, 3388	3363	3491, 3363	3491, 3386	3493, 3386	3442, 3359
νNH_2	-	3306, 3108	3306, 3100	3303, 3097	3303, 3095	3303, 3097	3303, 3097	3301, 3106
νC-O	1198	-	1200	1177	1199	1223	1199	1178

SC*: bulk crystalline material

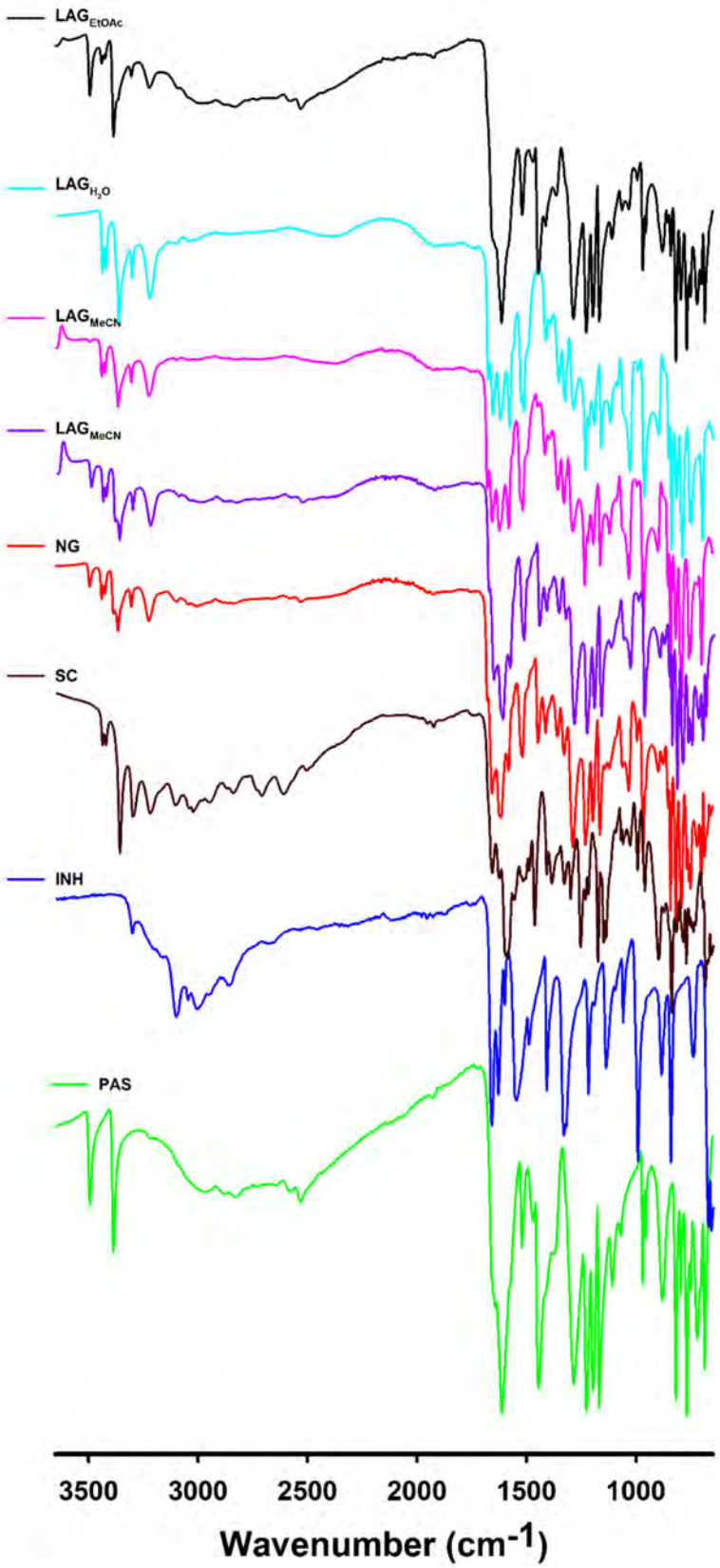

Figure 2: ATR-FTIR spectra of the starting materials, PAS and INH, bulk crystalline material, NG, LAG_{H2O}, LAG_{MeOH}, LAG_{EtOAc}, and LAG_{MeCN}.

3.2.2.1. B) PXRD patterns for the NG, LAG samples and crystalline material

PXRD of the ground samples (NG and LAG) were performed to confirm phase purity and to determine if different phases had been formed from grinding with different solvents. The PXRD patterns in **Figure 3** show that the products have significant similarity to each other irrespective of the method of synthesis, suggesting that the synthetic method does not affect the nature of the product resulting in the same phase. The PXRD patterns of the ground samples have a close resemblance to the physical mixture with differences in the intensities of the major peaks at 17 and 25-27º (2θ). The peak at 7º (2θ) is maintained in the all samples except the LAG_{H_2O} sample; however, it is not very intense in the LAG_{MeOH} and LAG_{EtOAc}. The similarities of the ground samples to the physical mixture could indicate unreacted material.

The diffractogram of the bulk crystalline material was not included because the PXRD instrument was offline by the time that the crystals were obtained, hence only the calculated pattern has been used for comparison. The calculated PXRD pattern based on single-crystal diffraction data is shown in **Figure 3** for comparison to the ground samples. It is evident that the calculated PXRD pattern matches the ground samples, showing that the single crystal is consistent with PXRDs of the bulk material. Moreover, the calculated PXRD pattern from this work is similar to those reported by Drozd *et.al*.[1] and Grobelny *et al*.[7] Presented in **Figure 4** is the reported and calculated PXRD patterns illustrating the perfect correlation between the calculated pattern and the reported data.

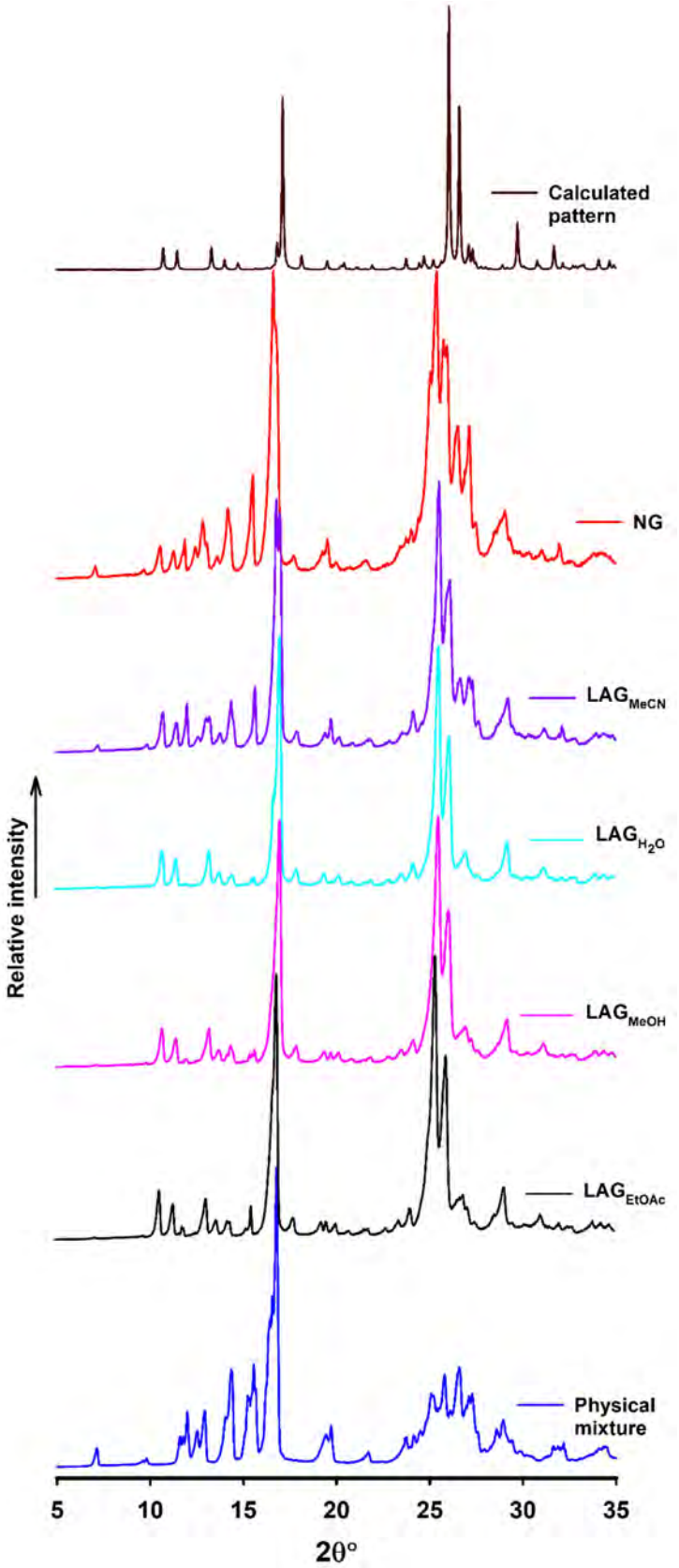

Figure 3: PXRD patterns for the physical mixture, NG, LAG_{H_2O}, LAG_{MeOH}, LAG_{EtOAc}, LAG_{MeCN} and calculated PXRD pattern.

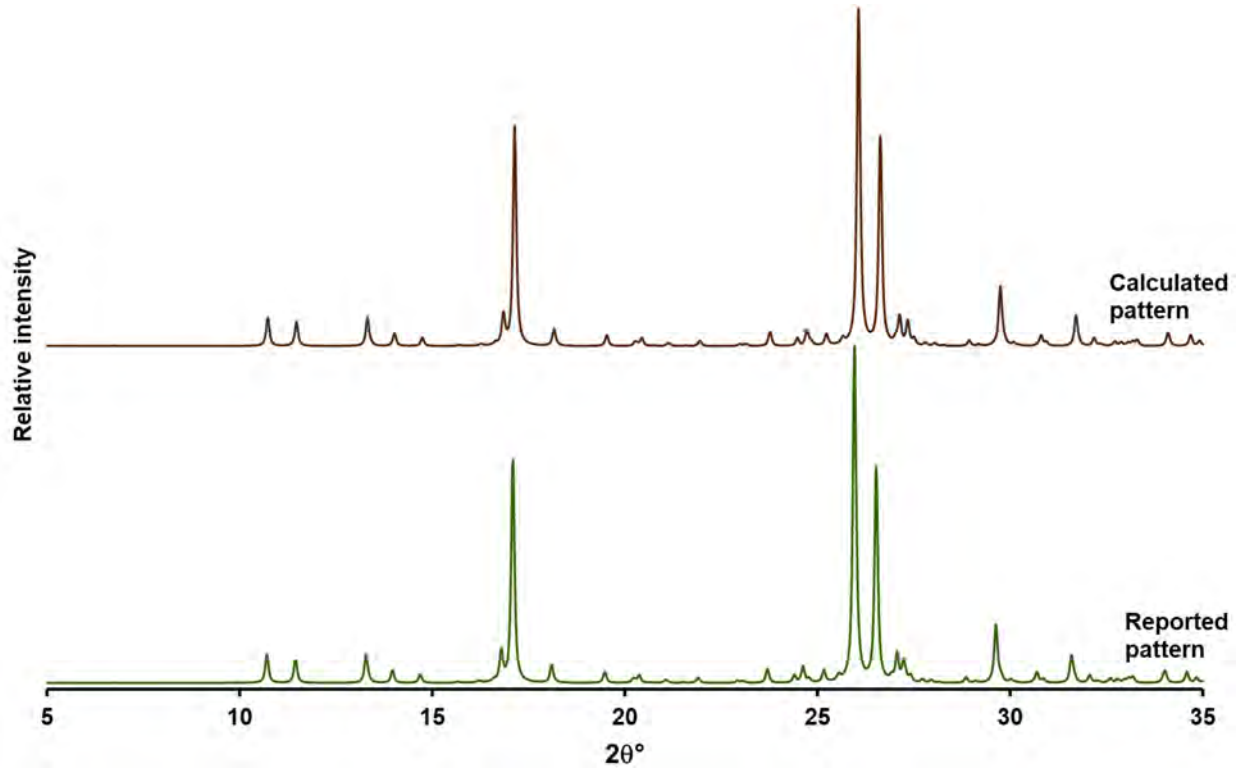

Figure 4: PXRDs for PAS-INH reported by Grobelny *et al*. (Refcode: URUDER, bottom)[7] in comparison with the calculated pattern from this work.

3.2.2.1. C) Thermal analysis of PAS-INH

DSC thermograms of starting materials PAS and INH have melt endotherms in the range 133.9-140.7 °C for PAS and 169.7-171.7 °C for INH. The melting point of the NG is 140.2-145.7 °C and lies between both starting materials indicating the formation of a different product, see **Figure 5 (A)**. The LAG samples also show similar melting point ranges, 138.9-146.9 °C (**Figure 5 (B)**), suggesting that the products have the same phase. The TGA thermograms in **Figure 6 (A)** show no evidence of included solvent for any of the samples since there is no significant mass loss evident. The DSC thermograms are consistent with those obtained by Drozd *et.*al.[1] and Grobelny *et al*.[7]; which is indicative of consistency in preparation even when it is prepared using the solvent free method.

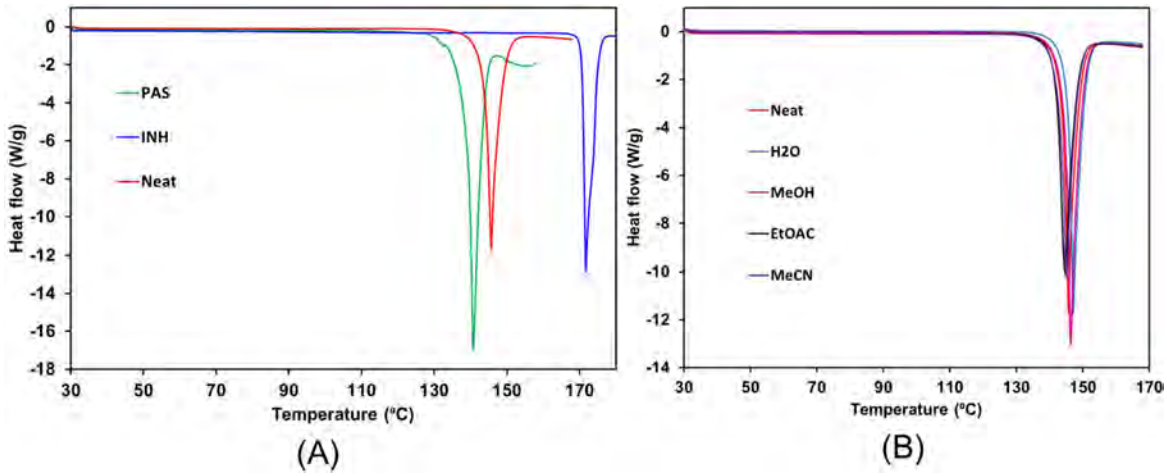

Figure 5: (A) DSC showing melting points of the starting materials (PAS and INH) and the NG sample. (B) DSC showing melting points for the NG, LAG_{H2O}, LAG_{MeOH}, LAG_{EtOAc}, and LAG_{MeCN} (exo↑).

The DSC and TGA thermograms, **Figure 6 (B)**, of the bulk crystalline material show a slightly lower melting point range, compared to the ground samples of 130.1-140.8 °C and has no included solvent. The melting points between the bulk crystalline material and the ground samples is about 5-8 °C which can be significant enough to indicate a new phase. This can only be verified by comparing the PXRD patterns; however, the PXRD data of the bulk crystalline material could not be collected as stated previously. The melt onset and peak temperatures of the NG, the LAG samples and bulk crystalline material are presented in **Table 3**.

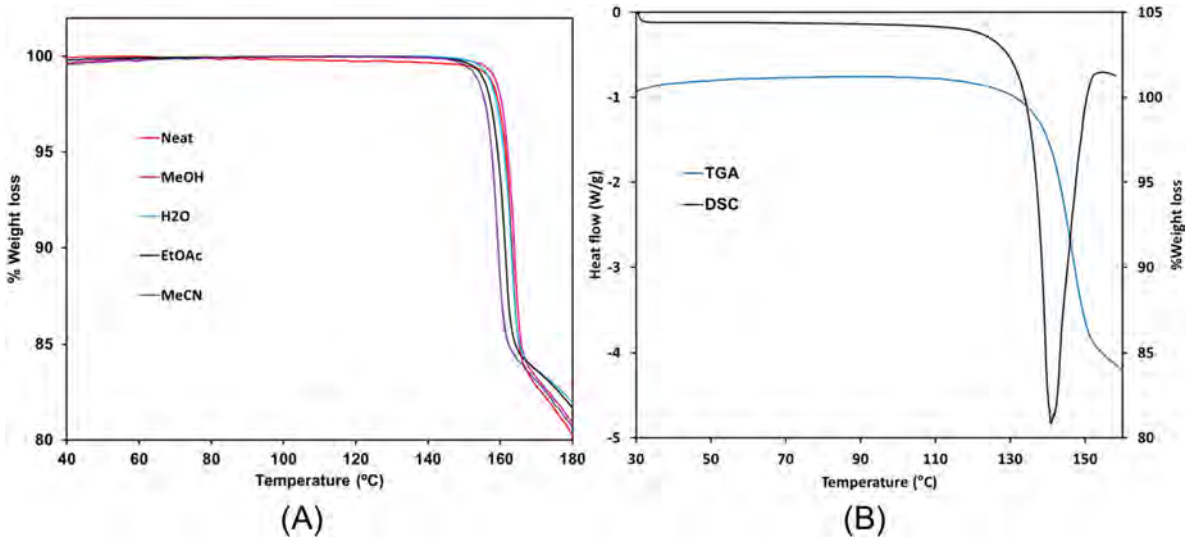

Figure 6: (A) TGA thermograms for the NG, LAG_{H2O}, LAG_{MeOH}, LAG_{EtOAc}, and LAG_{MeCN}. (B) Overlaid DSC and TGA thermograms of the bulk crystalline material.

Table 3: Melt onset and peak temperatures of the ground samples and crystalline material.

Sample	Refcode	T_{onset} (°C)	T_{peak} (°C)
Grobelny *et al*.,[4]	URUDER	-	142.0
Drozd *et.*al.,[1]	-	141.4	-
NG	This work	140.2	145.7
LAG_{H2O}	This work	142.1	146.9
LAG_{MeOH}	This work	140.9	145.8
LAG_{EtOAc}	This work	139.3	144.8
LAG_{MeCN}	This work	139.9	145.2
SC	This work	130.1	140.8

3.2.2.1. D) Single-crystal X-ray diffraction analysis of PAS-INH bulk crystalline material

Crystals suitable for single crystal X-ray diffraction were obtained *via* slow evaporation by dissolving equimolar amounts of PAS (0.1 mmol, 51.0 mg) and INH (0.1 mmol, 39.7 mg) in methanol at room temperature.

i. Data collection and space group determination

Unit cell parameters, crystal system, space group and single crystal data were collected on a Bruker D8 Venture diffractometer using MoKα radiation of wavelength 0.71073 Å. The PAS-INH cocrystal crystallises in the space group $Pna2_1$.

ii. Structure solution and refinement

SHELXT[8] was used for structure solution and SHELXL[9] for refinement of PAS-INH. All atoms were refined anisotropically based on well-behaved isotropic temperature factors and hydrogen atoms were placed in idealized positions in a riding model. For heteroatoms, hydrogen atoms were refined using peaks observed from the difference Fourier map. Data collection and refinement parameters for PAS-INH are reported in **Table 4**.

Table 4: Structure solution and refinement parameters for PAS-INH cocrystal.

Data-collection and refinement parameters	
Formula unit	$2(C_6H_9N_3O)$, $2(C_7H_5NO_3)$
Formula mass (g mol^{-1})	580.56
Crystal system	Orthorhombic
Space group	*Pna*2$_1$ (No. 33)
a/Å	21.7749 (8)
b/Å	16.4725(6)
c/Å	7.1953(2)
α/°	90
β/°	90
γ/°	90
Volume (Å^3)	2580.86 (15)
Z	4
D_{calc} (g cm^{-3})	1.494
F (000)	1216
μ (MoKα) (mm^{-1})	0.114
Crystal size (mm^3)	0.19 x 0.22 x 0.37
Temperature (K)	100
Range scanned θ (º)	2.2 - 28.3
Index ranges	-29: 29 ; -21: 21 ; -9: 9
Total number of reflections collected	59194
Number of unique reflections	6210
Number of reflections with I > 2σ (I)	5300
Number of least-squares parameters	436
R_{int}	0.072
S	1.04
R_1 (I > 2σ (I))	0.0352
wR_2	0.0851
Weighting scheme parameters	a = 0.0396, b = 0.6594
$(\Delta/\sigma)_{mean}$	0.00
Δρ excursions (e Å^{-3})	-0.19, 0.29

iii. Molecular structure and hydrogen bonding schemes

Illustrated in **Figure 7 (A)** is the asymmetric unit of the PAS-INH cocrystal that consists of two molecules of PAS and two molecules of INH. The two INH molecules are arranged in a tail-to-tail manner with homomeric hydrogen bonding between the hydrazide moieties. Each PAS molecule is hydrogen bonded to the terminal N atom of the pyridine ring in each INH molecule *via* the carboxylic acid moiety, see **Figure 7 (B)**. It is noteworthy that the two pairs of COOH···N hydrogen bonds formed between PAS and INH have different bond lengths, where one pair exhibits more ionic character than the other. This was fully discussed by Grobelny *et.al*.[7] who demonstrated the mobility of the carboxylic acid hydrogen atom in a temperature resolved study. This topic will not be covered any further here as it does not form part of the investigation for this study.

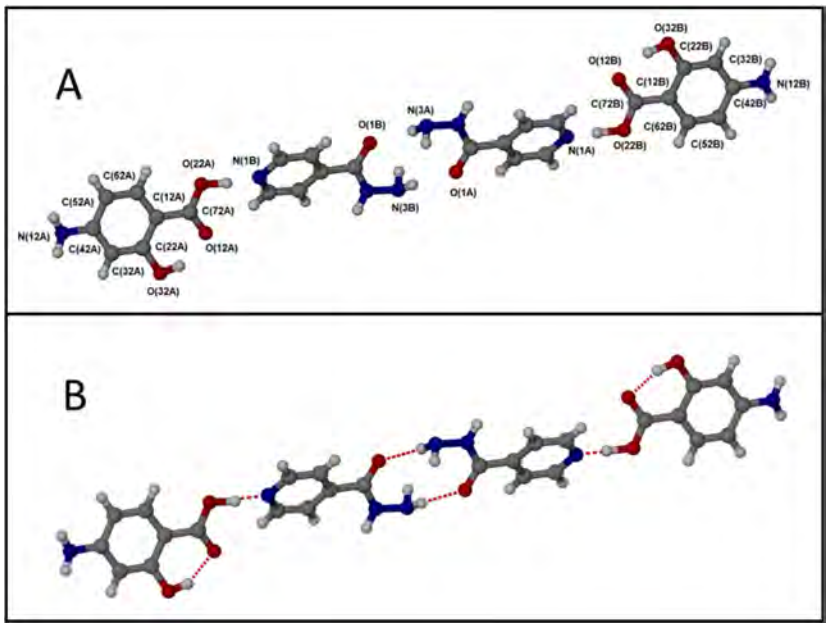

Figure 7: (A) Labelled molecular diagram of the asymmetric unit of PAS-INH. (B) Shows the hydrogen bonding between the PAS and INH molecules.

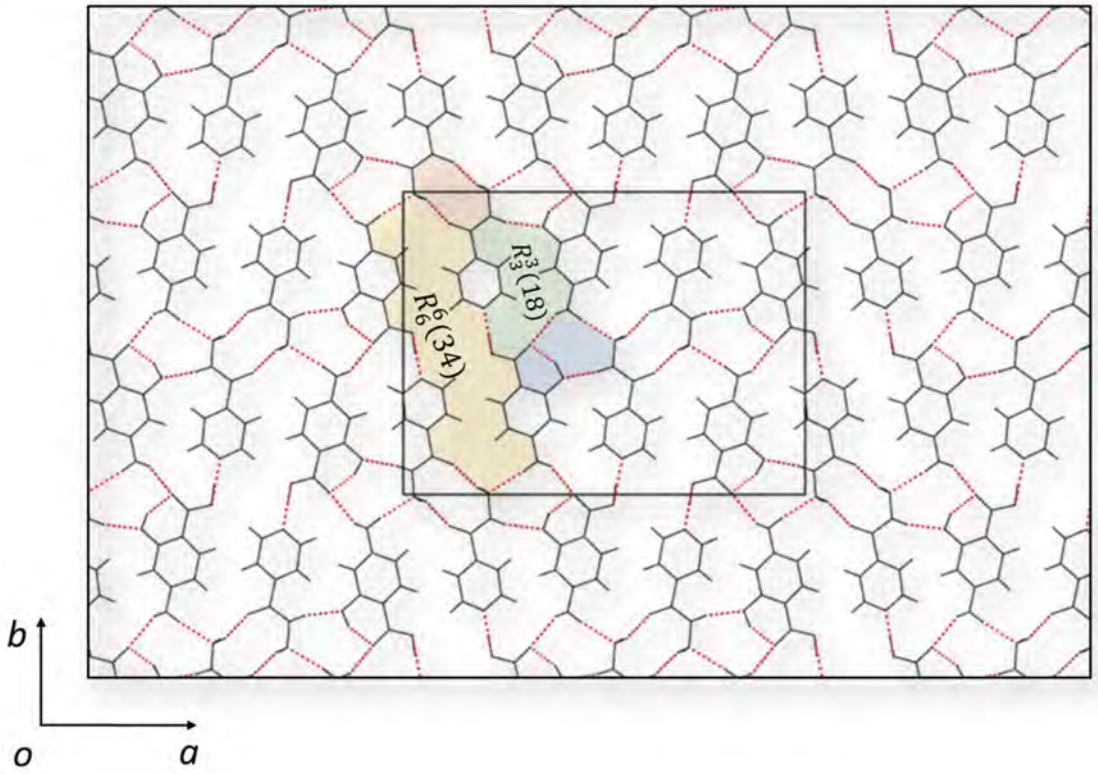

Figure 8: The hydrogen bonding ring motifs of PAS-INH viewed down the *c* axis.

Figure 8 depicts hydrogen bonding between the PAS and INH molecules and shows the two distinct ring motifs generated by hydrogen bonding. Shaded in red is the ring motif formed between two INH molecules through the hydrazide moieties. Shaded in blue is the ring motif formed between two PAS

molecules and one INH molecule. The larger ring shows hydrogen bonding between the amine moiety and hydroxyl group of the PAS molecules and between the amine and amide moieties of the INH. The smaller ring shows intramolecular hydrogen bonding between the carboxylic acid and hydroxyl groups of PAS. The green shaded ring contains 18 atoms, three donor atoms and three acceptor atoms and involves two PAS molecules and one INH molecule ($\boldsymbol{R_3^3(18)}$). The yellow shaded ring motif is made up of 34 atoms, six hydrogen bond donor atoms and 6 acceptor atoms and involves four INH molecules and two PAS molecules ($\boldsymbol{R_6^6(34)}$). All the hydrogen bond interactions and parameters are reported in **Table 5**. The important COOH···(pyridine) interaction bond distances in this cocrystal falls within the average O-H···N H-bond distance of 2.631 Å.[10]

Table 5: Hydrogen bond parameters for the PAS-INH cocrystal.

D-H···A	D-H (Å)	H···A (Å)	D···A (Å)	D-H···A (°)	Symmetry code
N3B- H3BA···O1A	0.97(3)	2.10(3)	3.011(3)	156(3)	.
N3A-H3AA···O1B	0.90(4)	2.13(4)	2.997(3)	160(3)	.
N2A-H2AN···O32A	0.87(3)	2.16(3)	3.009(3)	165(2)	-1/2+x,3/2-y,z
N3A-H3AB···O12B	0.92(4)	2.39(4)	3.203(4)	149(3)	1/2-x,1/2+y,-1/2+z
N3B-H3BB···O32B	0.95(4)	2.54(5)	3.422(3)	155(4)	1/2-x,1/2+y,1/2+z
N2B-H2BN···O32B	0.91(3)	2.14(4)	3.002(3)	159(3)	1/2+x,1/2-y,z
N12A-H12C···N3B	0.90(3)	2.18(3)	3.078(3)	175(3)	x,1+y,z
N12A-H12D···O12B	0.87(4)	2.26(3)	3.017(3)	145(3)	1/2+x,3/2-y,z
N12B-H12E···N3A	0.90(3)	2.27(3)	3.160(3)	175(3)	x,-1+y,z
N12B-H12F···O12A	0.85(3)	2.26(3)	3.037(3)	152(2)	-1/2+x,1/2-y,z
O32A-H22A···O12A	0.90(3)	1.77(3)	2.587(2)	149(3)	.
O32B-H22B···O12B	0.92(3)	1.68(3)	2.546(2)	155(3)	.
O22A-H72A···N1B	1.11(3)	1.46(3)	2.569(3)	173(3)	.
O22B-H72B···N1A	1.19(5)	1.35(5)	2.536(3)	179(6)	.
C3A-H3A···O1B	0.9500	2.3800	3.334(3)	177.00	1/2-x,-1/2+y,-1/2+z

iv. Crystal packing

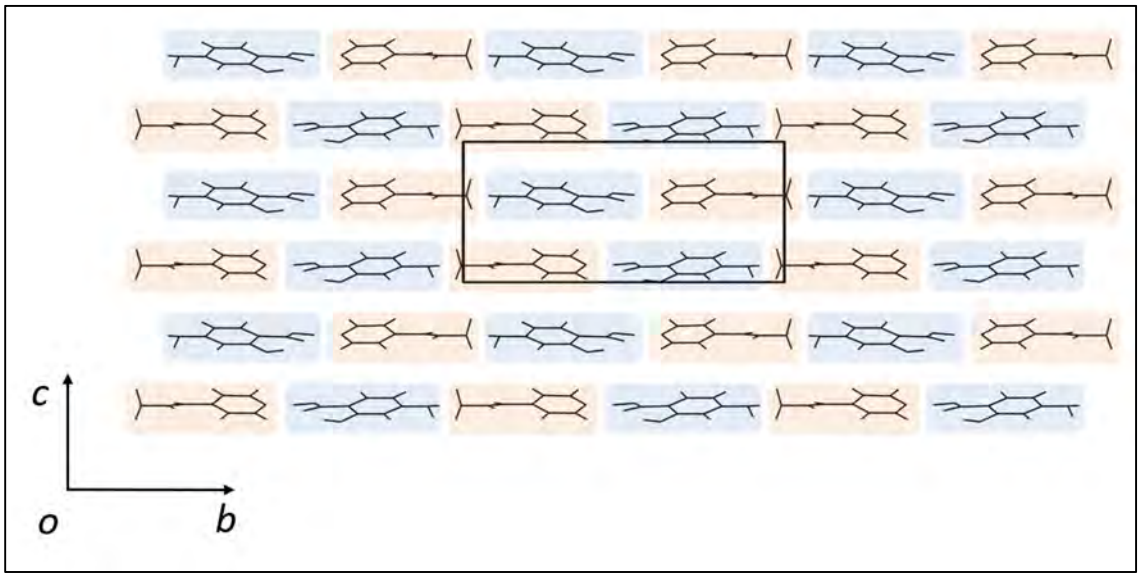

Figure 9: View down the *a* axis showing rows of alternating PAS and INH molecules parallel to the *b* axis.

Shown in **Figure 9** is the packing arrangement of PAS-INH where alternating PAS and INH molecules are arranged in layers stacked parallel to the *a* axes. Moreover, the consecutive layers are anti-parallel and displaced relative to each other.

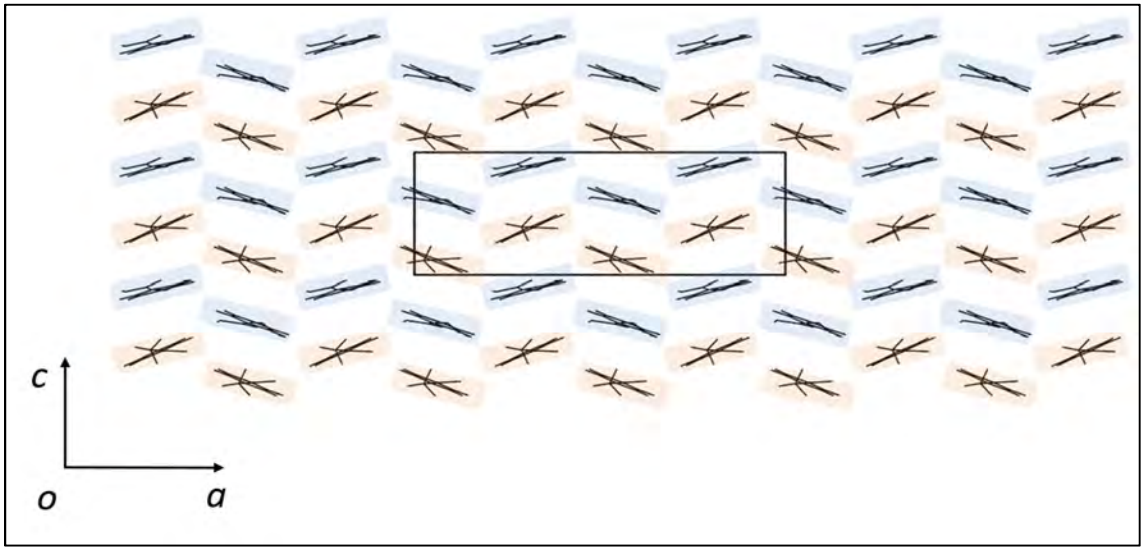

Figure 10: Consecutive columns of alternating PAS and INH molecules stacked parallel to the *c* axis.

Figure 10 shows columns of alternating PAS and INH molecules that are stacked parallel to the *c* axis and along the *a* axis. Consecutive columns have an opposite alternate inclination to the *a* axis.

3.2.2. PAS-PYR·H_2O

The PAS-PYR·H_2O cocrystal was previously synthesised by Grobelny *et al.*,[4] Drozd *et al.*,[1] and Zhang *et al.*,[11]. Of particular interest to us was the fact that they used different solvent systems to obtain the same cocrystal. Grobelny *et al.*,[7] obtained the cocrystal from MeOH while Drozd *et al.*,[1] and Zhang *et al.*,[11] obtained it from H_2O. Neat and LAG methodologies with two polar and two apolar solvents were attempted to reproduce the cocrystal to see if different or similar results would be obtained. The cocrystal was prepared by grinding equimolar amounts of PAS (0.49 mmol, 75 mg) and PYR (0.49 mmol, 60mg) in a mechanical ball mill. The LAG samples were prepared by adding 3 drops (~15 µL) of solvent before grinding and neat grinding involved no addition of solvent.

3.2.2.1. Characterization

3.2.2.1. A) ATR-FTIR spectra for PAS-PYR·H_2O

FTIR spectra of pure PAS, PYR and LAG samples are presented in **Figure 11** and reveal that there are no significant shifts of the peak positions in the ground samples, but the samples have combined properties of both starting materials. PYR is characterized by two amide stretching bands at 3410 and 3294 cm^{-1} and a stretching carbonyl band at 1705 cm^{-1}. The amine and amide bands from PAS and PYR are maintained in all samples with very small changes of the peak positions. The ground samples also show presence of the carbonyl moieties of both parent compounds with slight shifts in peak position. However, this is not exhibited in the LAG_{H2O} sample, it only shows the carbonyl peak for PAS. The broad OH band (3095-2452 cm^{-1}) of PAS is still maintained in all ground samples. This could imply that no hydrogen bonds have been formed between the two molecules and the observed band shifts are as a result of the changed chemical environment. **Table 6** summarises the shifts in wavenumbers of the relevant functional groups.

Table 6: Summary of the band shifting in the spectra of PAS-PYR·H_2O samples.

Vibrational mode	PAS/cm^{-1}	PYR/cm^{-1}	Neat/cm^{-1}	H_2O/cm^{-1}	MeOH/cm^{-1}	EtOAc/cm^{-1}	MeCN/cm^{-1}
νNH_2	3494, 3387	-	3496, 3388	3495, 3388	3496, 3388	3496, 3388	3495, 3387
νNH_2	-	3410, 3294	3414, 3294	3431, 3301	3413, 3294	3414, 3292	3416, 3303
νC=O	-	1705	1712	-	1709	1710	1713
νC=O	1613	-	1613	1616	1612	1613	1614

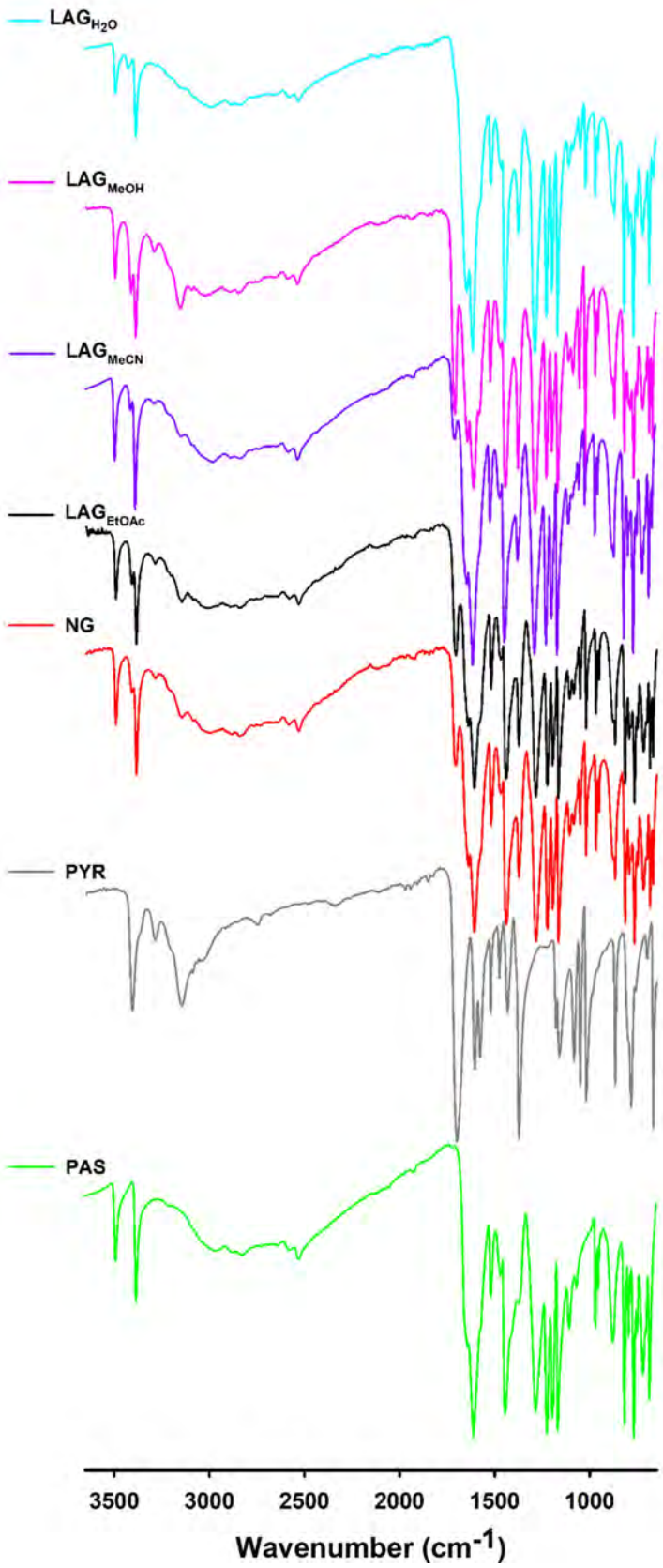

Figure 11: ATR-FTIR spectra for PAS, PYR, NG, LAG_{H_2O}, LAG_{MeOH}, LAG_{EtOAc} and LAG_{MeCN}.

3.2.2.1. B) PXRD patterns of PAS-PYR·H_2O

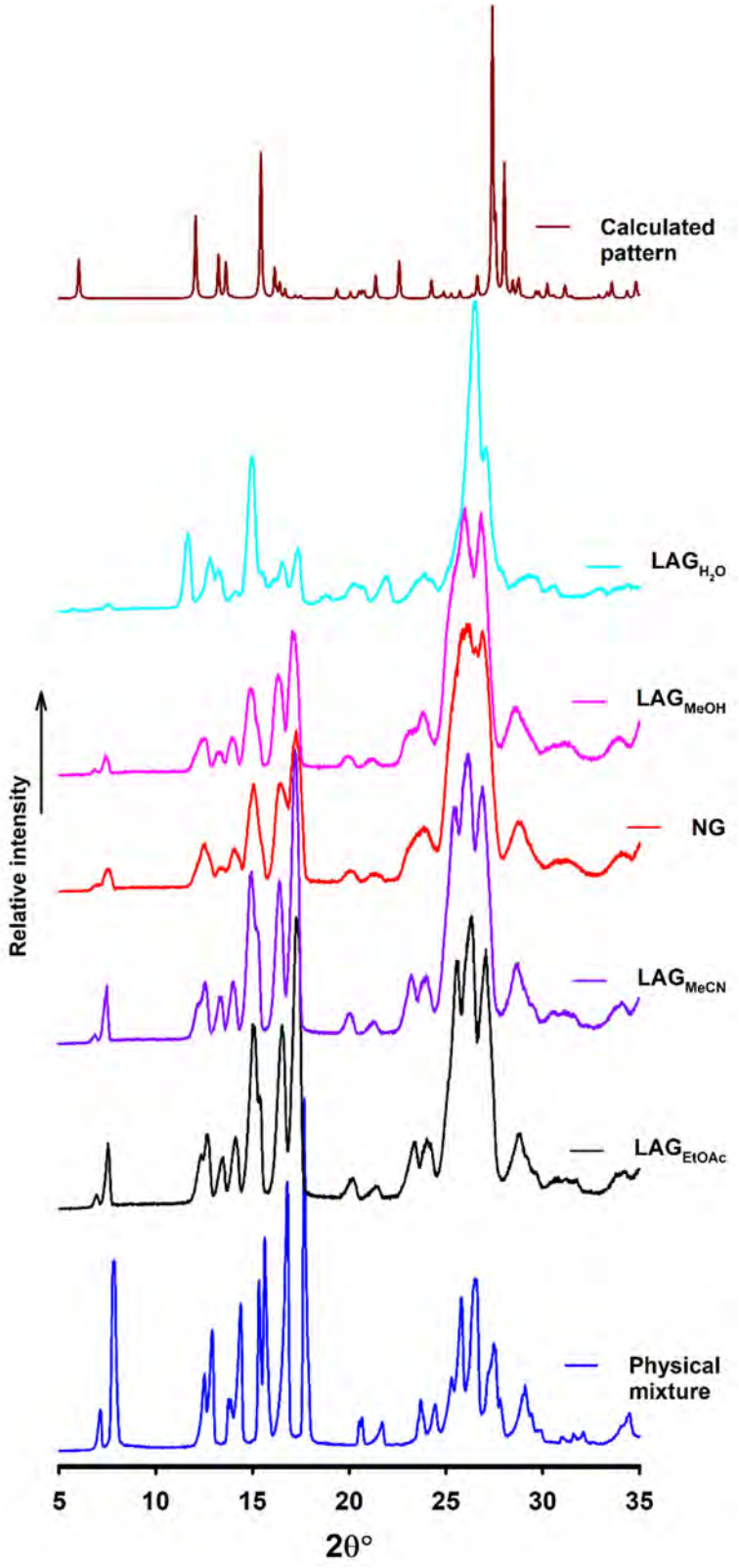

Figure 12: PXRD patterns for the physical mixture, NG, LAG_{H2O}, LAG_{MeOH}, LAG_{EtOAc}, LAG_{MeCN} and calculated pattern.

PXRD was performed to confirm presence of new phases and as can be seen in **Figure 12,** all samples show some similarity to the diffractogram of the physical mixture which suggests the presence of unreacted material. Since crystals of good quality could not be obtained despite the numerous attempts, PXRD analysis of the bulk crystalline material was not done, therefore, only the calculated diffractogram from the single crystal data was included. Only the LAG_{H_2O} PXRD pattern shares some similarities with the calculated pattern while still being similar to the PXRD pattern of the physical mixture, This could be due to large amounts of unreacted material present in the sample. The LAG_{MeCN} and LAG_{EtOAc} results in diffractograms that are almost identical to the physical mixture. The calculated PXRD pattern based on the single-crystal X-ray data that was collected matches the PXRD diffractogram reported by Grobelny *et al,*[7] see **Figure 13.**

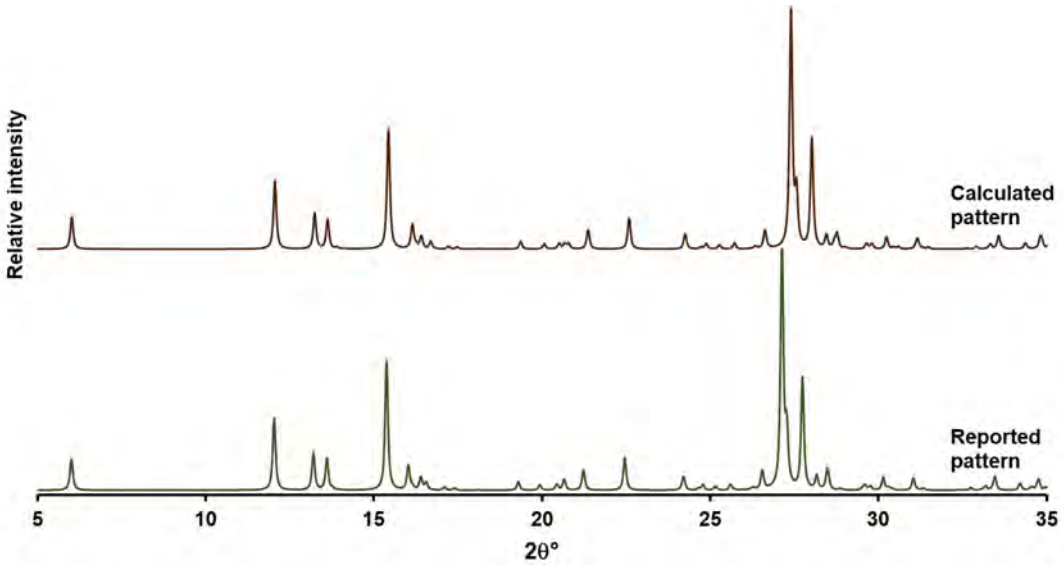

Figure 13: PXRD patterns for PAS-PYR·H_2O reported by Grobelny *et al*. (Refcode: URUGIY)[7] compared to the calculated pattern from this work.

3.2.2.1. C) Thermal analysis of PAS-PYR·H_2O

The DSC thermograms shown in **Figure 14 (A)** reveals that PAS and PYR have melt endotherms in the range 133.9-140.7 °C and 188.9-190.5 °C respectively. The NG has a melting point range of 137.7-143.4 °C, which coincides with the melting point range of PAS. The overlap of melting point ranges complicates the interpretation of thermal analysis and makes it more difficult to determine whether a new phase is present. The samples obtained using the LAG approach also exhibits a similar melting point range to the NG, *i.e*., 134.7-142.7 °C (**Figure 14 (B)**). Apart from the thermogram for LAG_{H2O}, none of the other thermograms show any other thermal events. This is supported by the TGA thermograms (**Figure 15)**, which shows a mass loss between 50-114 °C for the LAG_{H2O} sample and is owing to included water. Melt onset and peak temperatures of the NG and LAG samples are summarized in **Table**

7. The thermal analysis of the bulk crystalline material could not be conducted since crystals of good enough quality for analysis could not be obtained.

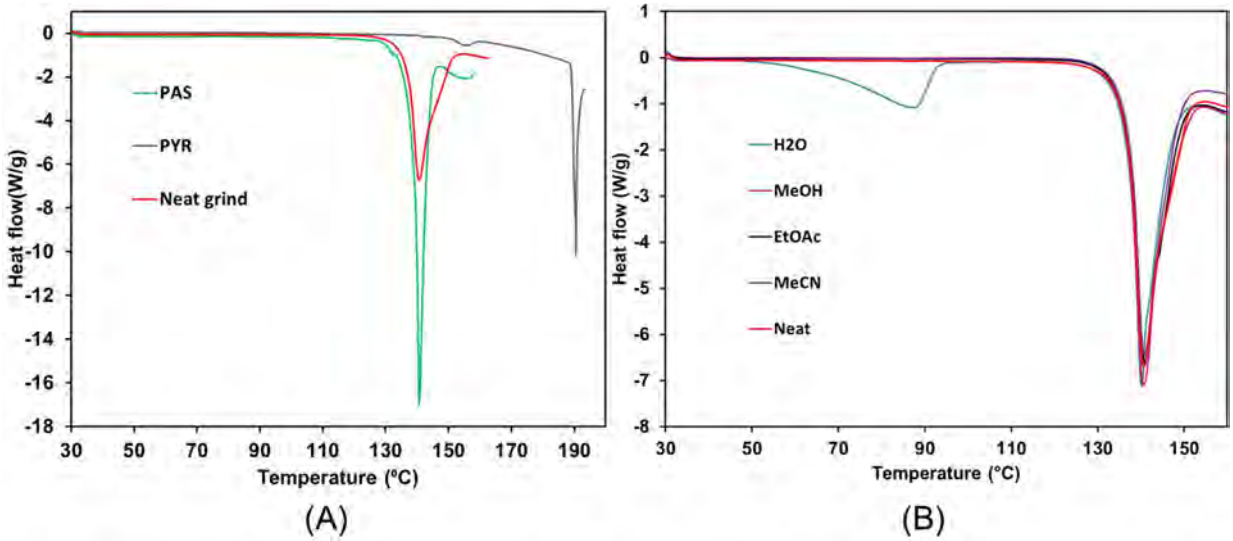

Figure 14: (A) DSC thermograms for PAS, PYR and NG while (B) shows the thermograms for the NG, LAG_{H2O}, LAG_{MeOH}, LAG_{EtOAc}, and LAG_{MeCN} (exo↑).

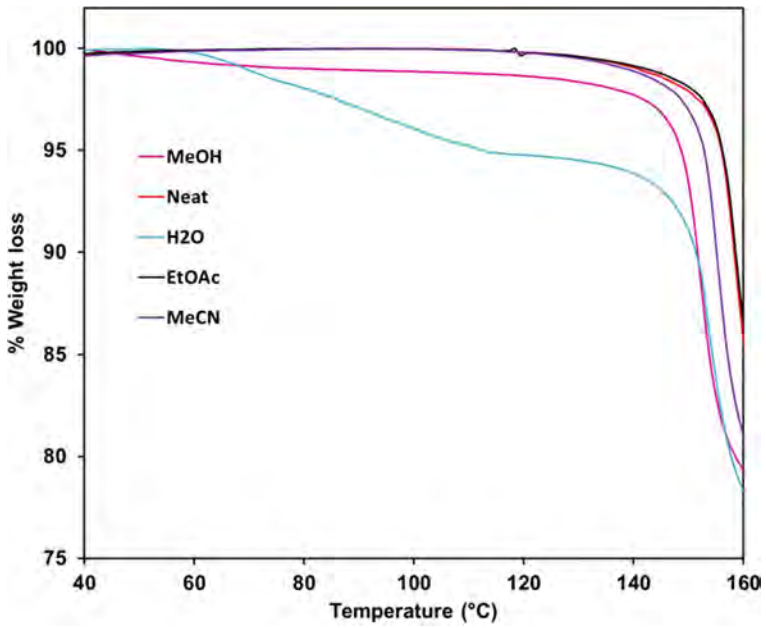

Figure 15: TGA thermograms for the NG (red), LAG_{H2O} (blue), LAG_{MeOH} (pink), LAG_{EtOAc} (black), and LAG_{MeCN} (purple).

Table 7: The melt onset and peak temperatures for PAS-PYR·H_2O samples.

Samples	REFCODE	T_{onset} (°C)	T_{peak} (°C)
Grobelny *et al.*[4]	URUGIY	-	126.0
Drozd *et.al.*[1]	-	132.5	138.0
NG	This work	137.7	143.4
LAG_{H2O}	This work	134.7	141.4
LAG_{MeOH}	This work	136.2	142.5
LAG_{MeCN}	This work	135.7	142.5
LAG_{EtOAc}	This work	135.7	142.7

The melt endotherm data for the results obtained in this study are consistent with the data reported by Drozd *et al.*[1] This is in spite of using two different milling techniques. On the other hand, values obtained in this study were different from the values reported by Grobelny *et al.*[7] To investigate the differences and to verify the work conducted in this study, cocrystal materials were prepared according to the procedures outlined by Drozd *et al*., and Grobelny *et al*.[1,7] Presented in **Figure 16** are the DSC thermograms of the LAG_{H2O} and LAG_{EtOH} samples prepared according to their reported methods. The melting point ranges of the materials prepared, according to the literature procedures, coincide with the melting point range for PAS. The melt endotherm range for LAG_{H2O} is similar to the reported value, while the LAG_{EtOH} peak temperature of 140.8 °C differs from the reported value of 126.0 °C.[1,7]

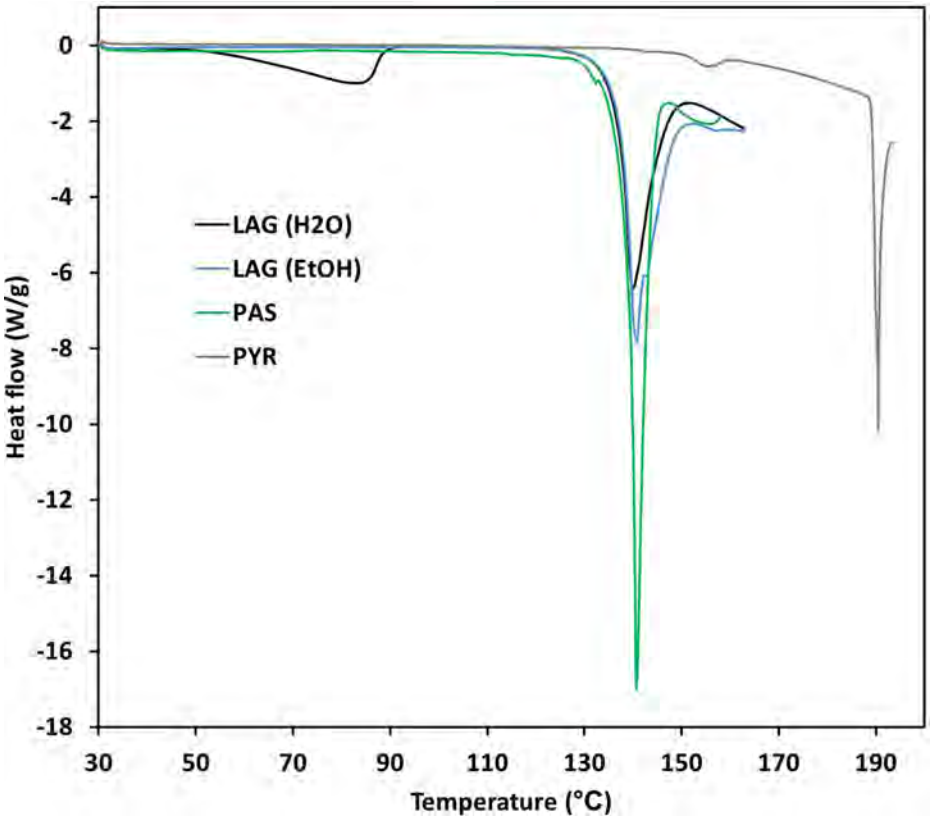

Figure 16: DSC thermograms of the API, PAS and PYR, the ground samples prepared according to the methods described by Drozd *et.al*. (LAG_{H2O}) and Grobelny *et.al*. (LAG_{EtOH}) (exo↑).[1,7]

Crystals of PAS-PYR·H_2O were prepared by slow evaporation using H_2O[1,11] and MeOH[7] as solvent, a few crystals were obtained using MeOH and none using H_2O. Unfortunately, the experiment was not reproducible to make a larger batch for FTIR, PXRD and thermal analysis. Every successive attempt produced only the starting materials. This phenomenon is currently being investigated.

3.2.2.1. D) SCXRD analysis of PAS-PYR·H_2O

Single crystals were prepared by dissolving equimolar amounts of PAS (0.49 mmol, 10.1 mg) and PYR (0.49 mmol, 0.08 mg) in approximately 7 ml of MeOH and stirring the solution at room temperature until the components were fully dissolved. The solution was left to slowly evaporate under ambient conditions. After several attempts to grow the crystals, a single crystal suitable for X-ray diffraction was finally obtained.

i. Data collection and space group determination

Unit cell parameters, crystal system, space group and single crystal data were collected on Bruker D8 Venture diffractometer. The PAS-PYR·H_2O crystallises in the space group *P*-1.

ii. Structure solution and refinement

All atoms were refined anisotropically based on well-behaved isotropic temperature factors while hydrogen atoms were placed in idealised positions in a riding model. For heteroatoms, hydrogen atoms were refined using peaks observed from a difference Fourier map. Data collection and refinement parameters of the PAS-PYR·H_2O can be found in **Table 8**.

Table 8: Data collection and refinement parameters for PAS-PYR·H_2O.

Data-collection and refinement parameters	
Formula unit	$(C_5H_5N_3O)$ $(C_7H_7NO_3)$ H_2O
Formula mass (g mol^{-1})	294.27
Crystal system	triclinic
Space group	*P*-1 (No. 2)
a/Å	6.7085 (3)
b/Å	7.0203 (2)
c/Å	15.0212 (5)
α/°	96.796 (1)
β/°	98.224 (2)
γ/°	105.267 (1)
Volume ($Å^3$)	666.37 (4)
Z	2
D_{calc} (g cm^{-3})	1.467
F (000)	308
μ (MoKα) (mm^{-1})	0.116
Crystal size (mm^3)	0.14 x 0.16 x 0.16
Temperature (K)	100
Range scanned θ (°)	2.8- 27.1
Index ranges	-8: 8; -8: 8; -19: 19
Total number of reflections collected	61268
Number of unique reflections	2927
Number of reflections with I > 2σ (I)	2298
Number of least-squares parameters	224
R_{int}	0.070
S	1.08
R_1 (I > 2σ (I))	0.0374
wR_2	0.1063
Weighting scheme	a = 0.0411, b = 0.4031
$(\Delta/\sigma)_{mean}$	0.00
Δρ excursions (e $Å^{-3}$)	-0.28, 0.22

iii. Molecular structure

The asymmetric unit of PAS-PYR·H_2O (**Figure 17 (A)**) consists of one molecule of PAS, one molecule of PYR and a single molecule of H_2O. PAS and PYR are hydrogen bonded to each other *via* the carboxylic acid moiety (O21) of PAS and one of the nitrogen atoms (N12) in the pyrazine ring. This acid-pyridine interaction falls within the mean interaction distance of 2.631 Å (**Table 9**).[10] This is supported by another weaker C-H···O hydrogen bond formed between O11 and a neighbouring aromatic hydrogen atom on C32 of the PYR molecule. The water molecule is hydrogen bonded to the PYR molecule through an N-H···O hydrogen bond *via* the amide group (**Figure 17 (B)**).

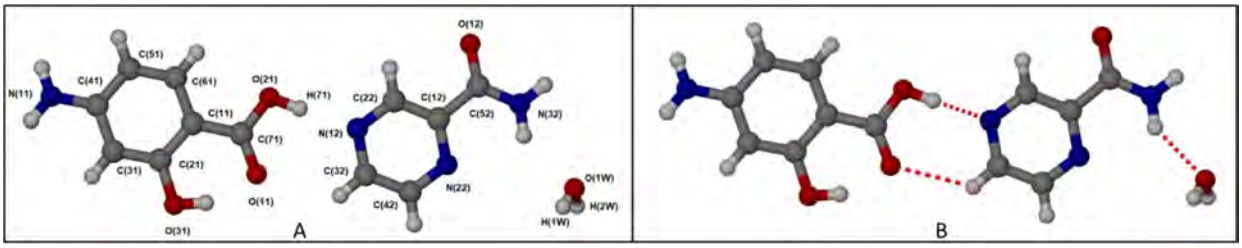

Figure 17: (A) Labelled molecular diagram of PAS-PYR·H_2O and (B) the asymmetric unit showing the hydrogen bonding between the molecules.

iv. Hydrogen bonding and packing arrangement

Depicted in **Figure 18** is a single layer of PAS-PYR·H_2O. The layer shows the hydrogen bonding network that spans the crystal. The repeating motif exhibits a hydrogen bonded ring (shaded blue) that is made up of 40 atoms, seven hydrogen bond donor atoms, eight hydrogen bond acceptor atoms, and involves four PYR molecules, two PAS molecules and three water molecules ($\boldsymbol{R_7^8(40)}$). The water molecules have a dual role and participate as both a hydrogen bond donor and acceptor. It accepts hydrogen bonds from an amine and an amide group of PAS and PYR, respectively, while also serving as a hydrogen bond donor by bonding to the carbonyl moiety of an amide group belonging to a PYR molecule in the same layer. It also hydrogen bonds to a hydroxyl group of a PAS molecule in the layer below (red atoms shown in **Figure 18**). Each PAS molecule has an intramolecular hydrogen bonded ring formed between the hydroxyl moiety and carboxylic acid groups belonging to PAS.

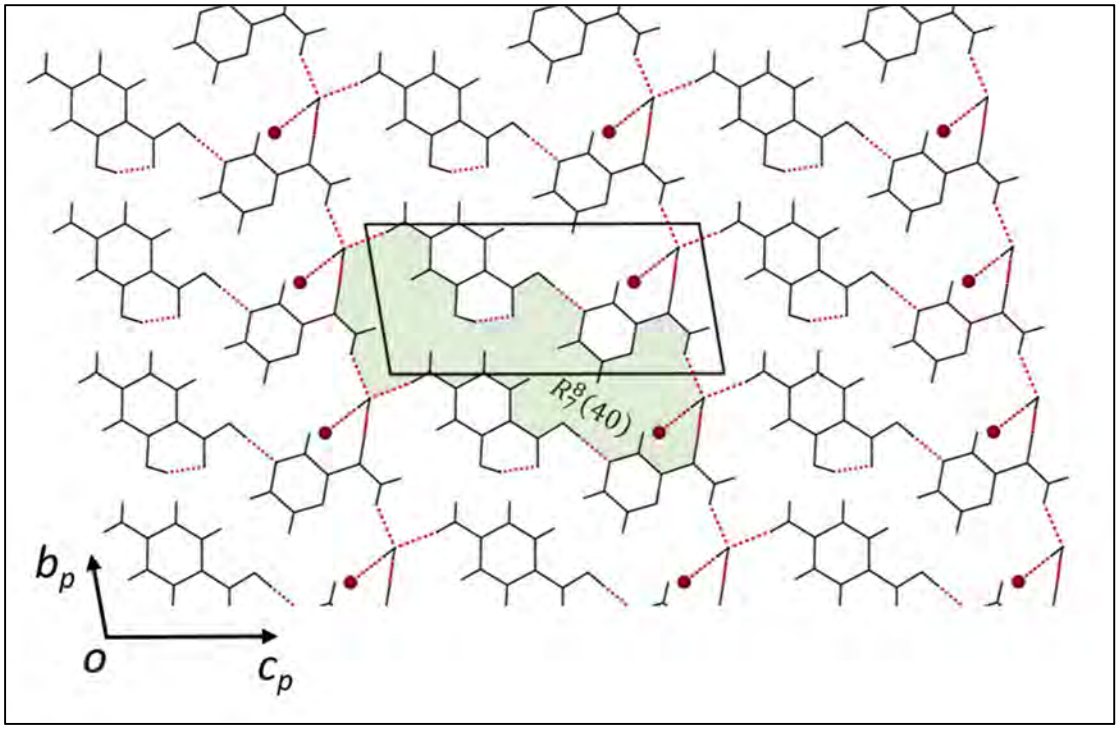

Figure 18: Hydrogen bonding scheme in the PAS-PYR·H_2O crystal viewed down the *a* axis.

When the layers are viewed down the *b* axis, it is clear that the single layer shown in **Figure 19** is hydrogen bonded to the layer below *via* the water molecule. The double layers are parallel to the *c* axis and are stacked along the *a*-direction. The layers show two hydrogen bonding ring motifs; the small ring (yellow shaded region) consists of 16 atoms, four H-bond donor atoms and four H-bond acceptor atoms and involves two water molecules and two PAS molecules. The motif shows that the water molecules act as a hydrogen bond donor to the hydroxyl group of PAS and simultaneously accepts a hydrogen bond from the amine moiety of PAS. The larger (orange shaded region) ring motif is made up of 32 atoms, eight H-bond donor atoms, eight H-bond acceptor atoms involving two water molecules, two PAS molecules and two PYR molecules. All hydrogen bonds are reported in **Table 9.**

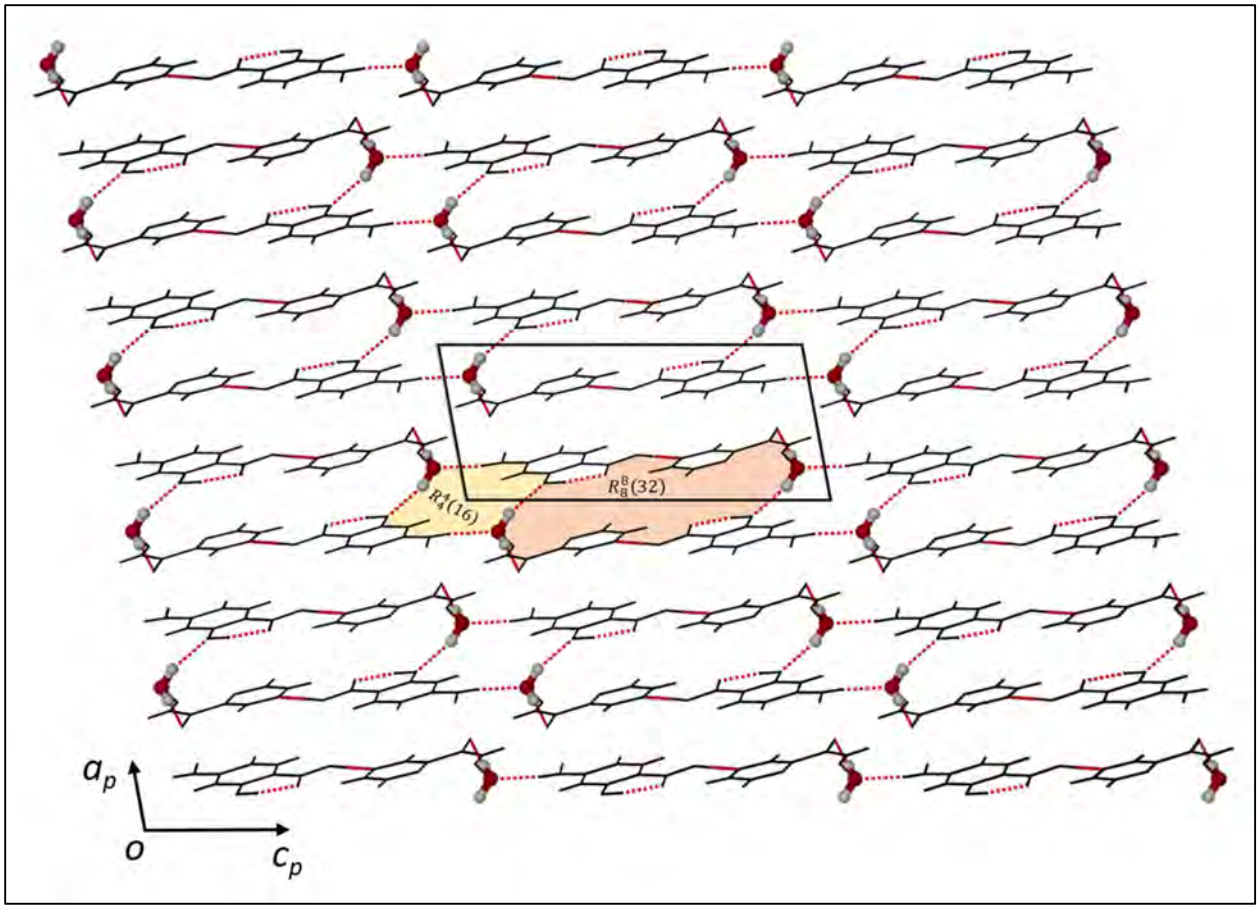

Figure 19: Propagation of hydrogen bonds between the layers of PAS-PYR·H_2O viewed down the *b* axis.

Table 9: Hydrogen bond parameters for PAS-PYR·H_2O.

D-H···A	D-H (Å)	H···A (Å)	D···A (Å)	D-H···A (°)	Symmetry code
O1W-H1W···O31	0.87(3)	2.02(3)	2.8480(17)	159(3)	-x,-y,1-z
O1W-H2W···O12	0.87(3)	1.97(3)	2.8372(18)	175(3)	x,-1+y,z
N11-H11A···O12	0.88(2)	2.24(2)	3.0315(18)	150.4(18)	1-x,2-y,1-z
N11-H11B···O1W	0.91(2)	2.06(2)	2.9574(19)	170.7(18)	x,1+y,-1+z
O31-H21···O11	0.92(3)	1.70(3)	2.5531(16)	154(3)	.
N32-H32A···O1W	0.92(2)	2.13(2)	2.9156(19)	143.5(18)	.
N31-H32B···O12	0.91(2)	2.03(2)	2.9341(17)	171.6(18)	1-x,1-y,2-z
O21-H71···N12	0.93(3)	1.78(3)	2.7076(17)	179(4)	.
C32-H32···O11	0.9500	2.5200	3.1727(18)	126.00	.

3.2.3. PAS-PCBA salt decomposition product

This complex has not previously been reported and in this study, attempts were made to synthesize it *via* neat and LAG methods as described in Chapter 2 of this work. The material was prepared by grinding equimolar amounts of PAS (0.65 mmol, 100 mg) and PCBA (0.65 mmol, 81mg) using a mechanical ball mill. LAG samples were prepared by adding 3 drops (~15 µL) of solvent before grinding. Neat grinding was carried out solvent free. The identity of the material as a salt was confirmed by SCXRD analysis. However, the PAS had decomposed through loss of CO_2.[2]

3.2.3.1. Characterization

3.2.3.1. A) ATR-FTIR spectra for the PAS-PCBA multicomponent materials and bulk crystalline material

Shown in **Figure 20** are the FTIR spectra for pure PAS, PCBA, NG, LAG and bulk crystalline samples. PCBA is characterized by a broad OH stretch between 2609-2181 cm^{-1} and a carbonyl stretch at 1715 cm^{-1}. For all samples, the amine bands and both carbonyls of PAS and PCBA are maintained even though there are small shifts in the peak positions. Both the NG and LAG samples show evidence of both starting materials; however, the characteristics of PAS are more prominent than those of PCBA and is probably a result of the presence of unreacted starting material. The broad OH stretch of PCBA only shows in the bulk crystalline material and does not show in the NG and LAG samples. A summarized list of peak shifts is reported in **Table 10**. The bulk crystalline sample exhibits characteristic modes for both PAS and PCBA.

Table 10: Summary of the spectral band shifts in the PAS-PCBA complex.

Vibrational mode	PAS/cm^{-1}	PCBA/cm^{-1}	Neat/cm^{-1}	H_2O/cm^{-1}	MeOH/cm^{-1}	EtOAc/cm^{-1}	MeCN/cm^{-1}	SC*/cm^{-1}
νNH_2	3494, 3387	-	3494, 3387	3494, 3388	3494, 3387	3494, 3386	3494, 3388	3494, 3385
$\nu C=O$	-	1705	1715	1715	1715	1716	1716	1713
$\nu C=O$	1613	-	1614	1612	1614	1612	1615	1615

SC*=Crystalline material

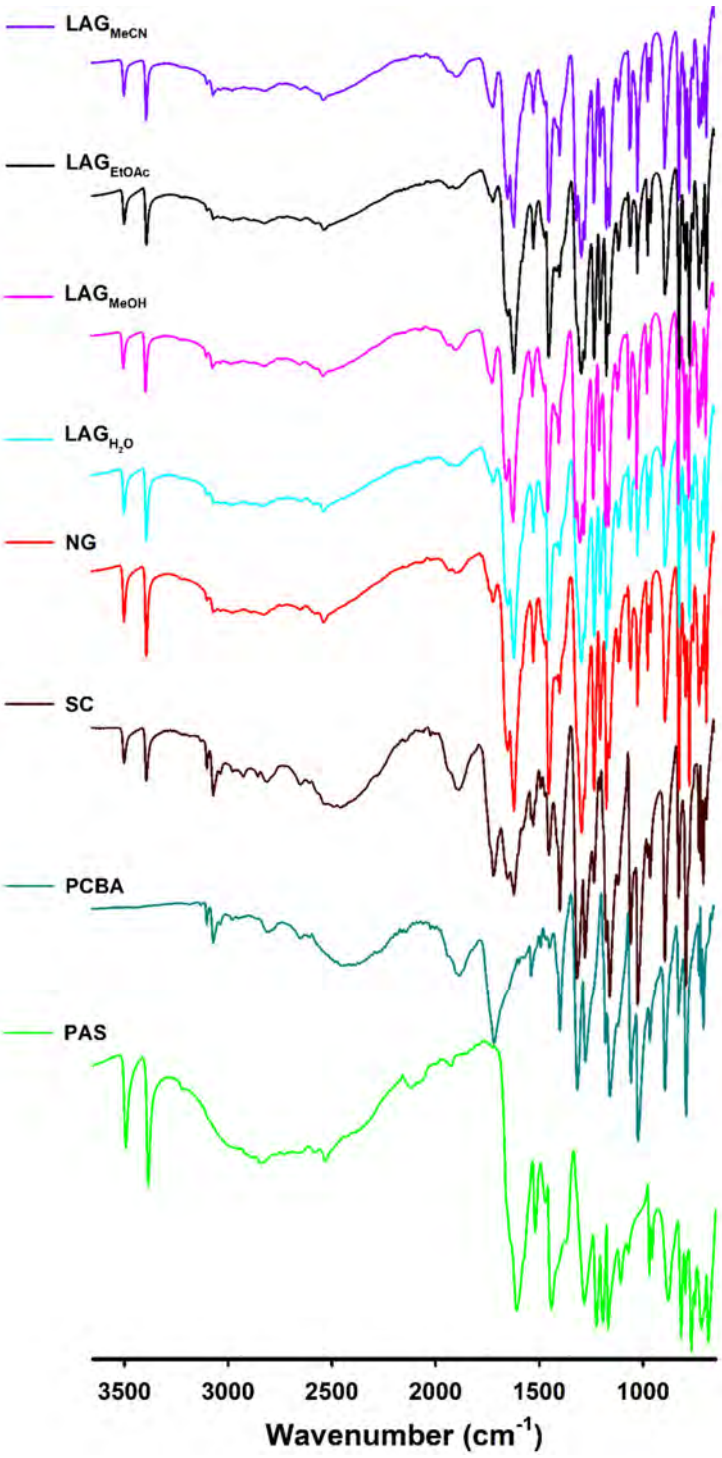

Figure 20: ATR-FTIR spectra for PAS, PCBA, NG, LAG_{H2O}, LAG_{MeOH}, LAG_{EtOAc}, LAG_{MeCN} and the bulk crystalline samples.

3.2.3.1. B) PXRD patterns of PAS-PCBA

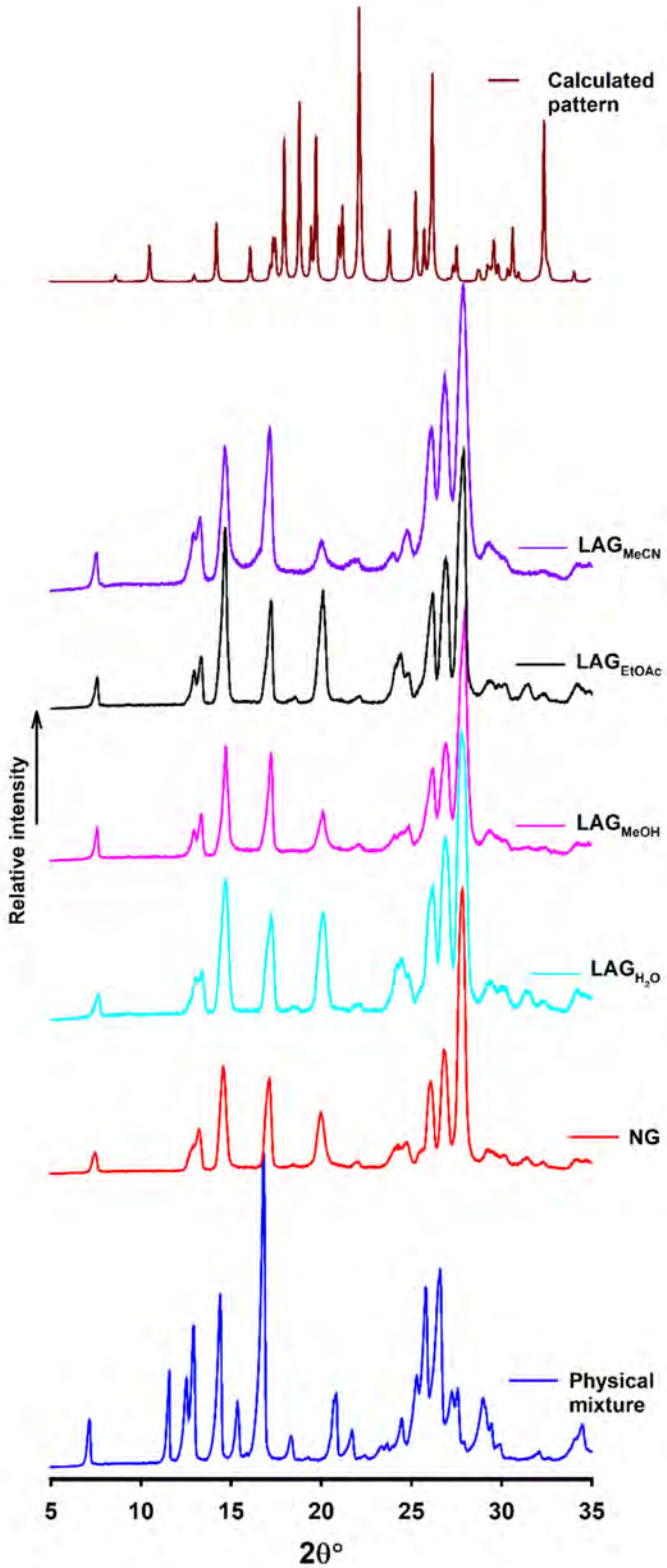

Figure 21: PXRD patterns for the physical mixture, NG, LAG_{H2O}, LAG_{MeOH}, LAG_{EtOAc}, LAG_{MeCN} and the calculated pattern.

The PXRD patterns of the ground samples and the physical mixture are presented in **Figure 21**. The PXRD instrument broke down and the analysis of the crystalline sample could not be carried out. The calculated PXRD pattern has been included with those of the ground samples. The patterns for the ground samples are similar to each other but differ from the physical mixture indicating the presence of a different phase. The major differences are related to the disappearance of peaks at 11º and 15º (2θ). However, there are several peaks present in all the PXRDs of the ground samples. Some of these peaks are located at 7, 12, 14, and 25º 2θ. This supports the FTIR data suggesting the presence of unreacted material. The calculated PXRD pattern is different from the ground samples even though there are some peaks that match.

3.2.3.1. C) Thermal analysis of PAS-PCBA multicomponent materials

DSC thermograms of PAS and PCBA show melt endotherms between 133.9-140.7 °C for PAS and 226.7-226.8 °C for PCBA. The NG exhibits two distinct endotherms at 150.6-156.2 °C and 168.7-174.6 °C which occur between melting points of both starting materials, depicted in **Figure 22 (A)**. Two distinct endotherms are present in all the LAG samples and occur at approximately the same temperature as those in the NG sample (**Figure 22 (B)**). The first set of endotherms occur at 148.3-157.3 °C and is immediately followed by a recrystallisation exotherm in the range 155-160 °C and upon further heating, a second endotherm occurs between 166.2-174.8 °C. All temperatures at which the thermal events (first and second endotherms and recrystallisation temperatures) occur are presented in **Table 11**. All samples were temperature cycled, *i.e.*, heating to a temperature slightly beyond the exotherm and followed by cooling to room temperature and reheating the sample. After the second cycle, the first endotherm disappears in all samples and only the second endotherm remains, as shown in **Figure 23 (A)**.

Table 11: Melt onset, recrystallisation point and peak temperatures of PAS-PCBA cocrystal.

Samples	First endotherm		Exotherm	Second endotherm	
	T_{onset} (°C)	T_{peak} (°C)	T_{peak} (°C)	T_{onset} (°C)	T_{peak} (°C)
NG	150.6	156.2	158.6	168.7	174.6
LAG_{H2O}	146.0	151.5	156.2	166.2	173.3
LAG_{MeOH}	148.9	155.1	158.2	167.9	173.9
LAG_{MeCN}	148.3	155.8	157.9	169.3	174.6
LAG_{EtOAc}	152.5	157.3	159.7	168.8	174.8
SC*	-	-	-	173.5	178.2

*T_{onset} = the start of melting.
*T_{peak} = trough of the endotherm.

The second endotherm may be the decomposition product since the overlay of the DSC and its corresponding TGA thermogram shows a weight loss of 17.4% at 166.9 °C matching with the second endotherm, **Figure 23 (B)**. A weight loss of 15.9% is expected for the loss of CO_2 in a (1:1) mixture of PAS and PCBA. It was determine that the loss was due to CO_2 from the crystal structure (elucidated later). The DSC thermogram of the bulk crystalline material shows a single melt endotherm at 173.5-

178.2 °C, which is close to the melting point range of the second endotherm of the ground samples. DSC and TGA overlays for all samples show similar profiles. The differences seen in the PXRD diffractograms between the calculated pattern and the ground samples could be a result of the different phases that exist. Apart from a small amount of H_2O present in the LAG_{H2O} there is no evidence for included solvent in the samples as illustrated in **Figure 24**.

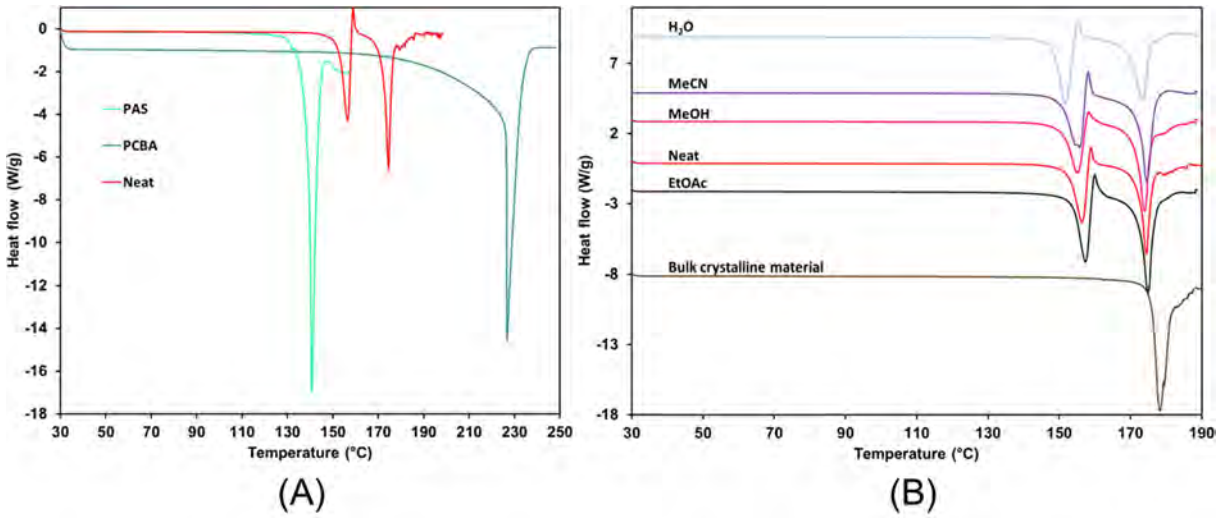

Figure 22: (A) DSC thermograms of PAS, PCBA and NG. (B)shows the stacked DSC thermograms for the NG, LAG_{H2O}, LAG_{MeOH}, LAG_{EtOAc}, LAG_{MeCN} and the bulk crystalline material.

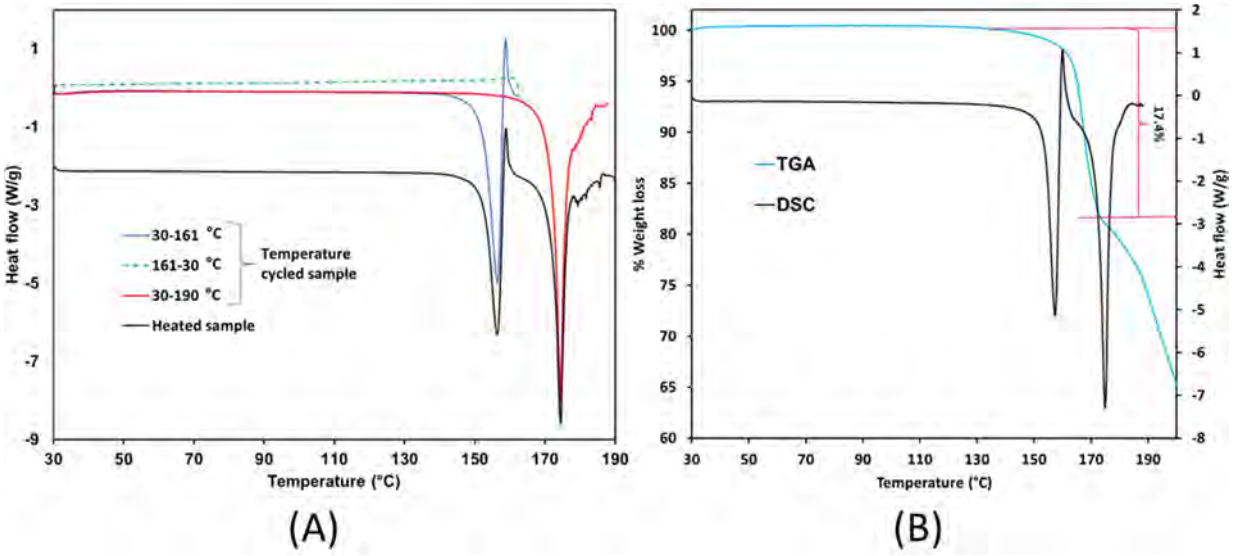

Figure 23: (A) Stacked DSC thermograms showing the temperature cycled NG sample. (B) is the superimposed DSC and TGA thermograms of LAG_{EtOAc} showing the melt and decomposition of the product.

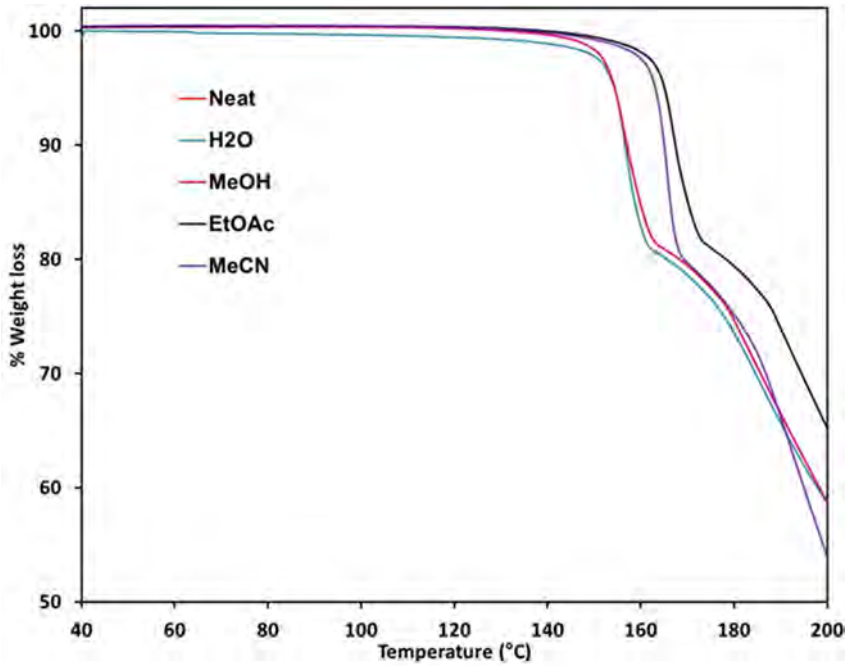

Figure 24: TGA thermograms for the NG, LAG_{H2O}, LAG_{MeOH}, LAG_{EtOAc} and LAG_{MeCN} showing initial decomposition due to loss of CO_2 followed overall decomposition.

3.2.3.1. D) Single-crystal analysis of the PAS-PCBA multicomponent material

The crystals were prepared by dissolving equimolar amounts of PAS (0.65 mmol, 10 mg) and PCBA (0.65 mmol, 8.1 mg) in approximately 7 mL MeOH and the solution was stirred at room temperature until all components had fully dissolved. It was left to evaporate slowly under ambient conditions. Crystal growth was also achieved by melt recrystallisation of the neat ground sample by heating 2.0 mg of the NG sample to 161 ºC at 5 ºC/min and slowly cooling it to 30 ºC at 1 ºC/min in the DSC instrument (TA DSC 250). This led to production of a cluster of crystals from which one of suitable quality was selected for single-crystal analysis. The crystals grown from both slow evaporation and melt crystallisation resulted in a multicomponent decomposition product consisting of aminophenol-pyrazine carboxylate, shown in **Figure 25**. The unit cell parameters are shown in **Table 12**. It is evident from the image in **Figure 25** that the carboxylic acid moiety of PAS is no longer part of the structure.

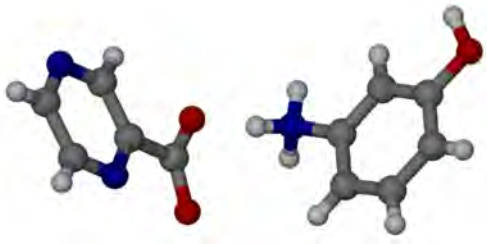

Figure 25: Molecular structure of the decomposition product of the PAS-PCBA salt.

Table 12: Unit cell parameters for PAS-PCBA decomposition product.

Formula	$C_{11}H_{11}N_3O_3$
Space group	$P2_1/c$
a/Å	8.4018(3)
b/Å	6.5102(2)
c/Å	20.4430(8)
α/°	90
β/°	95.437(1)
γ/°	90
Z	4
V/Å^3	1113.15

The multicomponent product shows proton transfer from the carboxylic acid moiety of PCBA to the amine of PAS resulting in a negatively charged carboxylate moiety and positively charged amine. The identity of the product as a cocrystal, salt or physical mixture before decomposition cannot be verified and therefore further investigations are needed.

3.3. Summary

From the attempts made at preparing the cocrystals of PAS with different coformers, two previously reported cocrystals (PAS-INH and PAS-PYR·H_2O) were isolated and characterised using bulk characterisation techniques and SCXRD. The PAS-PCBA preparation led to a decomposition product that was also characterised. The PAS-INH cocrystal was prepared using both slow evaporation and mechanochemical synthesis while the PAS-PYR·H_2O cocrystal was prepared by slow evaporation. Preparation of the cocrystal by mechanochemistry was unsuccessful in all cases except for the LAG_{H_2O} experiments. Single crystals of the decomposition product were isolated using melt recrystallisation in the DSC and led to partial SCXRD characterisation of the decomposition structure.

References

(1) Drozd K. V., Manin A. N., Churakov A. V. and Perlovich G. L. Drug-Drug Cocrystals of Antituberculous 4-Aminosalicylic Acid: Screening, Crystal Structures, Thermochemical and Solubility Studies. *Eur. J. Pharm. Sci.* **2017**, *99*, 228–239.

(2) Jivani, S. G. and Stella V. J. Mechanism of Decarboxylation of P-Aminosalicylic Acid. *J. Pharm. Sci.* **1985**, *74*, 1274–1282.

(3) Kornblum S. S. and Sciarrone B. J. Decarboxylation of P-Aminosalicylic Acid in the Solid State. *J. Pharm. Sci.* **1964**, *53*, 935–941.

(4) Salem A., Khanfar E., Nagy S. and Széchenyi A. Cocrystals of Tuberculosis Antibiotics: Challenges and Missed Opportunities. *Int. J. Pharm.* **2022**, *623*, 121924.

(5) Snider D. E. Pyridoxine Supplementation during Isoniazid Therapy. *Tubercle* **1980**, *61*, 191–196.

(6) Doleal M., Zitko J. and Jamplek J. Pyrazinecarboxylic Acid Derivatives with Antimycobacterial Activity. In *Understanding Tuberculosis - New Approaches to Fighting Against Drug Resistance*; Cardona, P.-J., Ed.; InTech, **2012**.

(7) Grobelny P., Mukherjee A. and Desiraju G. R. Drug-Drug Co-Crystals: Temperature-Dependent Proton Mobility in the Molecular Complex of Isoniazid with 4-Aminosalicylic Acid. *CrystEngComm.* **2011**, *13*, 4358.

(8) Sheldrick G. M. *SHELXT* – Integrated Space-Group and Crystal-Structure Determination. *Acta Cryst.* **2015**, *A71*, 3–8.

(9) Sheldrick G. M. Crystal Structure Refinement with *SHELXL*. *Acta Cryst.* **2015**, *C71*, 3–8.

(10) Ferrence G. M., Tovee C. A., Holgate S. J. W., Johnson N. T., Lightfoot M. P., Nowakowska-Orzechowska K. L. and Ward S. C. *CSD Communications* of the Cambridge Structural Database. *IUCrJ* **2023**, *10*, 6–15.

(11) Zhang Z., Fang J., Bo Y., Xue J., Liu J., Hong Z. and Du Y. Terahertz and Raman Spectroscopic Investigation of Anti-Tuberculosis Drug-Drug Cocrystallization Involving 4-Aminosalicylic Acid and Pyrazinamide. *J. Mol. Struct.* **2021**, *1227*, 129547.

Chapter 4: Pyridoxine salts

4.1. Introduction

As previously mentioned, pyrazinecarboxylic acid (PCBA) is the active form of pyrazinamide, a compound that exhibits antimycobacterial activity, making it a suitable candidate for cocrystallization with other active pharmaceutical ingredients (API).[1] Pyridoxine (PN) is one of the three main forms of group B vitamins, the other two derivatives being pyridoxal and pyridoxamine.[2] These are naturally occurring vitamins found in food which play a vital role as coenzymes in the synthesis of neurotransmitters and contribute to the maintenance of a healthy nervous system.[3] Cocrystallization experiments in which pyridoxine and different coformers (*i.e.* isoniazid, squaric acid, nicotinic acid, saccharin, para-aminobenzoic acid, para-nitrobenzoic acid) lead to the formation of different types of multicomponent structures including cocrystals, salts and eutectics, all of which result in improved physicochemical properties in most cases, have been reported.[4,5] Pyridoxine is administered as a food supplement during TB therapy, therefore, co-crystallizing the compound with an API serves as a possible alternative method to reducing the so called "pill burden" when combination therapy is advocated.

4.2. Present study

Two salts, pyridoxine-4-aminosalicylate monohydrate (PN-PAS·H_2O) and pyridoxine-pyrazinecarboxylate (PN-PCBA) were identified and analysed using several analytical techniques. Pyridoxine and the coformers were ground together in 1: 1 molar ratios using neat grinding and LAG as described (Chapter 2) and the products screened using PXRD. New phases were further characterised using FTIR, TGA and DSC. Crystallisation experiments of the new phases were setup using slow evaporation in order to obtain single crystals. Once obtained, suitable single crystals were analysed through SCXRD as described in Chapter 2.3.4. Presented in **Figure 1** are the molecular diagrams of the compounds investigated and **Table 1** provides a summary of the salts covered in this chapter.

Table 1: Summary of synthesized compounds in this chapter and the next.

Compound	Nature	Synthesis methods			Reported
		Neat	LAG	Solvent recrystallization	
PN-PCBA	Salt	✓	MeOH, H_2O, MeCN and EtOAc	MeCN + MeOH (3:1)	This work
PN-PAS	Salt (hydrate)	✓	MeOH, H_2O, MeCN and EtOAc	EtOAc + MeOH (3:1)	This work

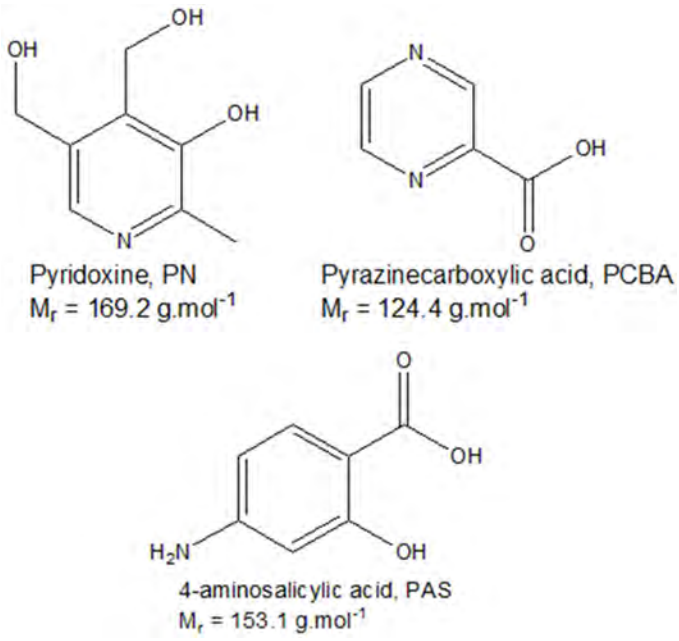

Figure 1: Molecular structures and acronyms of compounds investigated in this chapter.

4.2.1. Pyridoxine-4-aminosalicylate monohydrate salt

The salt was prepared by grinding equimolar amounts of PN (0.97 mmol, 111 mg) and PAS (0.97 mmol, 104mg). The LAG samples were prepared by addition of 3 drops (~15 μL) of solvent (H_2O, MeCN, EtOAc and MeOH, respectively) to the PN and PAS mixture prior to grinding in the mechanical ball mill. The neat grind involved no addition of solvent.

4.2.1.1. Characterization

4.2.1.1. A) ATR-FTIR spectra of the PN-PAS ground samples and bulk crystalline material.

Depicted in **Figure 2** are the FTIR spectra of the ground samples and bulk crystalline material (SC) in comparison to the starting materials (PAS and PN). PAS is characterized by two amine bands at 3494 and 3387 cm^{-1}, a carbonyl C=O stretch at 1615 cm^{-1} and a broad OH band between 3095-2452 cm^{-1}, while PN is characterized by a hydroxyl absorption peak at 3278 cm^{-1} and a C-O band at 1019 cm^{-1}. The amine bands from PAS were maintained in the bulk crystalline material and ground samples but shifted in peak position. These appear as shoulders alongside the newly formed N-H bond of PN which is a result of proton transfer from the carboxylic acid moiety of PAS to the nitrogen atom in the aromatic ring of PN. The broad OH stretch of the carboxylic acid moiety of PAS disappears due to proton transfer to PN. This is reinforced by shifts in the peak positions of the carbonyl (C=O and C-O) bands of PAS to higher wavenumbers. The hydroxyl and C-O bands of PN are maintained in all samples but at different peak positions owing to hydrogen bond formation between the PAS and PN molecules. A new broad peak appears between 2200 and 2800 cm^{-1} and is present in all grinds as well as the bulk crystalline material

which is indicative of strong hydrogen bonding interactions. **Table 2** summarises the shifts in wavenumbers of pertinent functional groups.

Table 2: Common stretching/bending frequencies for the putative salt obtained from the different preparations.

Vibrational Modes	PAS/cm^{-1}	PN/cm^{-1}	Neat/cm^{-1}	MeCN/cm^{-1}	EtOAc/cm^{-1}	MeOH/cm^{-1}	H_2O/cm^{-1}	SC*/cm^{-1}
vOH		3278	3237	3238	3237	3235	3334	3234
vNH_2	3494, 3387		3472, 3357	3472, 3356	3470, 3354	3472, 3358	3462, 3358	3499,3391
vC=O	1615	-	1622	1639	1640	1638	1625	1638
vC-O	1286	-	1289	1289	1289	1293	1253	1286
vC-OH	-	1019	1026	1027	1027	1028	1020	1025

SC* = bulk crystalline material.

The splitting of the peaks in the amine region of the FTIR spectra is probably owing to the presence of unreacted material in the ground material as this effect is not seen in the SC sample.

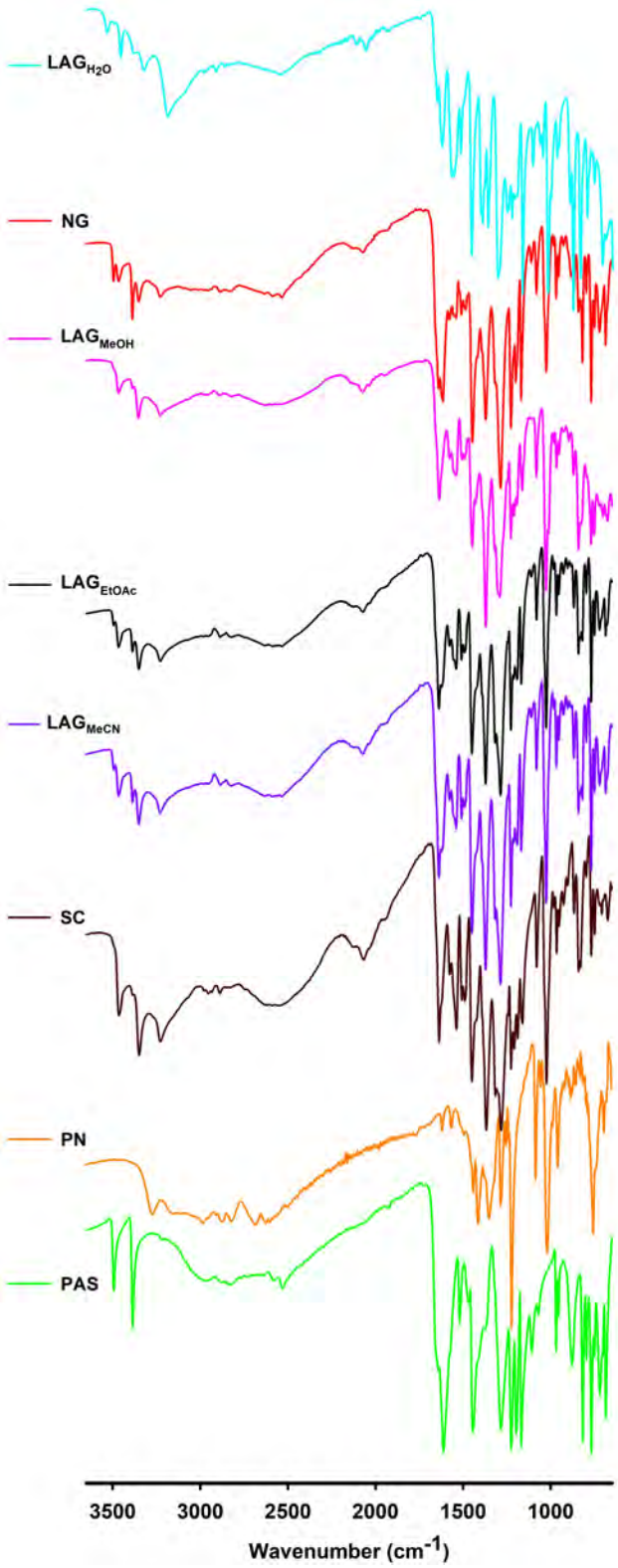

Figure 2: Stacked ATR-FTIR spectra for PN, PAS, the bulk crystalline material, $LAG_{MeCN,}$ LAG_{EtOAc}, LAG_{MeOH}, NG and LAG_{H2O} samples.

4.2.1.1. B) Powder patterns of the PN-PAS ground samples and bulk crystalline material

PXRD of the ground samples were carried out in order to confirm phase purity and to determine if different phases were obtained after neat and liquid assisted grinding. The crystalline material obtained from slow evaporation was gently ground to a fine powder in a mortar and pestle prior to data collection. From **Figure 3**, the NG and LAG_{MeCN} grinds have similar features to the physical mixture and possibly indicates the presence of unreacted material. The diffractograms for the LAG_{MeOH} and LAG_{EtOAc} grinds are similar to each other and closely match the diffractogram of the bulk crystalline material. Generally, all samples differ from the physical mixture but it seems the LAG_{H2O} has more unreacted material.

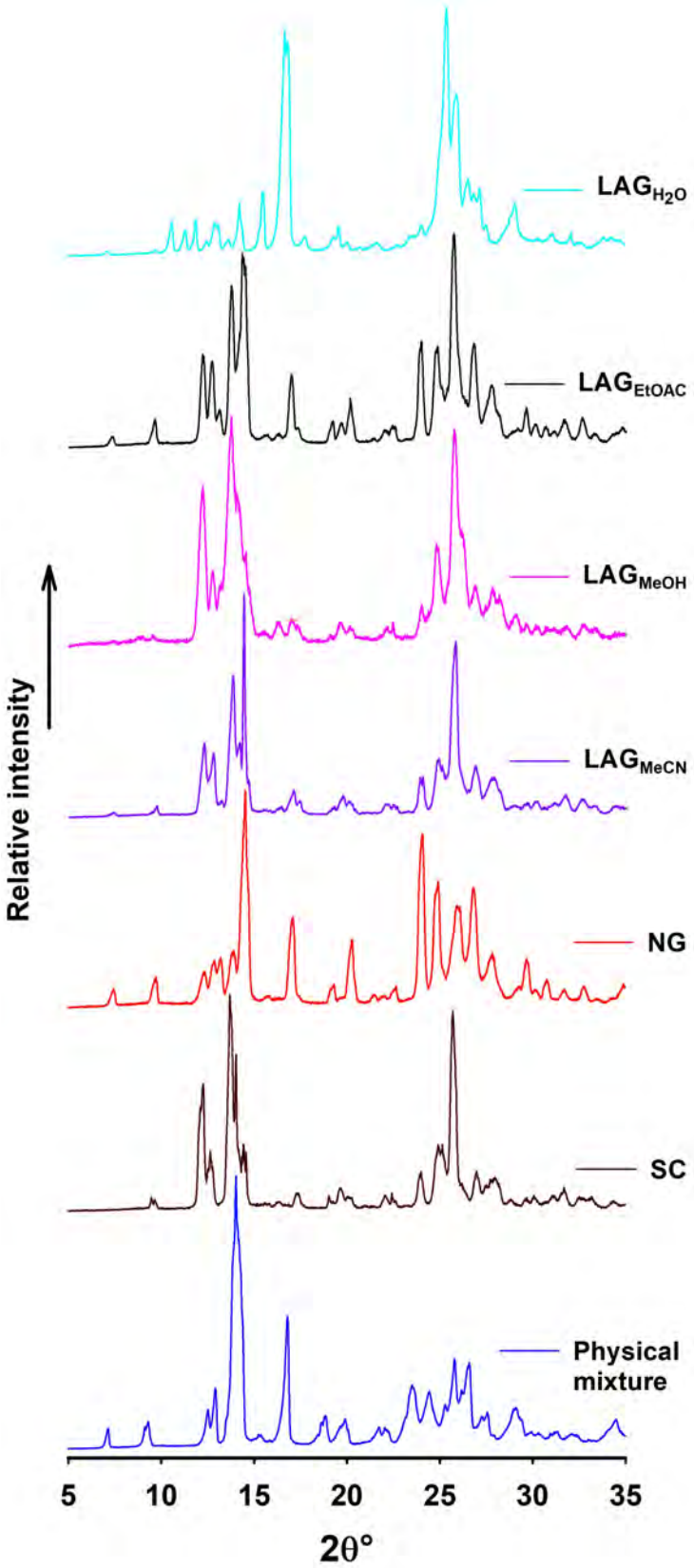

Figure 3: PXRD patterns for the PN and PAS, the bulk crystalline material, $LAG_{MeCN,}$ LAG_{EtOAc}, LAG_{MeOH}, NG and LAG_{H2O} samples.

Figure 4 shows the PXRD pattern calculated from single crystal data and the experimental measurement. There is a near one-to-one correspondence between the two diffractograms indicating that the bulk crystalline material is consistent with the single crystal. Moreover, these diffractograms match those of the ground samples in which MeOH, MeCN and EtOAc were used indicating that both synthetic routes lead to formation of the same crystal form.

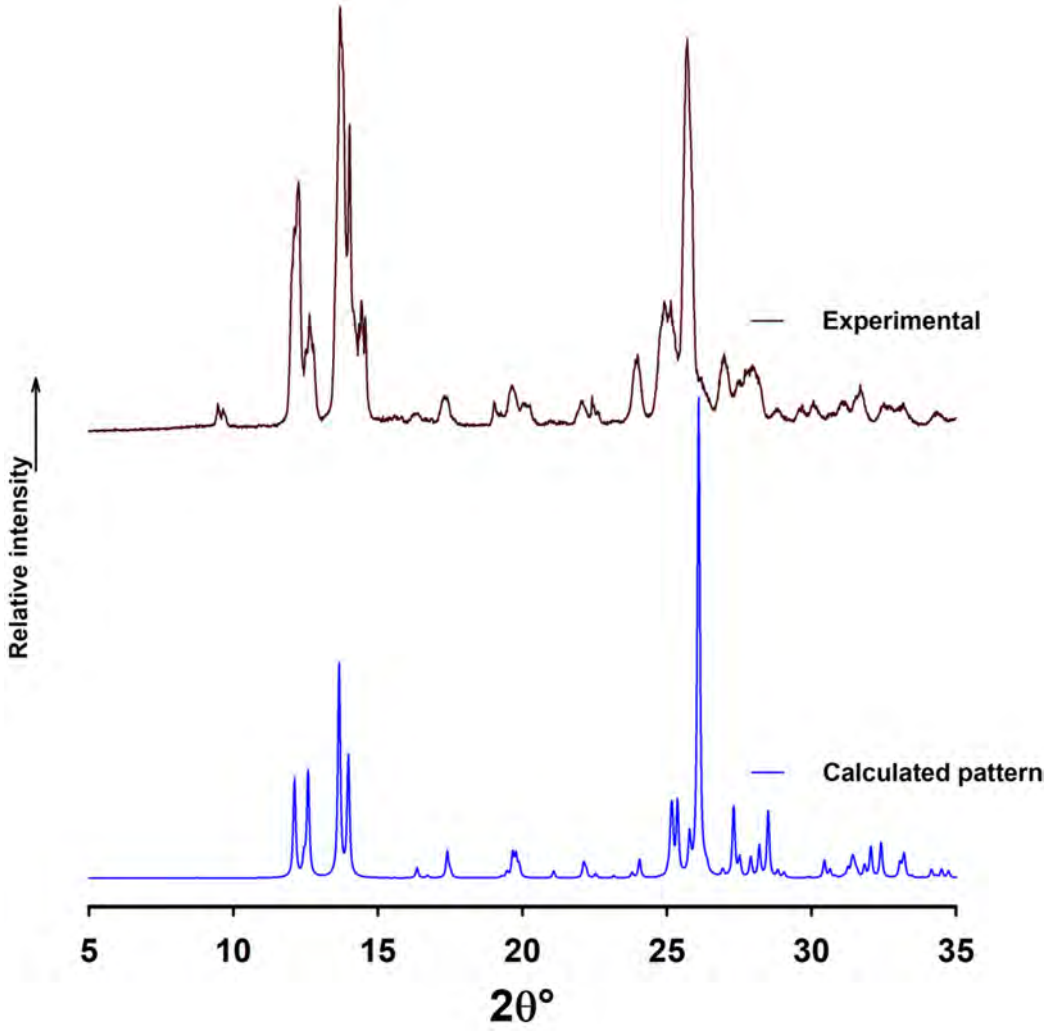

Figure 4: Experimental and calculated powder patterns for PN-PAS·H_2O crystals.

4.2.1.1. C) Thermal analysis of the PN-PAS ground samples and bulk crystalline material

DSC thermograms for the API, PN and PAS, show melting endotherms in the range of 153.1-158.5 °C for PN and 133.9-140.7 °C for PAS. The NG sample melts between 112.3-120.8 °C which is below the melting point ranges of both starting materials (**Figure 5 (A)**). The LAG samples have similar melting point ranges to the NG (113-122 °C), see **Figure 5 (B)**. The melt endotherms are followed by the onset of decomposition. The LAG_{H2O} sample shows solvent loss in the range 64.9-89.5 °C, followed by decomposition. This is also reflected in the TGA thermogram (**Figure 6 (A)**) which shows that the water

loss occurs between 60-90 °C followed by the onset of decomposition. All the DSC thermograms have broad endotherms in the range 50-90 °C indicating small quantities of included solvent. This is supported by TGA thermograms shown in **Figure 6 (B)**. It also shows the minor weight loss for each of the LAG samples between 45-80 °C. Further characterisation (*e.g.,* hyphenated evolved gas analysis FTIR-TGA) is required to definitively confirm the identity of the included solvent for the LAG samples. **Table 3** summarises the melt onset and peak temperatures of the NG, LAG samples and bulk crystalline material.

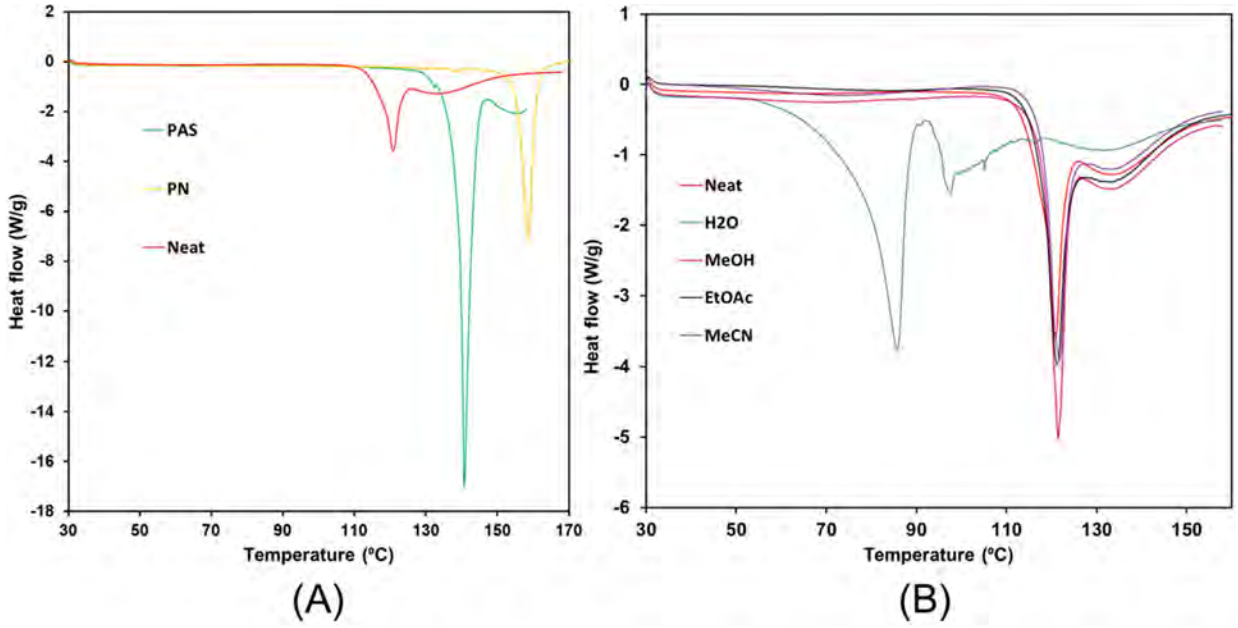

Figure 5: (A) DSC showing endotherms for PAS, PN and NG. (B) shows DSC thermograms for NG and the LAGs.

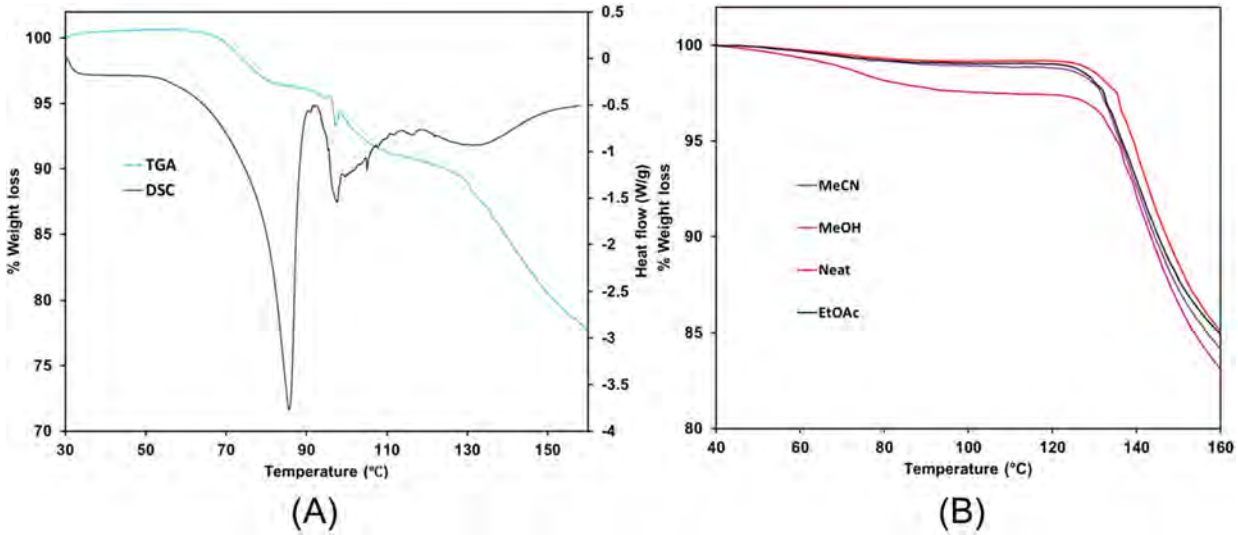

Figure 6: (A) Superimposed DSC and TGA thermograms of the LAG_{H2O} sample. (B) Overlaid TGA thermograms for the NG, LAG_{MeCN}, LAG_{EtOAc} and LAG_{MeOH}.

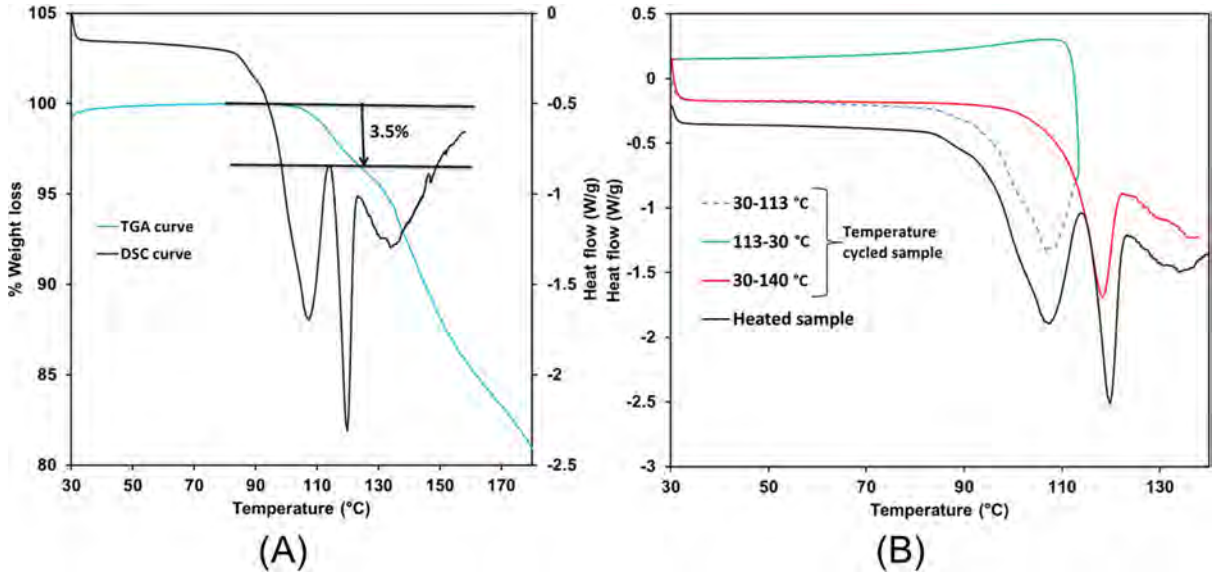

Figure 7: (A) Superimposed TGA (blue) and DSC (black) thermograms of PN-PAS·H_2O crystals. (B) DSC curve of PN-PAS·H2O reheated.

Figure 7 (A) depicts a DSC thermogram for the recrystallized sample grown *via* slow evaporation from a 3:1 (v/v) solvent mixture of EtOAc and MeOH. The first endotherm in the range 86-114 °C results from water loss. This is followed by the melt of the **PN-PAS·H_2O salt** in the range 113-123 °C after which decomposition ensues. The TGA thermogram reflects a weight loss of approximately 3.5% commencing at 93 °C and continuing to 114 °C. This weight loss correlates well with the 3.15% for a water molecule with partial site occupancy determined from the crystal structure. The compound then undergoes gradual decomposition. The DSC thermogram in **Figure 7 (B)** supports water loss since cooling and reheating the sample after the first endotherm leads to the disappearance of the first endotherm with only the melt endotherm remaining.

Table 3: Melt onset and peak temperatures of the ground samples and bulk crystalline material.

Samples	T_{onset} (°C)	T_{peak} (°C)
NG	112.3	120.8
LAG_{H2O}	-	-
LAG_{MeOH}	115.8	121.6
LAG_{MeCN}	115.2	121.9
LAG_{EtOAc}	113.3	121.0
SC	106.6	120.0

The melting point range of the bulk crystalline material is similar to the LAG samples (EtOAc, MeOH, and MeCN) and NG, indicating that the formation of the salt is independent of the synthetic approach.

4.2.1.1. D) Single crystal X-ray analysis of the PN-PAS ground samples and bulk crystalline material

Single crystals were prepared by dissolving equimolar amounts of PAS (0.065 mmol, 10.43 mg) and PN (0.065 mmol, 11.44 mg) in a solvent mixture of MeOH and EtOAc (1:3 v/v) while gently heating the solution to approximately 45 °C to facilitate complete dissolution of the components. The solution was left to evaporate slowly under ambient conditions. A crystal of suitable quality for single crystal X-ray diffraction was selected for data collection. Attempts to grow the crystals *via* sublimation failed as it led to the decomposition of the PAS component through the elimination of CO_2 from PAS.[6]

i. Data collection and space group determination

Unit cell parameters, crystal system, space group and single crystal data were collected on a Bruker D8 Venture diffractometer. The PN-PAS·H_2O salt crystallises in the space group $P2_1/c$.

ii. Structure solution and refinement

SHELXT was used for structure solution and SHELXL was utilized for refinement of PN-PAS·H_2O salt. All atoms were refined anisotropically based on well-behaved isotropic temperature factors and hydrogen atoms were placed in idealized positions in a riding model. Each hydrogen atom was assigned an isotropic temperature factor of 1.2 times (1.5 for methyl hydrogens) that of its parent atom.

Table 4: Data - collection and refinement parameters for PN-PAS·H_2O salt.

Data-collection and refinement parameters	
Formula unit	$(C_8H_{12}NO_3)$ $(C_7H_6NO_3)$ 0.63(H_2O)
Formula mass (g mol^{-1})	333.66
Crystal system	monoclinic
Space group	$P2_1/c$ (No. 14)
a/Å	7.2978(3)
b/Å	14.5994(6)
c/Å	14.4328(6)
α/°	90
β/°	103.142(2)
γ/°	90
Volume (Å^3)	1497.45(11)
Z	4
D_{calc} (g cm^{-3})	1.480
F (000)	705
μ (MoKα) (mm^{-1})	0.117
Crystal size (mm^3)	0.27 x 0.36 x 0.39
Temperature (K)	100
Range scanned θ (º)	2.0 - 35.8
Index ranges	-12: 10 ; -23: 23 ; -23: 23
Total number of reflections collected	100239
Number of unique reflections	6936
Number of reflections with I > 2σ (I)	5510
Number of least-squares parameters	270
R_{int}	0.049
S	1.04
R_1 (I > 2σ (I))	0.0401
wR_2	0.1193
Weighting scheme parameters	a = 0.0618, b = 0.3462
$(\Delta/\sigma)_{mean}$	0.00
Δρ excursions (e Å^{-3})	-0.30, 0.50

For heteroatoms, hydrogen atoms were refined using peaks observed from a difference Fourier map. To refine the disorder in the PN molecule, the respective peak heights in the difference map were used to determine the site occupancy; based on the sum of the heights. The water molecule site occupancy was based on proximity to the disordered aliphatic hydroxyl group (discussed later). **Table 4** lists the data collection and refinement parameters.

iii. Molecular structure

The asymmetric unit consists of one molecule of PAS, one molecule of PN and a single molecule of water with partial occupancy (0.63), see **Figure 8 (A)**. From the crystal structure it could be established that salt formation had occurred since a hydrogen atom covalently bonded to the nitrogen atom of the pyridine ring of PN could be modelled. This is supported by the individual bond lengths of the carboxylate moiety of PAS, shown in **Table 5.** The aliphatic hydroxyl group located at the 4-position on the pyridine ring of the PN molecule is disordered over two positions shown in blue and green in **Figure 8 (B)**, while the water molecule is shown in green. The site occupancy of the water molecule and green aliphatic hydroxyl group are refined to site occupancy of 0.63 (63%) while the blue aliphatic hydroxyl group has occupancy of 0.37 (37%). In all subsequent images, the disorder has been hidden for the purposes of clarity.

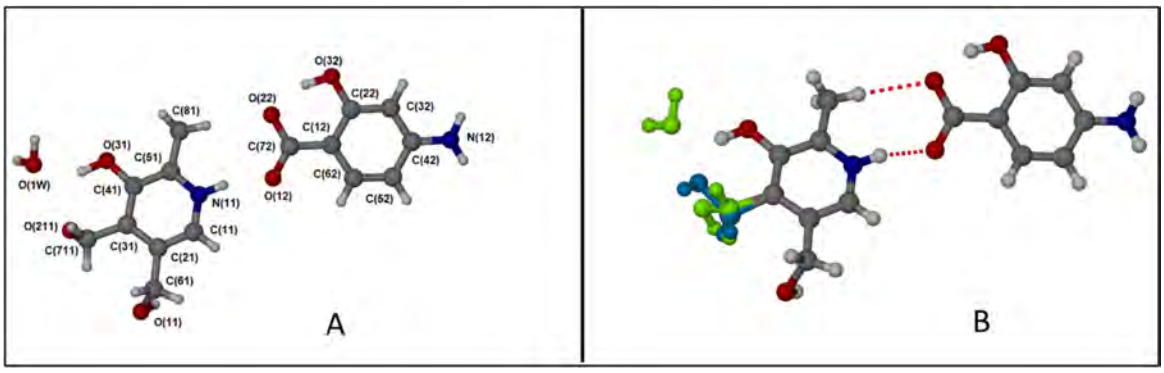

Figure 8: (A) The labelled molecular diagram of the asymmetric unit of PN-PAS·H_2O. (B) Shows hydrogen bonding between the PN and PAS molecule, it also shows the disorder of the aliphatic hydroxyl group and the H_2O molecule (the colours represent the corresponding site occupancies).

Table 5: Bond lengths of the carboxylate and pyridinium bonds in the PN-PAS salt compared to the selected structures in the CSD

PAS	This work	Carboxylic acid bonds	Refcode
	Carboxylate bonds		
C72-O22	1.2830(9)	1.317(2)	AMSALA02[7]
C72-O12	1.2660(9)	1.2517(19)	
PN	**Pyridinium bonds**	**Pyridine bonds**	
C51-N11	1.3457(10)	1.3327(3)	BITZAF[7]
C11-N11	1.3380(9)	1.3406(3)	

iv. Hydrogen bonding schemes

PN and PAS are hydrogen bonded to each other via a charge-assisted N-H···O hydrogen bond between the pyridine nitrogen atom N11of PN and the deprotonated oxygen atom O12 of the carboxylate moiety of PAS. The hydrogen bonding between the two molecules is supported by a weaker C-H···O hydrogen bond from the methyl group (C81) of PN to O22 of the carboxylate moiety of PAS (see **Figure 8 (B)**).

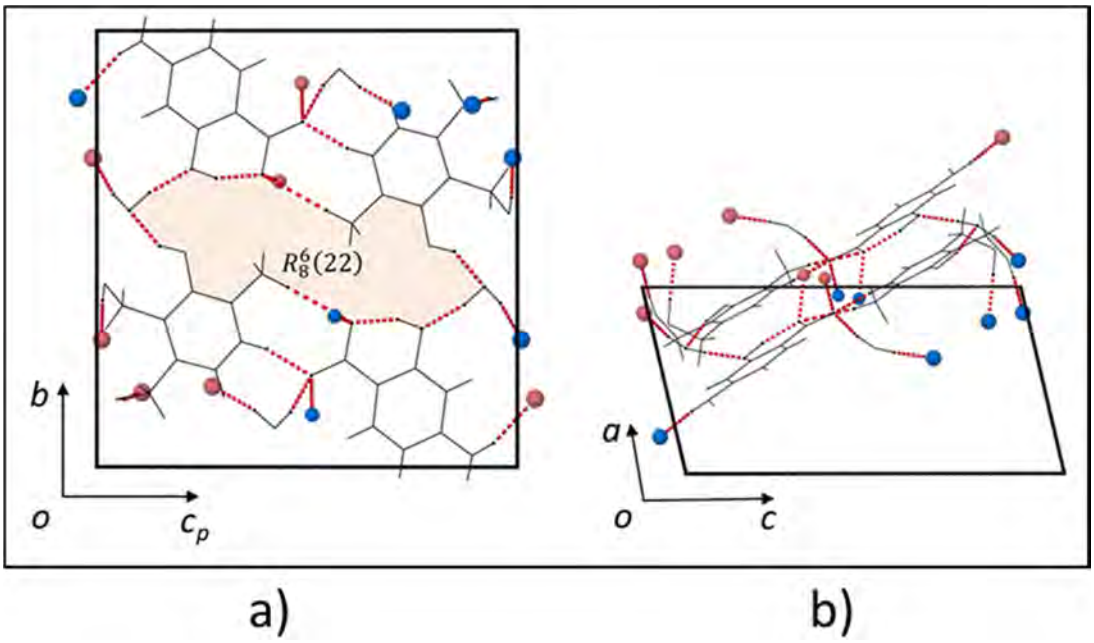

Figure 9: (a) Shows the hydrogen bonding ring motif ($R_8^6(22)$) of PN-PAS·H_2O viewed down the *a* axis. In the (b) image the red atoms indicate hydrogen-bonding above the plane while the blue atoms are below the plane.

Figure 9 (a) two PN-PAS moieties are hydrogen bonded to each other *via* two water molecules in the structure forming a ring motif. The motif involves eight H-bond donor atoms, six H-bond acceptor atoms and a total of 22 atoms that completes the ring motif. There are many hydrogen bond interactions in the structure some above the plane and some below. The out of plane hydrogen bonds are mainly through the aliphatic hydroxyl groups (O211 and O11). These are depicted in **Figure 9 (b**) as red and blue atoms. All the hydrogen bonds are provided in **Table 6** below. The COO^--$pyridine^+$-H bond length in this crystal falls within the average N^+-H···O^- H-bond length of 2.652(1).[7]

Table 6: Hydrogen bond parameters for PN-PAS·H_2O salt hydrate.

D-H···A	D-H (Å)	H···A (Å)	D···A (Å)	D-H···A (°)	Symmetry code
O1W-H1W···O32	0.970(12)	1.708(12)	2.6652(13)	168.6(10)	.
O1W-H2W···O12	0.972(19)	1.759(18)	2.7180(13)	168.2(15)	x,3/2-y,-1/2+z
N11-H11N···O12	0.918(15)	1.784(15)	2.6849(9)	166.4(14)	2-x,1-y,1-z
N12-H12A···O11	0.880(14)	2.143(14)	2.9982(9)	163.9(12)	1-x,1-y,-z
N12-H12B···O22	0.871(15)	2.399(15)	3.2250(10)	158.4(13)	1-x,1/2+y,1/2-z
O32-H22···O22	0.971(12)	1.606(10)	2.5230(9)	155.7(17)	.

D-H···A	D-H (Å)	H···A (Å)	D···A (Å)	D-H···A (°)	Symmetry code
O31-H41···O1W	0.969(10)	1.757(14)	2.6286(13)	147.9(14)	.
O31-H41···O211	0.969(10)	2.321(12)	2.8944(12)	117.1(12)	.
O31-H41···O212	0.969(10)	1.817(12)	2.6449(18)	141.5(15)	.
O11-H61···O22	0.968(6)	1.796(7)	2.7584(9)	172.3(16)	2-x,-1/2+y,1/2-z
O211-H711···O12	0.972(17)	1.888(17)	2.8547(13)	172.2(16)	2-x,-1/2+y,1/2-z
C711-H71A···O11	0.99	2.5	3.196(2)	127	.
C711-H71B···O1W	0.99	2.56	3.185(5)	121	1-x,1-y,-z
C81-H81B···O22	0.98	2.45	3.4267(9)	176	2-x,1-y,1-z

*The author is aware that the highlighted angle is smaller than the angular cutoff of 120° for a hydrogen bond. It is, however, still close enough to the cutoff.

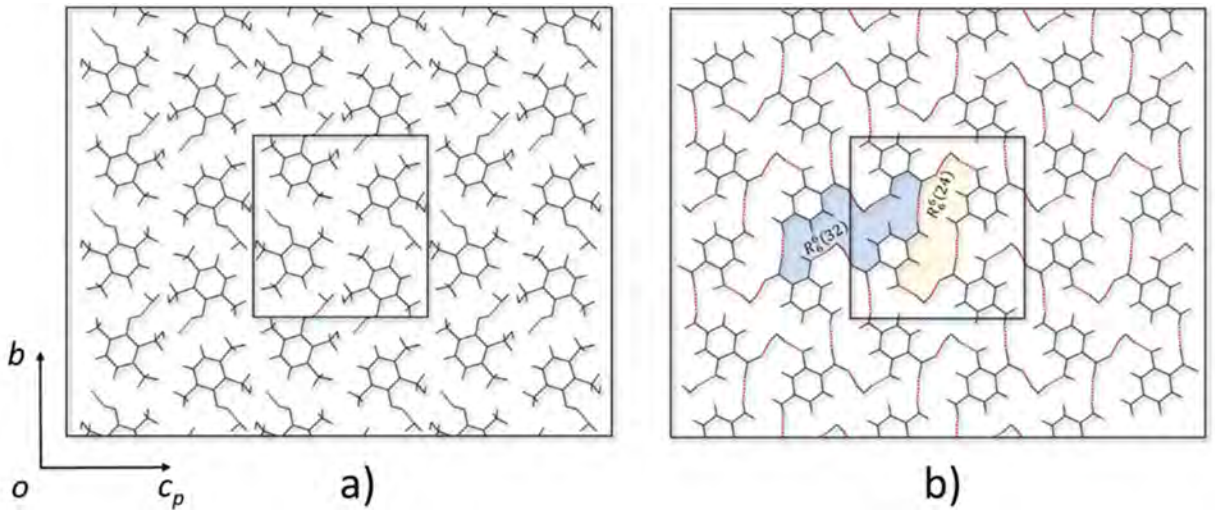

Figure 10: (a) hydrogen bonding between PN and water molecules. (b) shows the hydrogen-bonding between PAS and the water molecules.

Figure 10 depicts the hydrogen bonding within each layer of PN and PAS. **Figure 10 a)** illustrates the hydrogen bonding between PN and the water molecules located in the interstitial spaces in the layer below. There are no intermolecular hydrogen bonds between the PN molecules. **Figure 10 b)** shows how the PAS molecules are hydrogen bonded to each other *via* interstitial water molecules and *via* the NH_2 and COO^- moieties. Two ring motifs are generated by hydrogen bonding. The ring motif shaded blue involves six bond donors, six acceptors, and 32 atoms, *i.e.*, four PAS molecules and two water molecules. The ring motif shaded pink involves six hydrogen bond donors, six hydrogen bond acceptors, and 24 atoms consisting of four molecules of PAS and two molecules of water. In both cases water acts as a hydrogen bond linker between the PAS molecules.

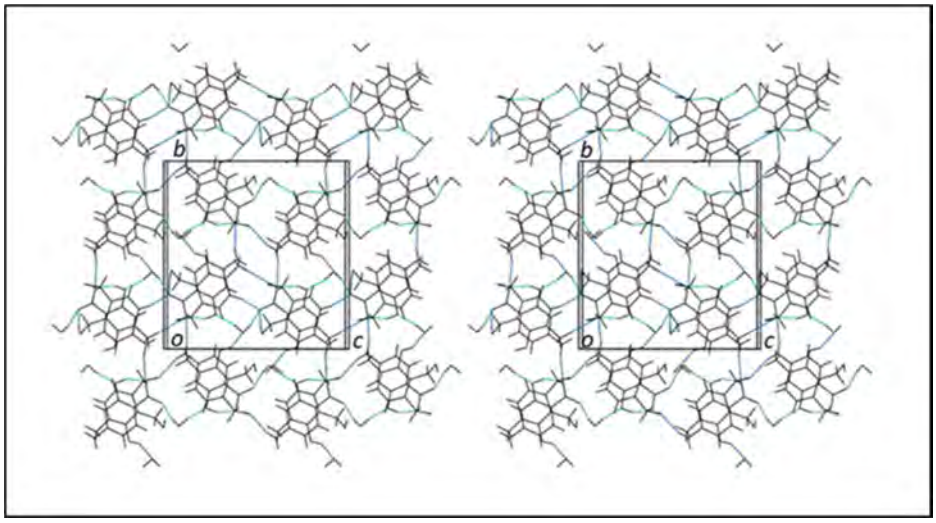

Figure 11: Shows the integration of the two layers shown in Figure 10 (a) and (b). The 3D view depicted here (view down *a* axis) demonstrates the complexity of the hydrogen bonding between layers. The blue lines are hydrogen bonds formed between the PN and PAS layers while the green lines are bonds within the PAS layer.

As mentioned previously, the packing arrangement of PN-PAS·H_2O is quite complex. For this reason and for simplicity the packing diagrams illustrated in **Figure 12** (next page) show only the upper layer viewed down each axial direction. The view onto the *bc* plane (**Figure 12** (top)) shows the overlap of consecutive alternating PN and PAS molecules. Furthermore, the alternating PN and PAS molecules are arranged in columns that are parallel to the *a* axis while consecutive columns stack along *c* (**Figure 12** (middle)). From the view onto the *ab* plane (**Figure 12** (bottom)), it can be seen that consecutive columns are displaced relative to each other along the *b* axis. It is also quite clear to see that the water molecules are located near the PAS molecules. This is consistent with **Figure 10 (b)** which shows that the PAS molecules are linked to each other *via* water molecules.

v. Crystal packing

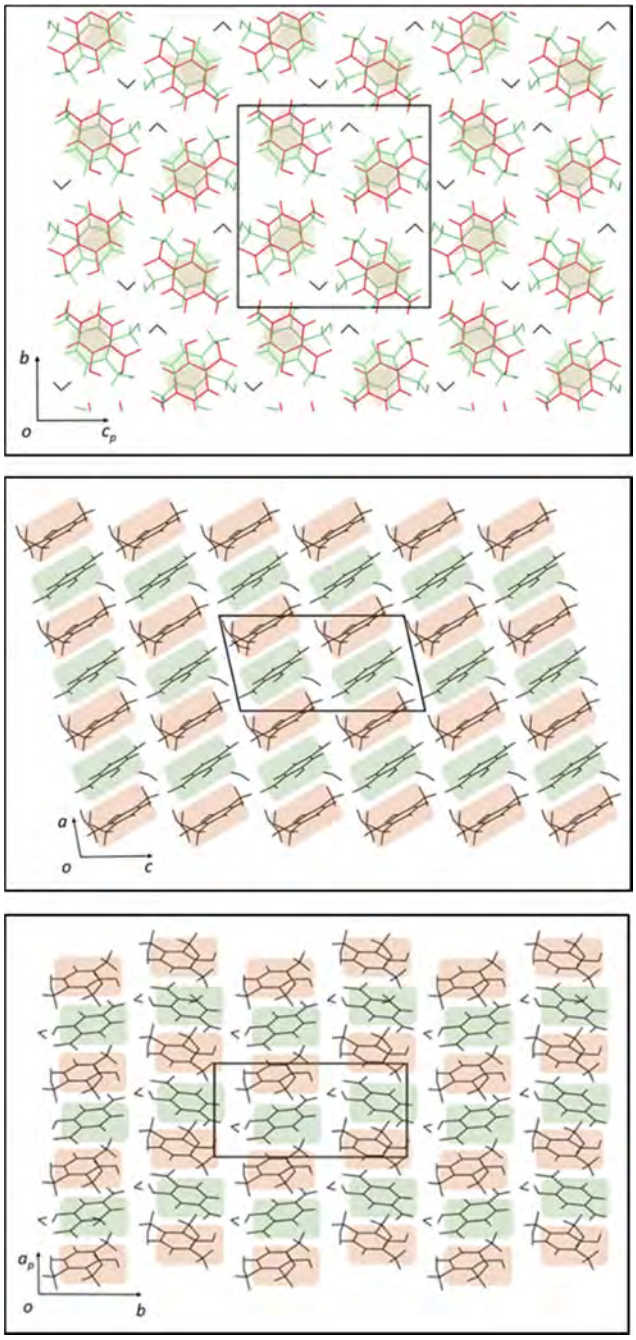

Figure 12: The packing arrangement of the PN-PAS·H_2O viewed along the different axes. The *top* image shows a view onto the *bc* plane containing alternating PN and PAS molecules. In the *middle* image the columns of alternating PN and PAS molecules are stacked parallel to the *a* axis and along the *c* axis. Bottom: view down the *c* axis shows the anti-parallel columns of alternating PN and PAS molecules stacked parallel to the *a* axis and along *b*.

4.2.2. Pyridoxine-pyrazinecarboxylate salt

The salt was prepared by grinding equimolar amounts of PN (0.81 mmol, 136 mg) and PAS (0.81 mmol, 101 mg). The LAG samples were prepared by the addition of 3 drops (~15 μL) of solvent (H_2O, MeCN, EtOAc and MeOH) to the PN and PCBA mixture prior to mechanical grinding in the ball mill. The neat grind involved the addition of no solvent.

4.2.2.1. Characterization

4.2.2.1. A) ATR-FTIR spectra of the PN-PCBA ground samples and bulk crystalline material

Shown in **Figure 13** are the FTIR spectra for PN, PCBA, NG, LAG samples and the bulk crystalline material. PN is characterised by a hydroxyl absorption peak at 3278 cm^{-1} and a strong C-OH band at 1019 $cm^{-1.}$ PCBA has a broad characteristic OH stretch between 2609-2181 cm^{-1} and a carbonyl stretch at 1715 cm^{-1}. The ground samples and bulk crystalline material have combined properties of both starting materials. The C=O absorption band at 1715 cm^{-1} in PCBA shifts to lower wavenumbers in both the LAG and crystalline materials. The broad OH stretch (2609-2181 cm^{-1}) in PCBA disappears in all LAG samples and in the crystalline material due to the transfer of the hydrogen atom from the carboxylic acid moiety of PCBA to the aromatic nitrogen of PN. Shifts in peak positions of the PCBA carbonyl bands (C=O and C-O) and OH of PN are reported in **Table 7**. The newly formed NH bond (present in all LAG samples) is masked by the broad -OH band between 2345 and 3148 cm^{-1} and results from strong hydrogen bonding in the salt. The NG spectrum exhibits characteristics of unreacted PCBA (at 3065, 2496, 1887 and 1716 cm^{-1}), and these are at slightly shifted peak positions compared to the pure PCBA. Reported in **Table 7** are characteristic vibrational modes of the PN-PCBA salt.

Table 7: Common stretching/bending frequencies for the putative salt obtained from the different preparations.

Vibrational modes	PCBA/cm^{-1}	PN/cm^{-1}	Neat/cm^{-1}	MeCN/cm^{-1}	EtOAc/cm^{-1}	MeOH/cm^{-1}	H_2O/cm^{-1}	SC*/cm^{-1}
vOH	-	3278	3258	3248	3253	3246	3244	3240
vC=O	1714	-	1716	1602	1603	1603	1601	1607
vC-O	1272	-	1274	1291	1291	1291	1290	1290
vC-OH	-	1019	1019	1019	1019	1019	1019	1018

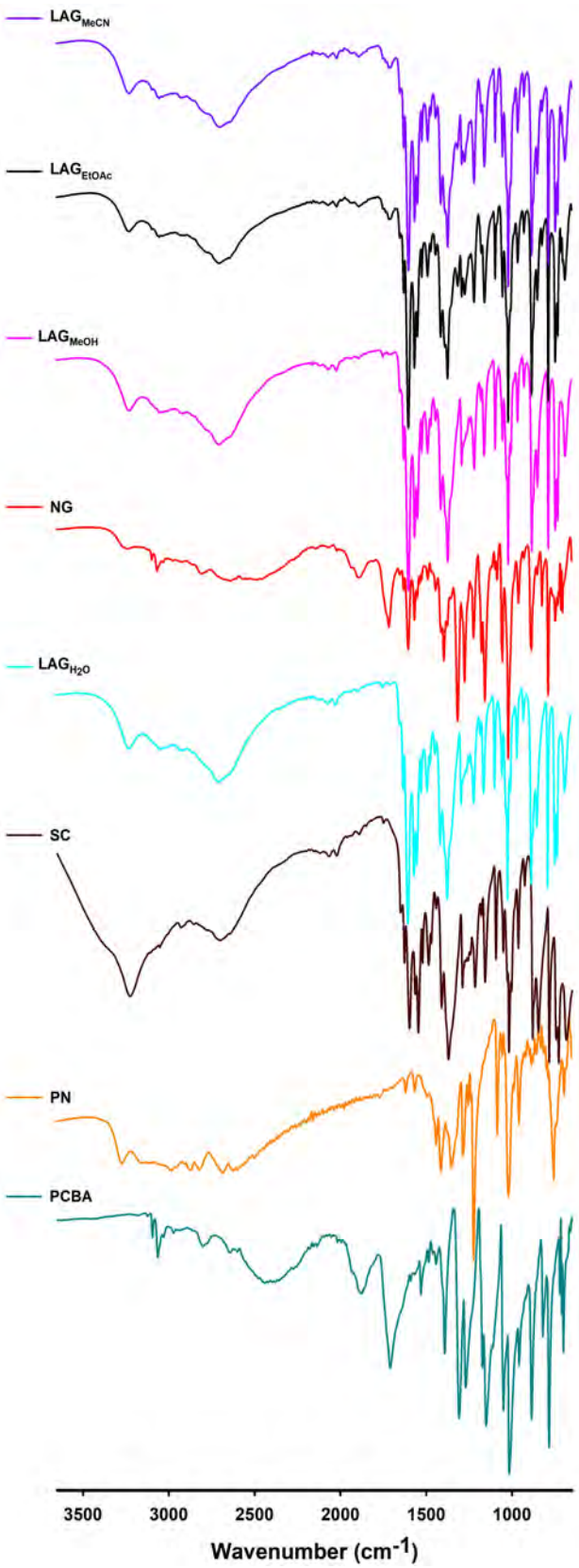

Figure 13: Stacked ATR-FTIR spectra for the PN, PCBA, bulk crystalline material, LAG_{MeCN}, LAG_{EtOAc}, LAG_{MeOH}, NG and LAG_{H2O} samples.

4.2.2.1. B) PXRD patterns of the PN-PCBA ground samples and bulk crystalline material

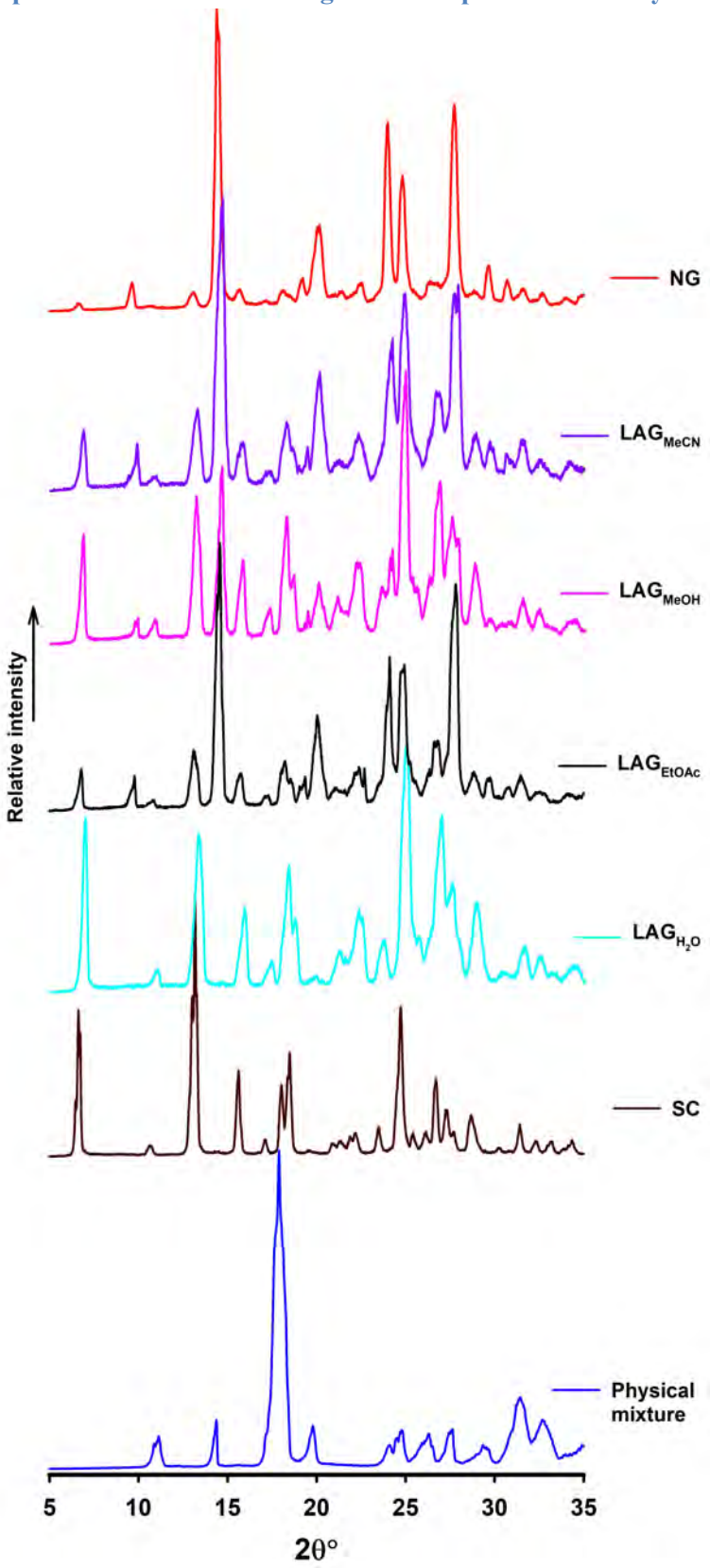

Figure 14: PXRD patterns for the physical mixture, bulk crystalline material, LAG_{MeCN}, LAG_{EtOAc}, LAG_{MeOH}, NG and LAG_{H2O} samples.

The powder patterns in **Figure 14** confirm that all grinds are different from the physical mixture suggesting the formation of new phases. The NG and LAG_{EtOAc}, LAG_{MeCN} and LAG_{MeOH} have similar diffraction patterns even though some of the peaks align with those present in the physical mixture. This may indicate the presence of unreacted starting material. However, there are several peaks that are common between the ground samples and the bulk crystalline material 6º, 11º, 14º, 17º and 19º (2θ), which indicate that these phases are the same. The LAG_{H2O} sample also exhibits a pattern comparable to that of the crystalline sample implying that co-grinding with water results in full conversion of the starting materials.

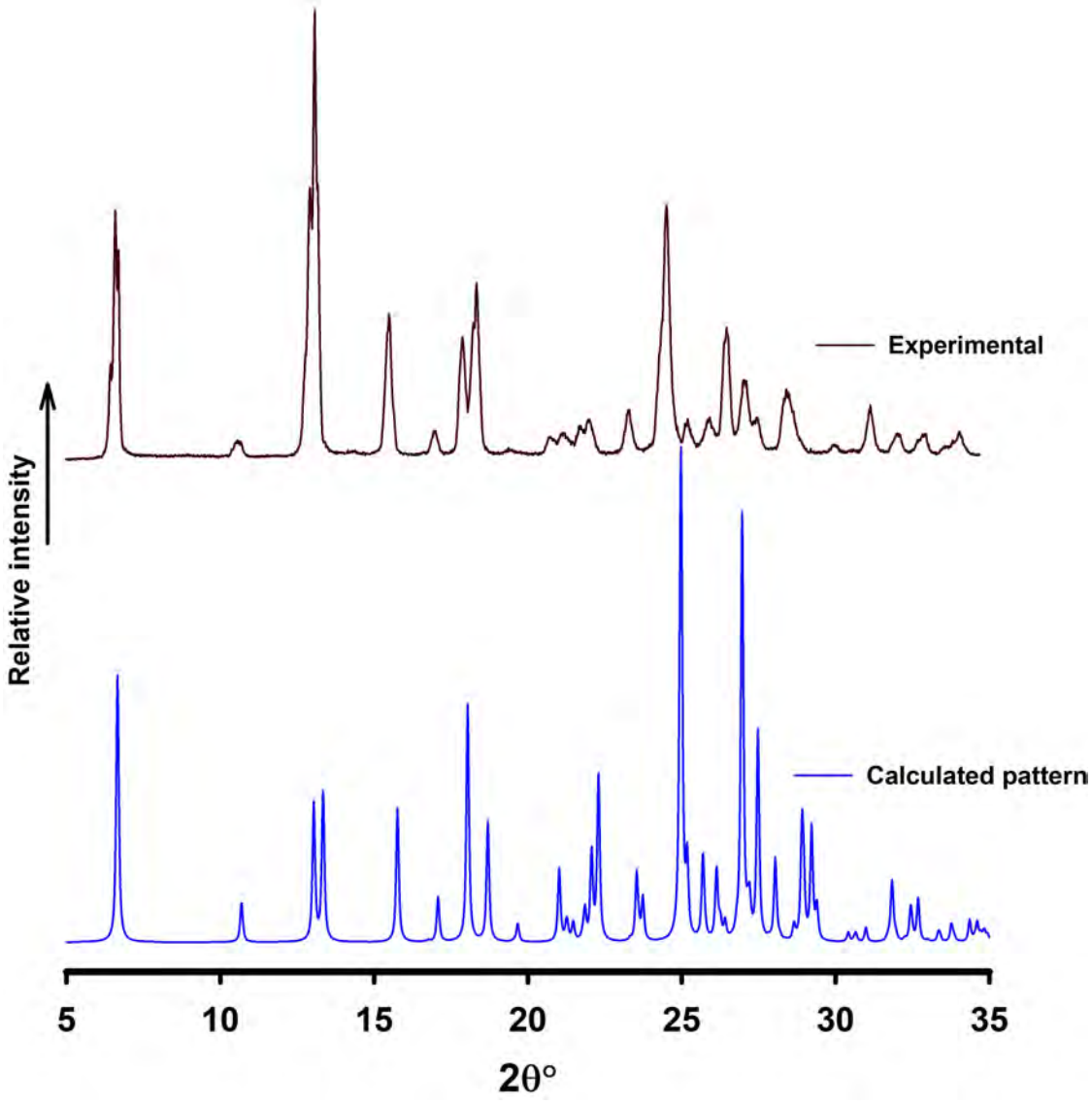

Figure 15: PXRD patterns of the bulk crystalline material compared to the pattern calculated from structural data.

The crystals grown using the slow evaporation method were gently ground into fine a powder using a mortar and pestle prior to PXRD analysis. **Figure 15** shows how closely the PXRD patterns of the crystalline sample and the calculated pattern match even though the peaks are slightly offset which is probably due to the different temperatures at which the data were collected. This indicates that the selected single crystal and bulk material are identical.

4.2.2.1. C) Thermal analysis of the PN-PCBA ground samples and bulk crystalline material

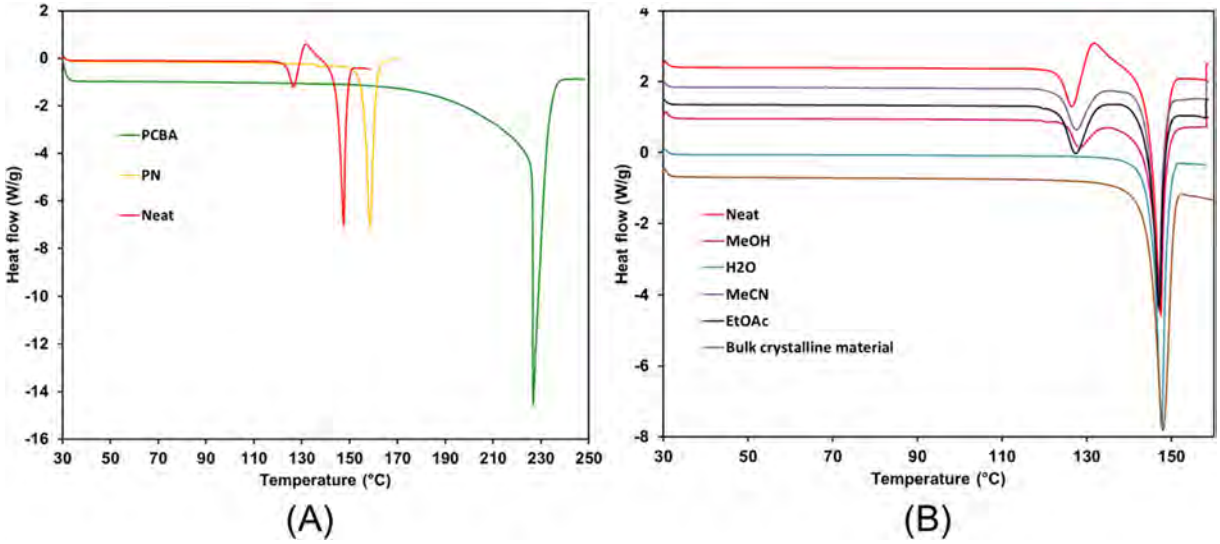

Figure 16: (A) DSC thermogram of the starting materials (PCBA and PN) and NG sample. (B) is the stacked DSC thermograms for the bulk crystalline material, NG and LAG samples (exo↑).

The DSC thermograms of the API, PN and PCBA, presents the melt endotherm between 153.1-158.5 °C for PN and between 226.7-22.8 °C for PCBA. The melting point of NG occurs at a lower temperature (142.0-147.4 °C) than both starting materials (**Figure 16 (A)**) and is similar to the melting point of all LAG samples (**Figure 16 (B)**). All the temperatures at which the thermal events occur are presented in **Table 8** (data for melt onset and peak temperature are presented here). The LAG_{H2O} shows a single endotherm while the other LAGs and NG exhibit two endotherms. The first set of endotherms occur at 122.9-128.3 °C. For the NG sample, this endotherm is followed by recrystallisation at ~130 °C. Upon further heating the sample melts. This was supported by the temperature cycling of the sample; heating to slightly beyond the exotherm and then cooling to room temperature followed by reheating the sample. After the second heating cycle the first endotherm disappears and only the melt endotherm remains (see **Figure 17 (A)**), which could imply that heating assists with the full conversion of the starting materials.

Table 8: Melt onset and peak temperatures of the PN-PCBA salt.

Samples	First endotherm		Recrystallisation (°C)	Second endotherm	
	T_{onset} (°C)	T_{peak} (°C)		T_{onset} (°C)	T_{peak} (°C)
NG	122.9	126.5	131.6	141.9	147.4
LAG_{H2O}	-	-	-	142.5	147.6
LAG_{MeOH}	124.9	128.3	-	140.6	147.3
LAG_{MeCN}	122.9	127.4	-	141.1	146.9
LAG_{EtOAc}	123.2	127.4	-	140.6	147.1
SC	-	-	-	143.9	149.0

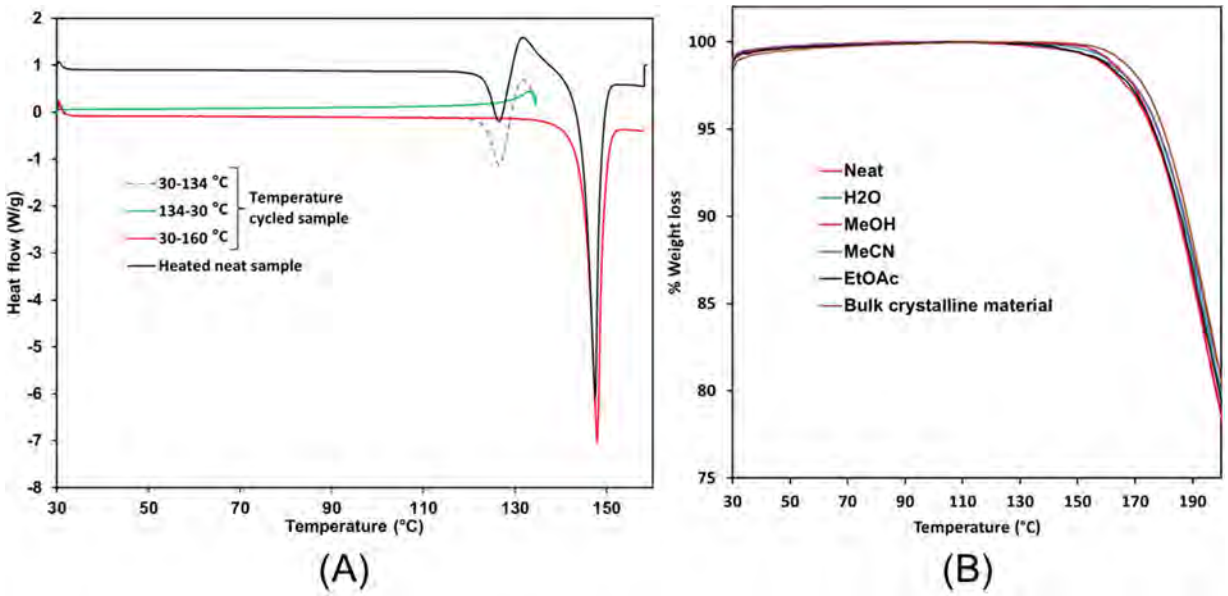

Figure 17: (A) Stacked DSC thermograms of the reheated NG sample and reheated sample (exo↑). (B) TGA thermogram for the bulk crystalline material, neat and LAG samples.

When the other LAG samples (MeOH, MeCN and EtOAc) were temperature cycled, the small endotherm re-appears at a lower temperature (103-109 °C). These DSC thermograms have been included in the **appendix** (**Figure 2**) since more work is required to gain insight into the thermal behaviour of these samples. However, the current theory is that it may be unreacted starting materials or a different phase. The unreacted starting material is evident in the PXRDs presented earlier. The DSC thermogram for the bulk crystalline material reveals a melting point between 141.1-148.0 °C that is similar to the NG and LAG samples. For all the samples, including bulk crystalline material, there is no mass loss evident during the heating of the samples, see TGA thermograms **Figure 17 (B)**.

4.2.2.1. D) Singe crystal X-ray analysis of the PN-PCBA ground samples and bulk crystalline material

Single crystals were prepared by dissolving equimolar amounts of PCBA (0.08 mmol, 10.4 mg) and PN (0.08 mmol, 13.6 mg) in approximately 6 ml MeCN and 2 ml MeOH and heating the solution to 50 °C to fully dissolve the components. The solution was left to evaporate slowly under ambient conditions. A single crystal suitable for X-ray diffraction was selected for SCXRD. Crystals were also produced from a mixture of EtOAc and MeOH in a 3:1 (v/v) volume ratio and they exhibited the same properties as those grown from MeCN and MeOH.

i. Data collection and space group determination

Unit cell parameters, crystal system, space group and single crystal data were collected on Bruker D8 Venture diffractometer. The PN-PCBA salt crystallises in the space group $P2_1/n$.

ii. Structure solution and refinement

Table 9: Data-collection and refinement parameters for PN-PCBA salt.

Data-collection and refinement parameters	
Formula unit	$(C_8H_{12}NO_3)$ $(C_5H_3N_2O_2)$
Formula mass (g mol^{-1})	293.28
Crystal system	monoclinic
Space group	$P2_1/n$ (No. 14)
a/Å	4.5766(2)
b/Å	26.5210(12)
c/Å	10.5787(5)
α/°	90
β/°	90.855(2)
γ/°	90
Volume (Å^3)	1283.86(10)
Z	4
D_{calc} (g cm^{-3})	1.517
F (000)	616
μ (MoKα) (mm^{-1})	0.118
Crystal size (mm^3)	0.10 x 0.14 x 0.17
Temperature (K)	100
Range scanned □ (º)	2.1- 28.3
Index ranges	-5: 6 ; -35: 35 ; -14: 14
Total number of reflections collected	46424
Number of unique reflections	3180
Number of reflections with I > 2σ (I)	2677
Number of least-squares parameters	208
R_{int}	0.051
S	1.04
R_1 (I > 2σ (I))	0.0342
wR_2	0.0904
Weighting scheme	a = 0.0387, b = 0.7130
$(\Delta/\sigma)_{mean}$	0.00
Δρ excursions (e Å^{-3})	0.31

SHELXT was used to solve the structure and SHELXL was used for structural refinement. All atoms were defined anisotropically based on well-behaved isotropic temperature factors and hydrogen atoms

were placed in idealised positions in a riding model. For heteroatoms, hydrogen atoms were refined using peaks observed from the difference Fourier map and data collection and refinement parameters of the PCBA-PN salt are summarized in **Table 9**.

iii. Molecular structure

The asymmetric unit consists of one molecule of PCBA and one molecule of PN with proton transfer from the carboxylic acid of the PCBA to the nitrogen in the PN ring evident, **Figure 18 (A)**, indicating that a salt has been formed. From the crystal structure it could be established that salt formation had occurred since a hydrogen atom covalently bonded to the nitrogen atom of the pyridine ring of PN could be modelled. This is supported by the individual bond lengths of the carboxylate moiety of PCBA, see **Table 10.**

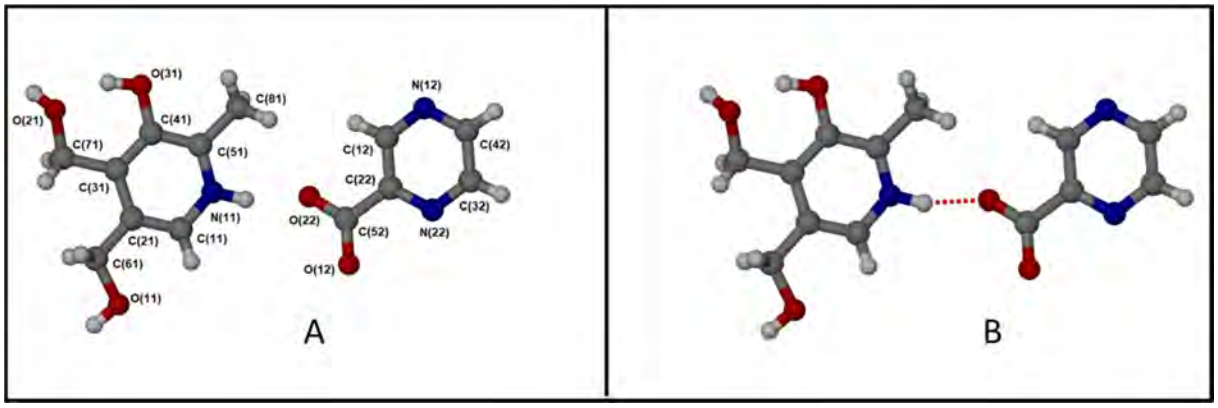

Figure 18: (A) Labelled, molecular diagram for PN-PCBA salt and (B) Asymmetric unit of the PN-PCBA salt showing hydrogen bonding between the moieties.

Table 10: Bond lengths of the carboxylate and pyridinium bonds in the PN-PCBA salt compared to the selected structures in the CSD

PCBA	This work	Carboxylic acid bonds	Refcode
	Carboxylate bonds		
C52-O22	1.2501(14)	1.317(2)	PYAZAC01[7]
C52-O12	1.2581(15)	1.2517(19)	
PN	**Pyridinium bonds**	**Pyridine bonds**	
C51-N11	1.3430(14)	1.3327(3)	BITZAF[7]
C11-N11	1.3491(15)	1.3406(3)	

iv. Hydrogen bonding and packing arrangement

In the asymmetric unit, PN and PCBA are hydrogen bonded to each other *via* a charge-assisted N^{+}-H···O^{-} interaction (illustrated in **Figure 18 (B)**). The pyridine nitrogen atom N11 of PN hydrogen bonds to the carboxylate oxygen atom O22 on PCBA. The hydrogen bonded unit of PN-PCBA is part of a larger hydrogen bonded network with the carboxylate oxygen atom O12 of PCBA being bifurcated, forming two O-H···O hydrogen bonds with another PN molecule through an aliphatic hydroxyl group (O11). This

hydrogen bonding is repeated through a centre of inversion halfway along the *b* axis forming a ring motif (shaded red). The red shaded ring motif, **Figure 19**, contains 20 atoms, four H-bond donor atoms and four acceptor atoms and involves two PN molecules and two PCBA molecules ($\boldsymbol{R_4^4(20)}$). The second hydrogen bond is with an aliphatic hydroxyl group O2 belonging to a different PN molecule and is itself hydrogen bonded to a symmetry related PCBA molecule, see **Figure 19**. This hydrogen bond network is repeated through a centre of inversion at the centre of the unit cell also forming a ring motif (yellow shaded). The yellow shaded hydrogen bonded ring motif at the centre of the unit cell comprises of 18 atoms, four hydrogen bond donor atoms and two acceptor atoms and involves two PN molecules and two PCBA molecules ($\boldsymbol{R_4^2(18)}$), **Figure 19**. There is an intramolecular hydrogen bond within PN between the aromatic hydroxyl and a neighbouring aliphatic hydroxyl group. The two hydrogen bonded networks (indicated by shading) share atoms and molecules forming hydrogen bonded sheets that span the crystal parallel to the *c* axis while consecutive sheets stack along *b*.

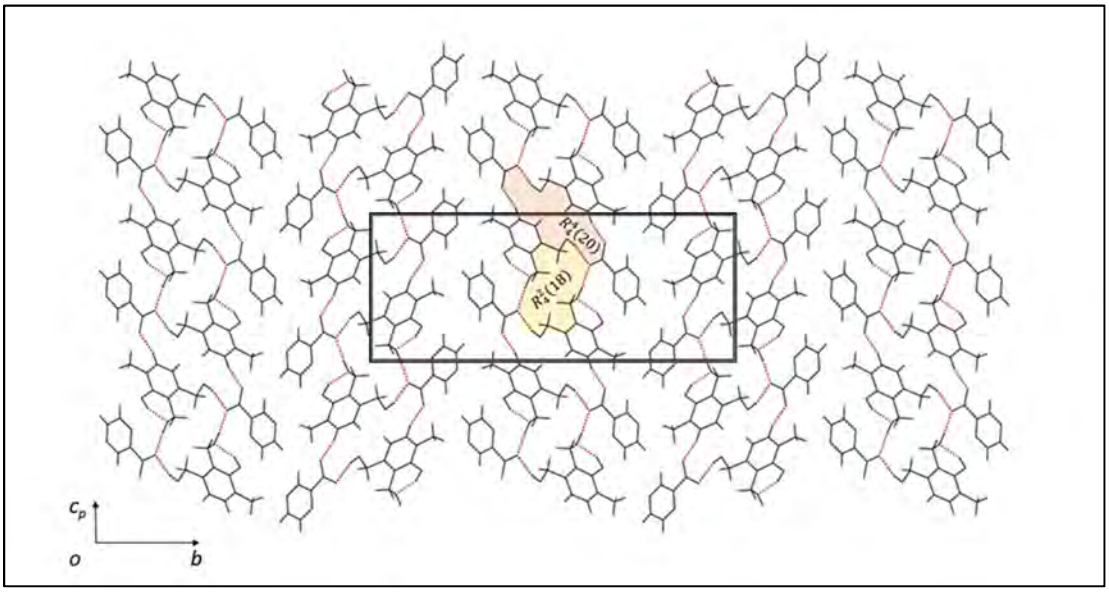

Figure 19: Alternating hydrogen bonded sheets parallel to *c* and stacked along the *b* axis.

Moreover, when the sheets are viewed down the *ac* diagonal it becomes apparent that consecutive sheets are inclined to each other by ~78.2° (Mercury[8]) generating a zig-zag motif along *b* (**Figure 20 (A)**).

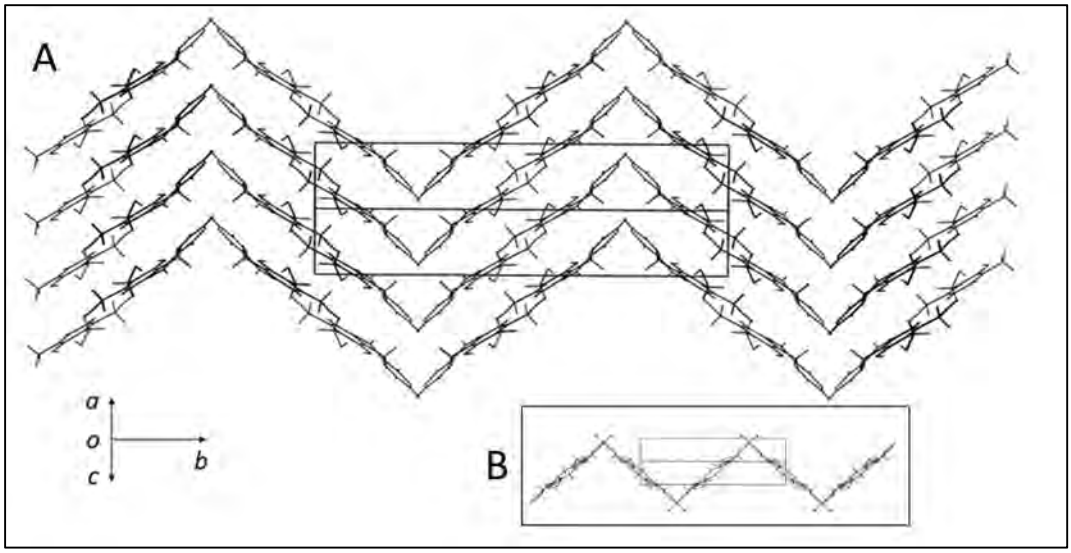

Figure 20: Zigzag pattern of the layers and hydrogen bonding between subsequent layers (insert) viewed down the *c* axis.

The sheets are stacked in layers perpendicular to the *ac* diagonal direction. Consecutive layers are hydrogen bonded to each other *via* a single C-H···N interaction between a nitrogen atom in the pyrazine ring (N12) and hydrogen atom on the methyl group (C81) on PN. All the hydrogen bond interactions and parameters are reported in **Table 11.** The COO^--(pyridine$^+$-H) interaction bond length of this salt is within the average N^+-H···O^- bond lengths of 2.652(1).[7]

Table 11: Hydrogen bond parameters for PN-PCBA salt.

D-H···A	D-H (Å)	H···A (Å)	D···A (Å)	D-H···A (°)	Symmetry code
N11-H11N···O22	0.937(17)	1.795(17)	2.7060(13)	163.5(15)	1+x,y,1+z
O31-H41···O21	0.93(2)	1.74(2)	2.5832(12)	148.5(18)	.
O31-H41···N22	0.93(2)	2.37(2)	2.9190(13)	117.2(16)	.
O11-H61···O12	0.88(2)	1.88(2)	2.7367(12)	163.9(19)	2-x,1-y,1-z
O21-H71···O12	0.89(2)	1.74(2)	2.6209(12)	171.9(19)	.
C11-H11···O11	0.95	2.48	3.2831(14)	143	3-x,1-y,2-z
C61-H61B···O21	0.99	2.47	3.2101(14)	131	1+x,y,z
C81-H81A···O22	0.98	2.46	3.1589(16)	128	1+x,y,1+z
C81-H81C···N12	0.98	2.59	3.5265(17)	161	3/2+x,3/2-y,1/2+z

4.3. Summary

Attempts at preparing cocrystals of PN with different coformers resulted in the isolation and characterisation of two multicomponent salts, *i.e.*; PN-PAS·H_2O and PN-PCBA. Both were prepared using mechanochemistry and slow evaporation. After an extensive search in the CSD[7], neither of these salts were found to have been previously reported.

References

(1) Doleal M., Zitko J. and Jamplek J. Pyrazinecarboxylic Acid Derivatives with Antimycobacterial Activity. In *Understanding Tuberculosis - New Approaches to Fighting Against Drug Resistance*; Cardona, P.-J., Ed.; InTech, **2012**.

(2) Kresge N., Simoni R. D. and Hill R. L. Esmond E. Snell and the B Vitamins. *J. Biol. Chem.* **2005**, *280*, e10–e11.

(3) Calderón-Ospina M. O. and Nava-Mesa. B Vitamins in the Nervous System: Current Knowledge of the Biochemical Modes of Action and Synergies of Thiamine, Pyridoxine and Cobalamin. *CNS Neurosci. Ther.* **2020**, *26*, 5–13.

(4) Ganduri R., Cherukuvada S. and Guru Row T. N. Multicomponent Adducts of Pyridoxine: An Evaluation of the Formation of Eutectics and Molecular Salts. *Cryst. Growth Des.* **2015**, *15*, 3474–3480.

(5) Komasa A., Babijczuk K., Dega-Szafran Z., Gołdyn M., Bartoszak-Adamska E., Szafran M. and Cofta G. Interactions of Pyridoxine (Vitamin B6) with Squaric Acid and Water. Experimental and Theoretical Studies. *J. Mol. Struct.* **2022**, *1251*, 1-13.

(6) Drozd K. V., Manin A. N., Churakov A. V. and Perlovich G. L. Drug-Drug Cocrystals of Antituberculous 4-Aminosalicylic Acid: Screening, Crystal Structures, Thermochemical and Solubility Studies. *Eur. J. Pharm. Sci.* **2017**, *99*, 228–239.

(7) Ferrence G. M., Tovee C. A., Holgate S. J. W., Johnson N. T., Lightfoot M. P., Nowakowska-Orzechowska K. L. and Ward S. C. *CSD Communications* of the Cambridge Structural Database. *IUCrJ* **2023**, *10*, 6–15.

(8) Macrae C. F., Sovago I., Cottrell S. J., Galek P. T. A., McCabe P., Pidcock E., Platings M., Shields G. P., Stevens J. S., Towler M. and Wood P. A. *Mercury 4.0*: From Visualization to Analysis, Design and Prediction. *J. Appl. Cryst.* **2020**, *53*, 226–235.

Chapter 5: Eutectics of isoniazid

5.1. Introduction

A eutectic is a crystalline, multicomponent solid formed when the homomolecular interactions between components outweighs the heteromolecular interactions, resulting in a product with lower a melting point compared to the individual starting materials but having a similar crystalline arrangement.[1,2] In the pharmaceutical industry, the aqueous solubility of a solid material (*i.e.,* solid oral medicines) is very important as it contributes to the bioavailability of the medicine and hence, its therapeutic effect.[3] Recently, solids displaying eutectic properties have been of particular interest predominantly due to its enhanced properties. In this regard, eutectic formation may lead to the production of solids with enhanced aqueous solubility and dissolution rates, and hence, improved bioavailability.[1,2,4]

As previously stated, isoniazid (INH) and pyrazinamide (PYR) are typically used in the treatment of tuberculosis[5], while pyridoxine (PN) acts as a coenzyme in the synthesis of neurotransmitters. A common side effect of isoniazid therapy in TB patients is that it leads to a deficiency of pyridoxine, resulting in the development isoniazid-induced neuropathy. To counteract this, patients are given pyridoxine supplementation (in the hydrochloride form) alongside INH, administered separately or given in the form of a combination tablet of INH and PN.[6,7] Moreover, anti-TB fixed dose combinations of INH have stability issues which result in reduced INH bioavailability impeding its action.[5]

5.2. Present study

To combat the side effects associated with isoniazid, the aim was to cocrystallise INH with PN, pyridoxine hydrochloride (PN·HCl) and separately with PYR in order to reduce isoniazid-induced neuropathy and to enhance the solubility of PYR. Cocrystallisation of INH with PN, PN·HCl and PYR was carried out according to the methods described in Chapter 2. The cocrystallisation experiments led to the formation of products displaying eutectic properties instead of cocrystals or salts, **Table 1**. Attempts to synthesise crystals by slow evaporation failed as only one of the components crystallised from solution, which is typical of eutectic adducts.[4] Presented in **Figure 1** are the molecular structures of the compounds investigated in this chapter.

Table 1: Summary of synthesized eutectics.

Compound	Nature	Synthesis methods			Reported
		Neat	LAG	SE*	
INH:PN	Eutectic	✓	MeOH, H_2O, MeCN and EtOAc	-	Ganduri *et al*, 2015[2]
INH-PYR	Eutectic	✓	MeOH, H_2O, MeCN and EtOAc	-	Cherukuvada and Nangia, 2012[1]
INH:PN HCl	Eutectic	✓	MeOH, H_2O, MeCN and EtOAc	-	This work

SE*= slow evaporation

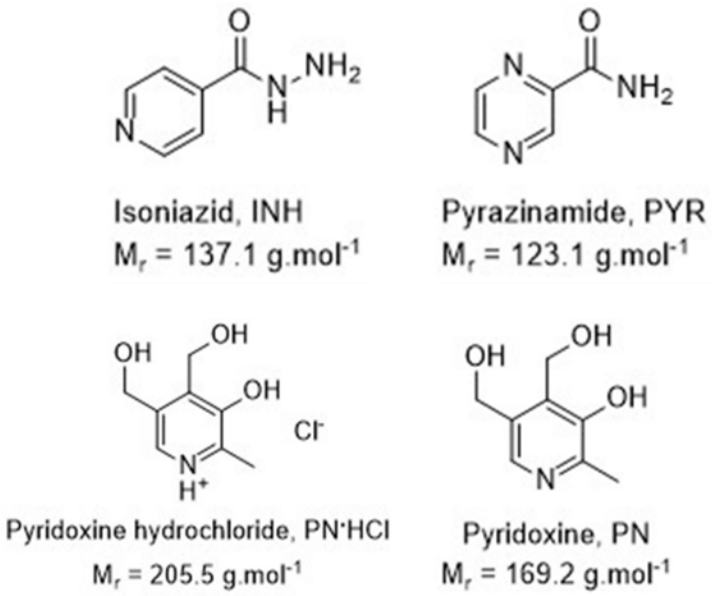

Figure 1: Molecular diagrams and acronyms for the compounds investigated in this chapter.

5.2.1. INH:PYR compound exhibiting eutectic properties

The INH:PYR eutectic product was previously synthesized and reported by Cherukuvada and Nangia.[1] In this work, the eutectic product was synthesised following the LAG method with a selection of solvents to probe the possible formation of a different phase to that obtained using the neat grinding/milling approach (NG).

5.2.1.1. Characterisation

5.2.1.1. A) ATR-FTIR spectra for the milled eutectic samples of INH:PYR

The IR spectra depicted in **Figure 2** indicates no significant differences between the milled products and the physical mixture, although minor differences in the intensities were noted.

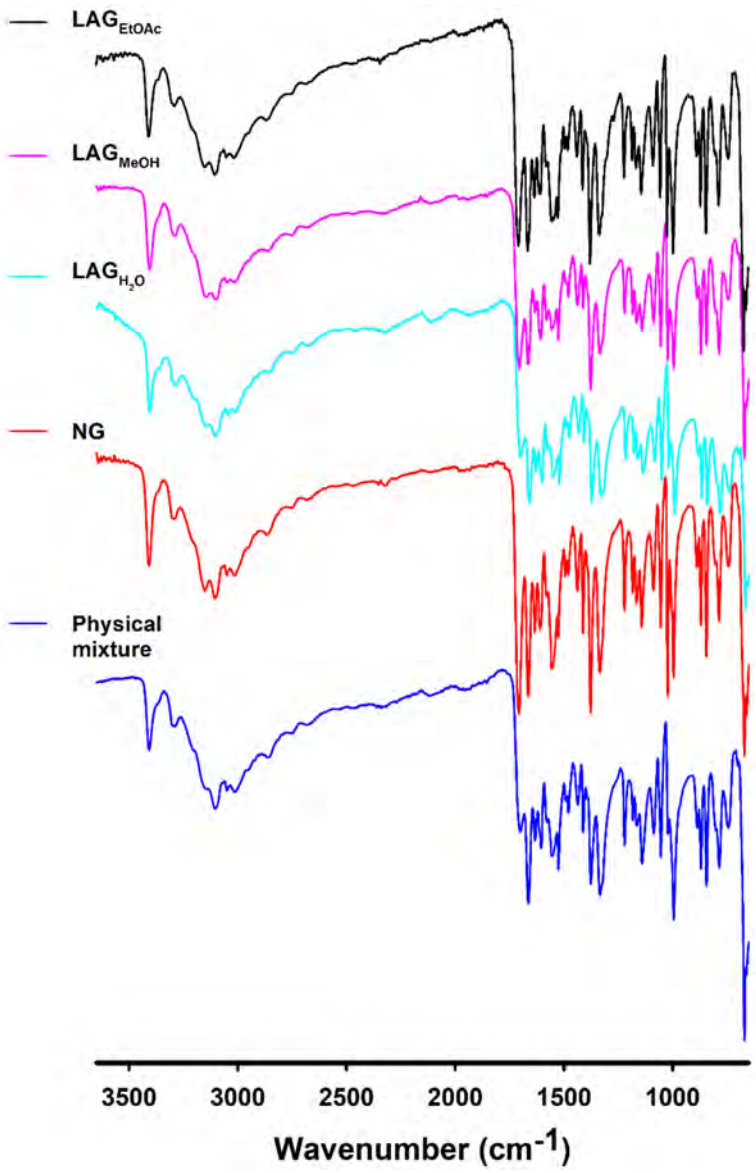

Figure 2: ATR-FTIR spectra comparing the physical mixture and samples prepared using NG/LAG methods.

5.2.1.1. B) PXRD characterization of INH:PYR eutectic samples

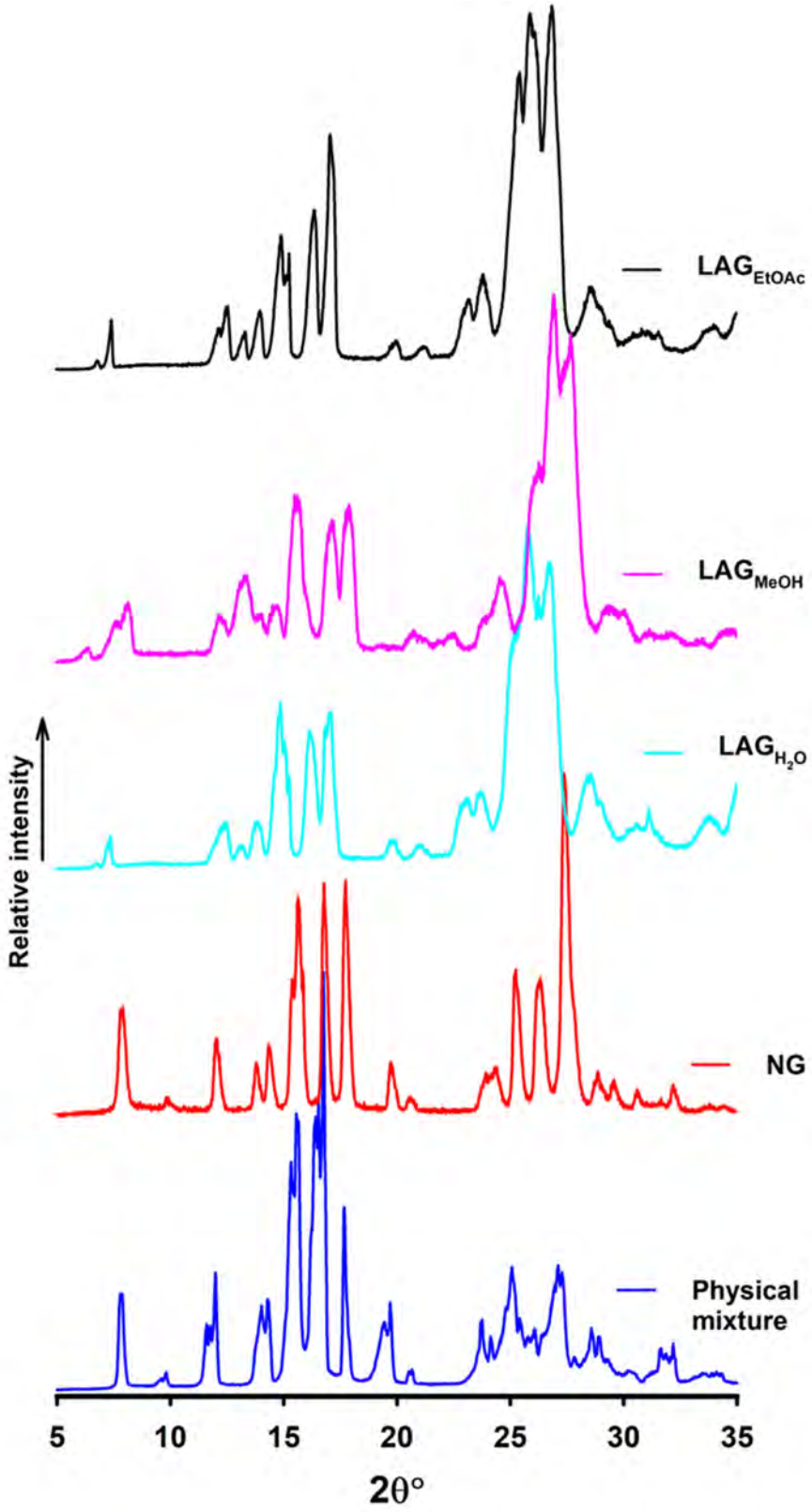

Figure 3: PXRD diffractogram comparison of the INH:PYR physical mixture with the NG, LAG_{H2O}, LAG_{MeOH}, and LAG_{EtOAc} samples.

Overall, the PXRD patterns for the ground samples are similar to each other and to the physical mixture, see **Figure 3**. However, minor differences between the LAG samples and NG sample were observed at the peak position at 6° (2θ) and the disappearance of the peak at 9° (2θ) in the LAG samples, in addition to differences in the fine structure of the peaks. This could be attributed to LAG samples exhibiting increased crystallinity, as well as to improved homogeneity achieved via the LAG process. There are no significant new peaks observed in the different profiles, and thus it was concluded that all the products are physical mixtures, which is in agreement with the observations made from the FTIR data.

5.2.1.1. C) Thermal analysis of the INH:PYR eutectic samples

DSC thermograms for INH and PYR are presented in **Figure 4 (A)**; with **Table 1** providing a summary of all temperatures corresponding to significant thermal events. From this dataset (**Figure 4 (A)** and **Table 1**) it is evident that the NG sample melts between 140.9-144.3 ºC, well below the melting point of the starting materials, which is characteristic of eutectic systems.[1] The LAG samples shown in **Figure 4 (B)** have similar melting point ranges to the NG sample (140.5-144.5 ºC), re-enforcing the conclusion that the same phase is obtained independent of the solvent used. The thermogram of the NG sample is in accordance with that reported in the literature.[1]

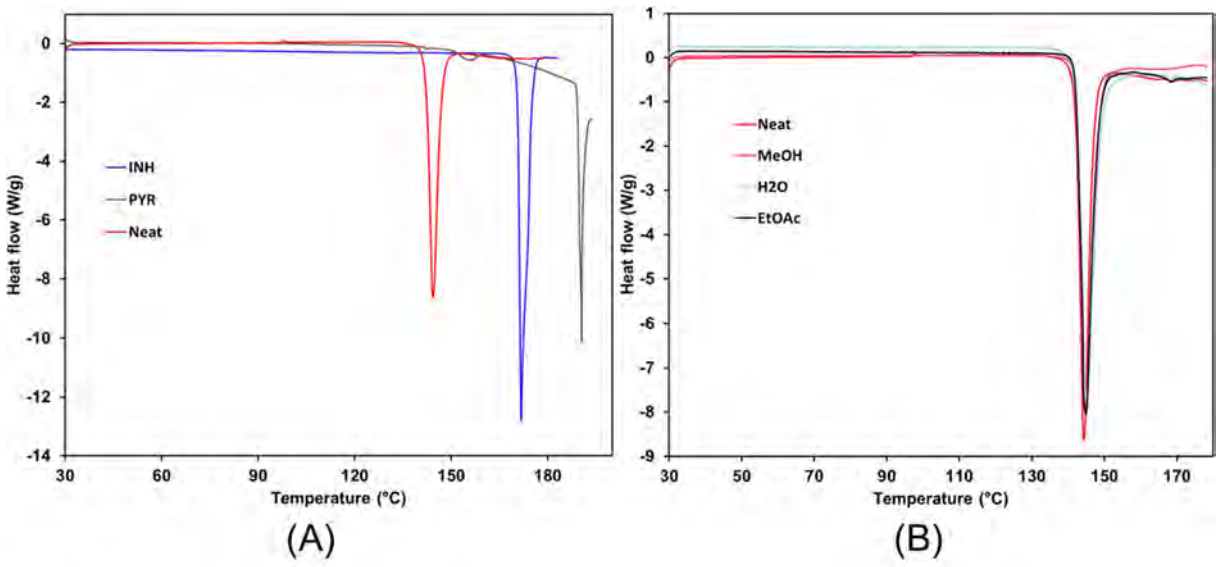

Figure 4: (A) DSC thermograms of the INH, PYR and NG samples. (B) DSC thermograms of the NG, LAG_{H2O}, LAG_{MeOH}, and LAG_{EtOAc} samples (exo↑).

Table 2: Melt onset and peak temperatures of INH:PYR eutectic samples.

(INH:PYR)	T_{onset} (°C)	T_{peak} (°C)
INH	169.7	171.7
PYR	188.9	190.5
NG	140.9	144.3
LAG_{H2O}	140.5	145.1
LAG_{MeOH}	140.9	144.7
LAG_{EtOAc}	141.4	144.9

Shown in **Figure 5** (**A**) are the representative DSC thermograms of the INH:PYR mixtures at different mole fractions used to construct the phase diagram. **Figure 5** (**B**) is the phase diagram of the INH:PYR eutectic exhibiting a "V"-type pattern which is characteristic of eutectic compounds.[8] The eutectic composition is 1:1 mixture of INH and PYR, with melting point of 140.9 °C.

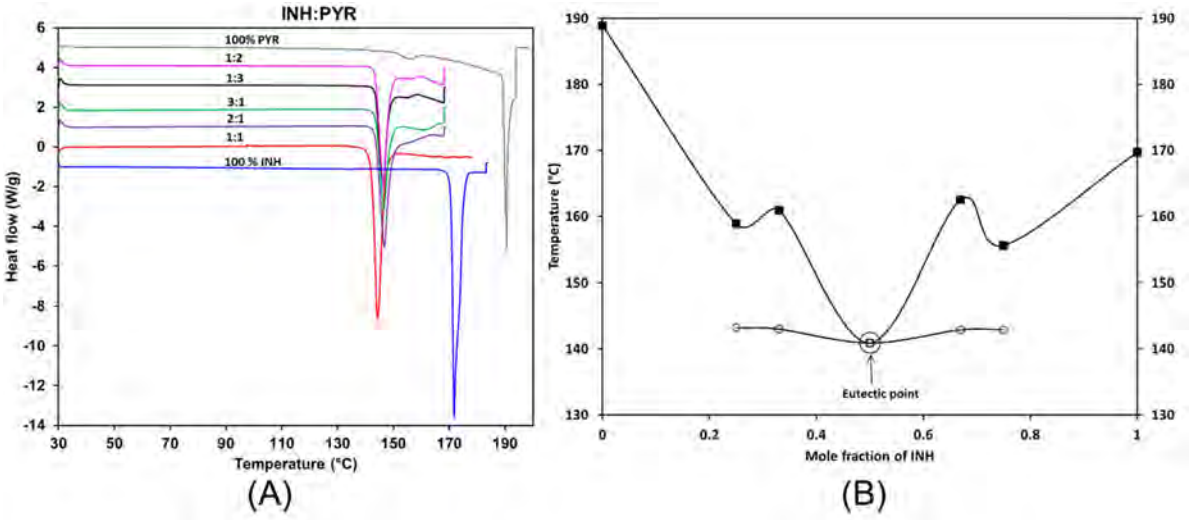

Figure 5: (A) Stacked DSC thermograms of pure INH, PYR and physical mixtures of INH:PYR in various mole fractions used to construct the phase diagram (exo↑). (B) The phase diagram of INH:PYR eutectic system. Solidus points = open circles and liquidus points = solid squares.

5.2.2. INH:PN and INH:PN·HCl compounds exhibiting eutectic properties

The INH:PN eutectic product was synthesised by Ganduri *et al*.[2] In this investigation, the eutectic product was synthesised following the LAG approach. This approach was used in an attempt to isolate a different phase compared to what is obtained using the neat grind method. Additionally, a similar set of experiments were performed with INH and PN·HCl (hydrochloride salt of PN) to determine if a different outcome could be achieved.

5.2.2.1. Characterisation

5.2.2.1. A) ATR-FTIR characterization of INH:PN and INH:PN·HCl samples

Figure 6 shows the IR spectra of the NG, LAG samples and physical mixtures of **(A)** INH:PN and **(B)** INH:PN·HCl. The resultant grinds for both combinations result in spectra similar to their corresponding physical mixtures with no apparent shifts in the peak positions; indicative of the formation of a mixture rather than a cocrystal/salt.

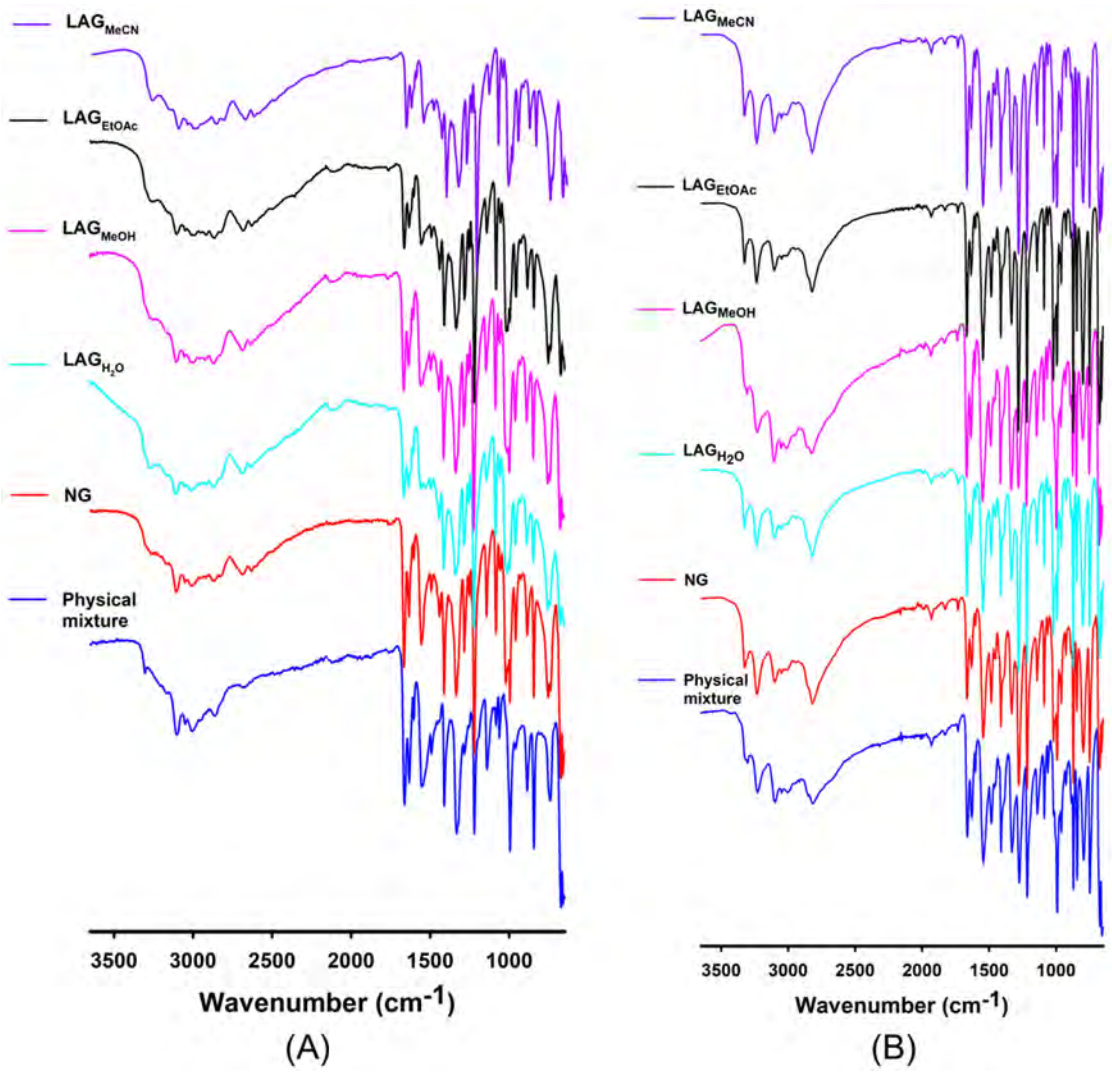

Figure 6: ART-FTIR spectra of the physical mixtures of (A) INH:PN and (B) INH:PN·HCl compared to the spectra of the corresponding NG, LAG_{H2O}, LAG_{MeOH}, LAG_{EtOAc} and LAG_{MeCN} samples.

5.2.2.1. B) PXRD characterisation of the INH:PN and INH:PN·HCl eutectic samples

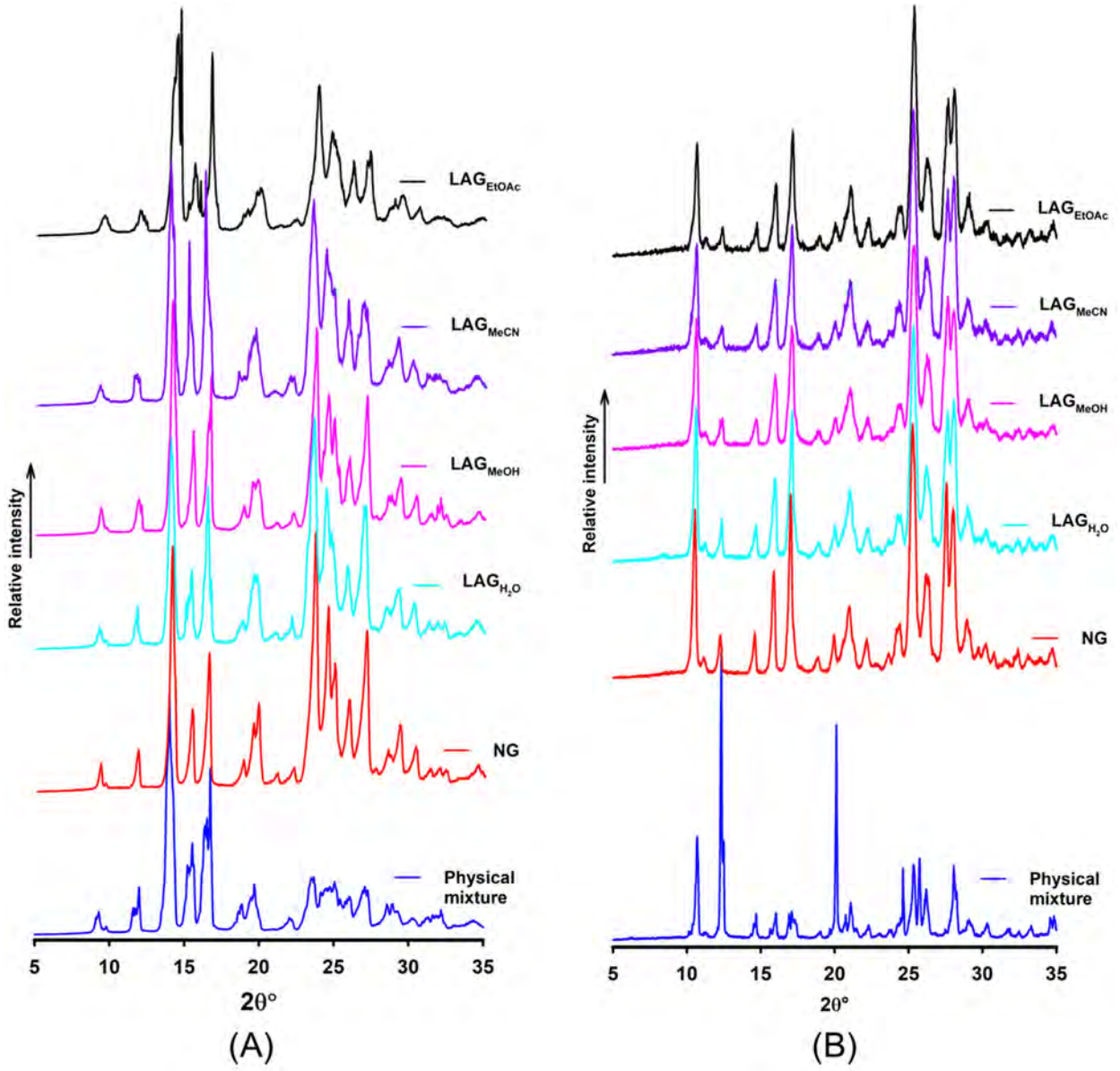

Figure 7: PXRD patterns of (A) INH:PN and (B) INH:PN·HCl and the corresponding diffractograms for the NG, LAG_{H2O}, LAG_{MeOH}, LAG_{EtOAc} and LAG_{MeCN} samples.

Powder X-ray diffraction of the ground samples was conducted in order to determine if different phases were obtained. The ground samples for eutectic mixtures of both INH:PN and INH:PN·HCl exhibit nearly identical PXRD profiles which also corresponds to the profiles of the physical mixtures, see **Figure 7 (A)** and **(B)**. Furthermore, the PXRD profiles of the INH:PN eutectic matches those reported in the literature[2]; and is in agreement with the FTIR data that a new complex has not been formed.

5.2.2.1. C) Thermal analysis of INH:PN and INH:PN·HCl eutectic samples

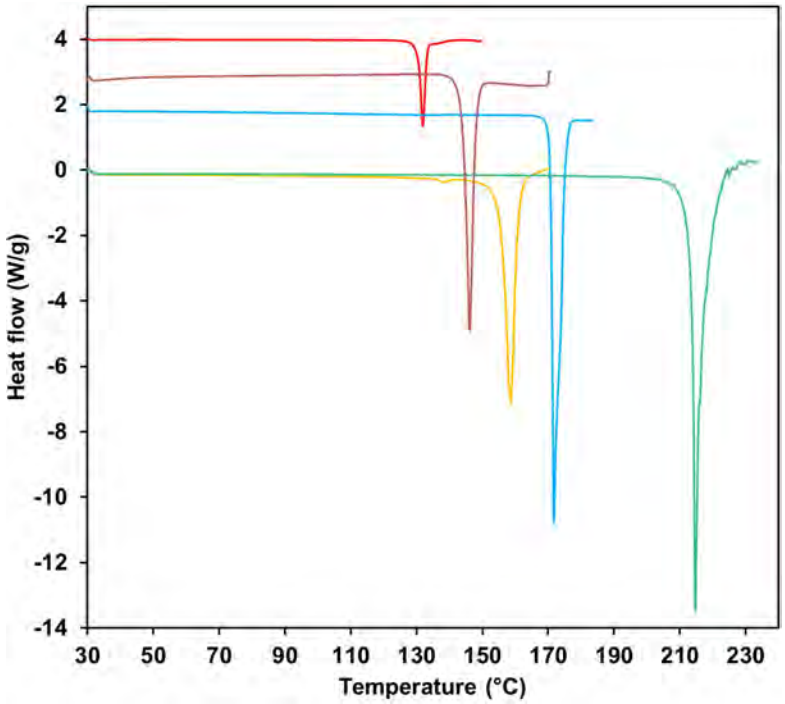

Figure 8: Stacked DSC thermograms for PN·HCl (green), INH (blue), PN (yellow) and the eutectic samples $NG_{INH:PN}$ (red) and $NG_{INH:PN·HCl}$ (brown) (exo↑).

DSC thermograms for the API, PN, INH and PN·HCl, show melt endotherms in the range 153.1-158.5 °C for PN, 169.7-171.7 °C for INH and 210.3-214.5 °C for PN·HCl, **Figure 8**. The NGs of INH:PN and INH:PN·HCl have melting points below all three of the melting points of the starting materials of 124.8-131.8 °C and 142.9-146.3 °C, respectively (**Figure 8**). The LAG samples also exhibit similar melting points to the NGs with melt endotherms between 127.4-133.9 °C for INH:PN and 139.6-146.4 °C for INH:PN·HCl as shown in **Figure 9 (A) and (B)**, respectively.

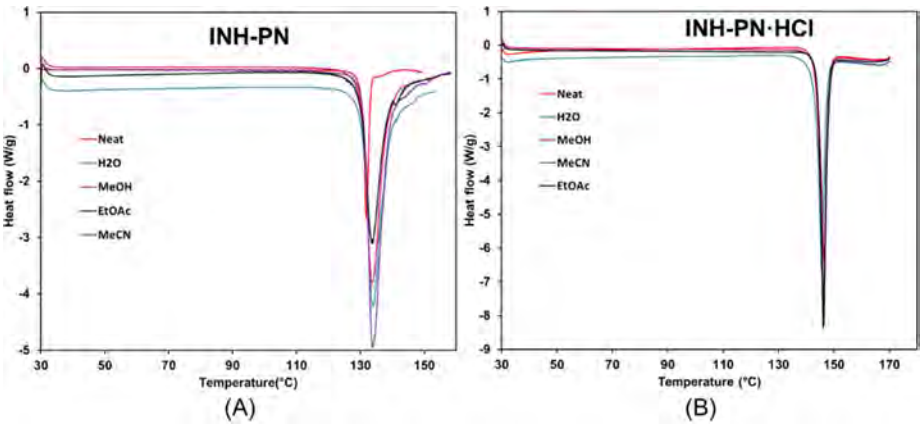

Figure 9: Comparison of DSC thermograms of (A) INH:PN eutectic and (B) INH:PN·HCl eutectic mixtures with their corresponding ground samples (NG, LAG_{H2O}, LAG_{MeOH}, LAG_{EtOAc} and LAG_{MeCN}) (exo↑).

Figure 10 (A) shows the DSC thermograms for the mole fractions of INH:PN·HCl used to construct the phase diagram shown in **Figure 10 (B)**. The eutectic composition is a mole fraction of 6:4 (INH:PN·HCl) at 148.6 °C. The data points were extrapolated from 4:6 to 7:3 (INH:PN·HCl) since the second endotherm of the ratios in between was not clearly distinguishable.

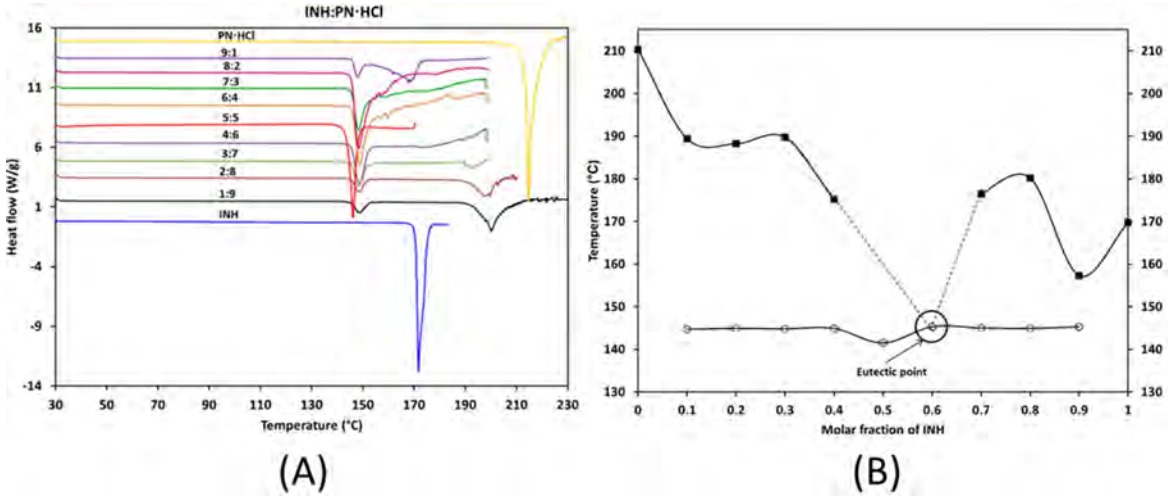

Figure 10: (A) Stacked DSC thermograms of INH, PN·HCl and physical mixtures of INH:PN·HCl in various mole fractions used to construct the phase diagram (exo↑). (B) Phase diagram of the INH:PN eutectic system. Solidus points = open circles and liquidus points = solid squares.

The DSC thermograms used to construct the INH:PN phase diagram are shown in **Figure 11 (A)** while the phase diagram is presented in **Figure 11 (B)**. The eutectic composition obtained from extrapolating the data points is the 1:1 mole fraction of INH:PN at 124.8 °C, which is different from the 1:4 (INH:PN) ratio that was reported by Ganduri *et al*.[2] The data points in **Figure 10 (B)** were extrapolated from 3:7 to 1:0 (INH:PN) because the data points for ratios in between could not obtained as the DSC profiles showed decomposition of these samples beyond 150 °C.

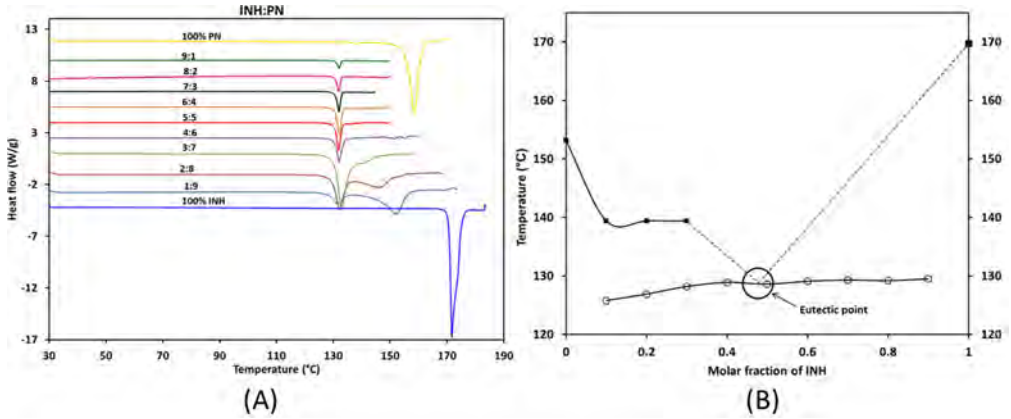

Figure 11: (A) Stacked DSC thermograms of INH, PN and the physical mixtures of INH:PN in various mole fractions used to construct the phase diagram (exo↑). (B) is the phase diagram of INH:PN eutectic system. Solidus points =open circles and liquidus points = solid squares.

Further investigations still need to be conducted to determine the differences in the results for INH:PN obtained in this study and those from previously reported data.

5.3. Summary

Attempts at preparing the cocrystals of INH with different coformers resulted in the isolation of three eutectic mixtures; INH:PYR, INH:PN and INH:PN·HCl, which were characterised and their phase diagrams successfully constructed. Two of the eutectics were reported previously, neither of these reports included information of eutectic formation involving PN·HCl.

References

(1) Cherukuvada S. and Nangi A. Fast Dissolving Eutectic Compositions of Two Anti-Tubercular Drugs. *CrystEngComm.* **2012**, *14*, 2579-2588.

(2) Ganduri R., Cherukuvada S. and Guru Row T. N. Multicomponent Adducts of Pyridoxine: An Evaluation of the Formation of Eutectics and Molecular Salts. *Cryst. Growth Des.* **2015**, *15*, 3474–3480.

(3) Moore M. D. and Wildfong P. L. D. Aqueous Solubility Enhancement Through Engineering of Binary Solid Composites: Pharmaceutical Applications. *J. Pharm. Innov.* **2009**, *4*, 36–49.

(4) Cherukuvada S. and Nangia A. Eutectics as Improved Pharmaceutical Materials: Design, Properties and Characterization. *Chem. Commun.* **2014**, *50*, 906–923.

(5) Salem A., Khanfar E., Nagy S. and Széchenyi A. Cocrystals of Tuberculosis Antibiotics: Challenges and Missed Opportunities. *Int. J. Pharm.* **2022**, *623*, 1-16.

(6) Levy L., Higgins L. J. and Burbridge T. N. Isoniazid-Induced Vitamin B6 Deficiency 1, 2, 3. *Am. Rev. Respi. Dis.* **1967**, 96, 910-917.

(7) Snider D. E. Pyridoxine Supplementation during Isoniazid Therapy. *Tubercle.* **1980**, *61*, 191–196.

(8) Cherukuvada S. and Guru Row T. N. Comprehending the Formation of Eutectics and Cocrystals in Terms of Design and Their Structural Interrelationships. *Cryst. Growth Des.* **2014**, *14*, 4187–4198.

Chapter 6: Conclusion

A total of eight multicomponent complexes of some anti-tubercular API and B group vitamins were prepared and meticulously characterised in this study. These complexes encompassed two cocrystals, two salts, three eutectic systems and a decomposition product. The molecular structures of five of these multicomponent crystals were elucidated using single-crystal X-ray diffraction.

Cocrystal preparation and characterisation

Both mechanochemical and solvent recrystallisation methods were used to prepare the multicomponent crystals. Mechanochemical methods involved both neat grinding and liquid-assisted grinding utilising MeOH, MeCN, H_2O and EtOAc as solvents to produce the pulverized samples. Single crystals were grown by slow evaporation from MeOH, MeCN, H_2O and EtOAc.

Comprehensive characterisation of products obtained through milling and slow evaporation was conducted using FTIR, PXRD, DSC and TGA. In the case where single crystals were produced, SCXRD was used to facilitate determination of the crystal structure.

6.1. Multicomponent crystals of PAS

Crystals of PAS-INH were reliably prepared by slow evaporation from MeOH and the crystals exhibited similar characteristics to the samples produced by milling. The PXRD patterns of the ground samples and associated calculated pattern were similar, even though the ground samples also exhibited some similarity to that of the physical mixture of these compounds. The PXRD and DSC results generated in this study also matched previously reported data where relevant.[1,2] Preparation of the PAS-PYR cocrystals was met with challenges, with discrepancies noted from the reported procedures and results. Grobelny *et al.*[1] and Drozd *et al.*[2] found significantly different melting point ranges and also claimed to have prepared the cocrystals from different solvent systems of MeOH and H_2O, respectively.

PXRD analysis of the ground samples of PAS-PYR·H_2O was insufficient to infer that cocrystallisation had occurred during milling. Notwithstanding the fact that the reported procedures were used to prepare the material, the results obtained differed from the published data. Several attempts were made to prepare suitable single crystals for single-crystal X-ray diffraction analysis. There are a number of possible reasons the PAS-PYR·H_2O cocrystal was not reproducible *via* mechanochemical synthesis including different environmental conditions, grade and source of reagents used, amongst others. On-going investigations are underway to determine why it has been challenging to obtain the cocrystal.

Preparation of the multicomponent crystals of PAS and PCBA was done using mechanochemistry and solvent evaporation. All ground samples exhibited two distinct endotherms in addition to a recrystallisation exotherm during DSC analysis while the product from recrystallisation only produced a single endotherm. The PXRD profiles of the ground samples differed from the calculated PXRD profile of the recrystallised material. This outcome was expected as the PAS-PCBA compound decomposed in solution. A crystal from the melt of one of the ground samples was also isolated. The crystal structure matched that produced from solvent recrystallisation. This structure revealed that PAS had decomposed through the loss of CO_2.[3] Discrepancies in the PXRD diffractograms may be an indicator that a multicomponent material which may be either salt or cocrystal exists in the ground samples, prior to observation of the decomposition product.

6.2. Salts of PN

Two salts of PN with PAS and PCBA were prepared by neat and liquid-assisted grinding using MeOH, H_2O, EtOAc and MeCN as solvents. The combination of PN-PAS resulted in a hydrated salt and crystals of the salt where obtained from a 3:1v/v solvent mixture of EtOAc and MeOH. From the ground materials, it was observed that the LAG_{H_2O} decomposes upon dehydration, therefore, making water an unsuitable solvent for mechanochemical preparation of this salt. The crystalline sample exhibited the same thermal behaviour as the ground products. The crystal structure exhibits minor disorder of an aliphatic hydroxyl group which is related to the occupancy of the water molecule in that structure.

The PN-PCBA salt was obtained from a 3:1 v/v solvent mixture of MeCN and MeOH, and separately from a 3:1 v/v mixture of EtOAc and MeOH. As with PAS-PCBA, the ground samples of PN-PCBA exhibited two endotherms in the DSC thermogram and that for the neat grind sample revealing an additional recrystallisation exotherm. The LAG_{H_2O} sample and the crystalline material obtained from recrystallisation, however, do not exhibit the second endotherm in the DSC thermogram, which means only one phase was formed. Unlike the decomposition product reported in Chapter 3, this PCBA complex exhibits similar PXRD patterns for both the ground and bulk crystalline materials and it was confirmed that the products from recrystallisation were intact from the crystal structure. Moreover, H_2O is an optimal solvent for mechanochemical synthesis of this salt since it has a single melt endotherm in the DSC thermogram. The results of this work have highlighted that evaluation of different methods of preparation such as neat and LAG facilitates identification of the best solvent, when using a LAG approach to produce the crystals or that in some cases the use of a solvent may not be required as heating can assist in the full conversion of starting materials as observed for the NG. This provides an alternative method of synthesis that aligns with the principles of green chemistry of reducing/eradicating the use of

auxiliaries such as solvents. Speaking of principles of green chemistry, the use of heat may not necessarily be the most energy efficient method, however; there are other reaction parameters such as milling frequency or number of milling media used to ensure full conversion without heating or solvent used may also be investigated.

6.3. Eutectics of INH

The formation of materials that display eutectic properties has been shown to play a key role in increasing the aqueous solubility and dissolution rate of multiple pharmaceutical compounds, owing to the reduction in the melting point of the resultant binary mixture. Therefore, making materials that exhibit eutectic properties are helpful in solving the big problem of low solubility and dissolution of pharmaceutical products with undesirable solubility and dissolution rates. Three eutectic systems of INH with PYR, PN and PN·HCl were prepared by neat and liquid-assisted grinding. Phase diagrams were constructed using DSC data for mixtures containing the two components at various molar ratios. All three systems resulted in products with melting points below the melting point of the starting materials, which is characteristic of eutectic systems.[4] The phase diagram for INH:PYR eutectic reveals a eutectic composition at 1:1 mixture of INH and PYR, which is similar to what has been reported previously.[4]

A eutectic mixture of INH and PN has also been reported[5], however; the results obtained in this study revealed a different eutectic composition of a 1:1 mixture and further investigations are necessary to verify these results. The preparation of the compounds can be repeated to make sure results are reproducible and a different method of constructing the phase diagram can be explored to determine if different or similar results will be obtained. A eutectic mixture of INH:PN·HCl with a eutectic composition of 6:4 INH:PN·HCl was also successfully prepared. Eutectics lead to the same phase regardless of the method used to produce these *viz.*, neat or LAG.

6.4. Other combinations

Other combinations that were investigated during the course of this work but were not reported in this dissertation are listed in **Table 1**.

Table 1: Table of other combinations investigated during the conduct of this work.

Combinations	Synthesis method					Reported
	NG	LAG				
		MeOH	H_2O	MeCN	EtOAc	
PAS + iNAM	Cocrystal	Cocrystal	Cocrystal	Cocrystal	Cocrystal	Drozd *et al.*[2]
PAS + CAF	Cocrystal	Cocrystal	Cocrystal	Cocrystal	Cocrystal	Drozd *et al.*[2]
PAS + NAM	Cocrystal	Cocrystal	Cocrystal	Cocrystal	Cocrystal	Drozd *et al.*[2] Cherukuvada *et al.*[6]
PAS + 4-hydroxybenzoic acid	Additional characterisation and other investigations still required					-
PAS + isonicotinic acid						-
PAS + nicotinic acid						-
INH + PCBA						-
PCBA + iNAM						-

6.5. Suggestions for future work

Since these results suggest the presence of potentially useful combinations of pharmaceutical compounds it will be important to conduct solubility, DOSY NMR, permeability, sensitivity testing and stability studies of the salts produced to determine if the changes observed have an impact on their potential efficacy as medicines. Variable temperature PXRD analysis on the samples that exhibited multiple endotherms would highlight the impact of processing conditions on formation of these materials and monitor any phase changes that may occur. Exploration of the preparation of the multicomponent crystals using other solvents to gain a better understanding of the role of solvents in the mechanochemical preparation of cocrystals will add to the body of knowledge of these processes. Additional studies in process performance using different methods of preparation may be required to improve the % yield as efficiency of formation is required if the process is to be used commercially. It was also observed from the FTIR and PXRD data sets that in most cases the ground samples revealed the presence of some unreacted material, which was not observed in the bulk crystalline samples. Therefore, altering the reaction parameters for mechanochemical grinding, such as grinding time, frequency, volume of solvent and number of milling media used, can be done to investigate the optimum reaction conditions that will yield purer products would also be beneficial from an efficiency and cost perspective.

References

(1) Grobelny P., Mukherjee A. and Desiraju G. R. Drug-Drug Co-Crystals: Temperature-Dependent Proton Mobility in the Molecular Complex of Isoniazid with 4-Aminosalicylic Acid. *CrystEngComm* **2011**, *13*, 4358-4364.

(2) Drozd K. V., Manin A. N., Churakov A. V. and Perlovich G. L. Drug-Drug Cocrystals of Antituberculous 4-Aminosalicylic Acid: Screening, Crystal Structures, Thermochemical and Solubility Studies. *Eur. J. of Pharm. Sci.* **2017**, *99*, 228–239.

(3) Jivani S. G. and Stella V. J. Mechanism of Decarboxylation of P-Aminosalicylic Acid. *J. of Pharm. Sci.* **1985**, *74*, 1274–1282.

(4) Cherukuvada S. and Nangia, A. Fast Dissolving Eutectic Compositions of Two Anti-Tubercular Drugs. *CrystEngComm.* **2012**, *14*, 2579-2588.

(5) Ganduri R., Cherukuvada S. and Guru Row T. N. Multicomponent Adducts of Pyridoxine: An Evaluation of the Formation of Eutectics and Molecular Salts. *Cryst. Growth Des.* **2015**, *15*, 3474–3480.

(6) Cherukuvada S., Bolla G., Sikligar K. and Nangia A. 4-Aminosalicylic Acid Adducts. *Cryst. Growth Des.* **2013**, *13*, 1551–1557.

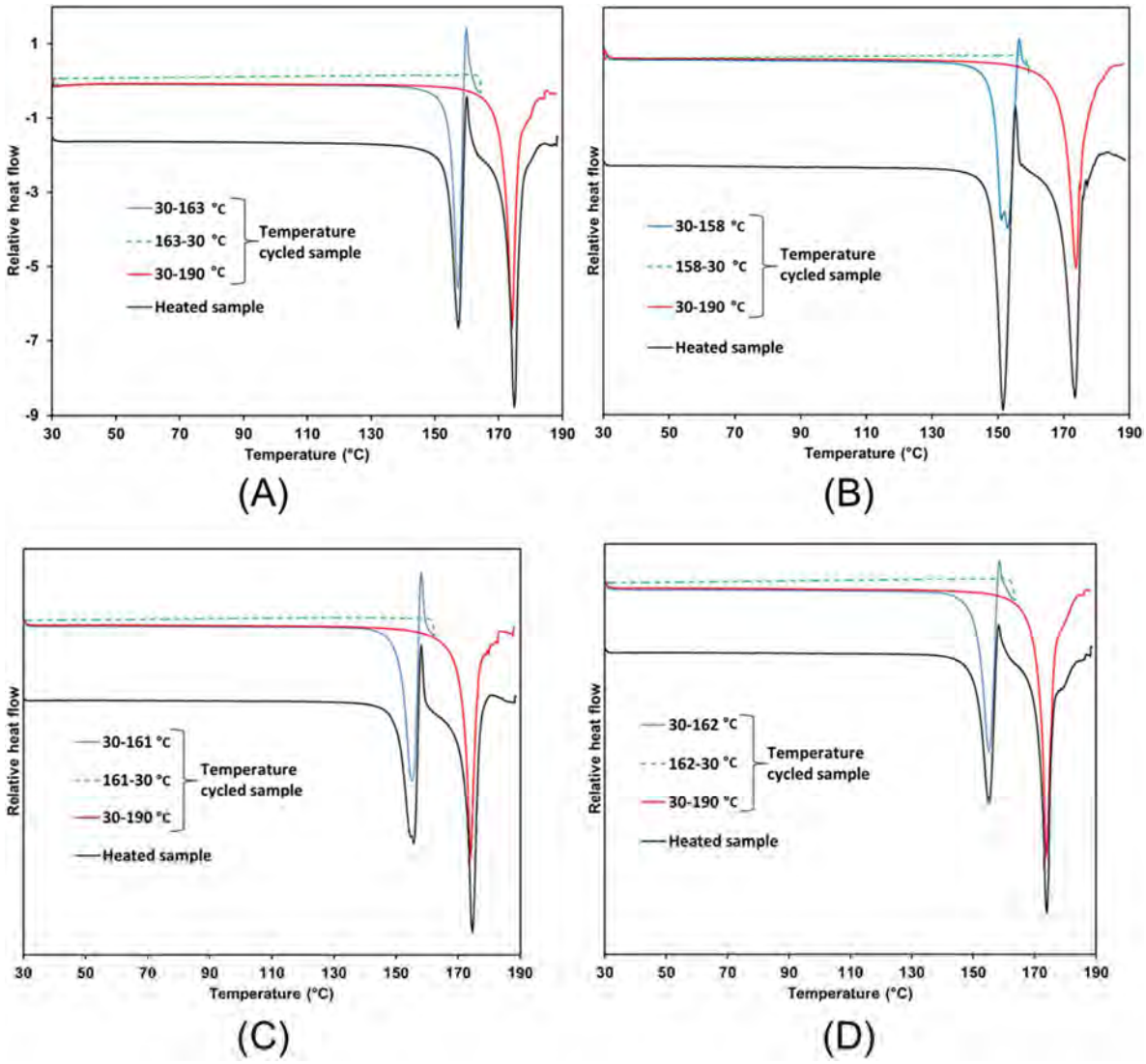

Figure 1: DSC curves for the PAS-PCBA temperature cycled samples showing recrystallization A) LAG_{EtOAc}, B) LAG_{H2O}, C) LAG_{MeCN} and D) LAG_{MeOH}

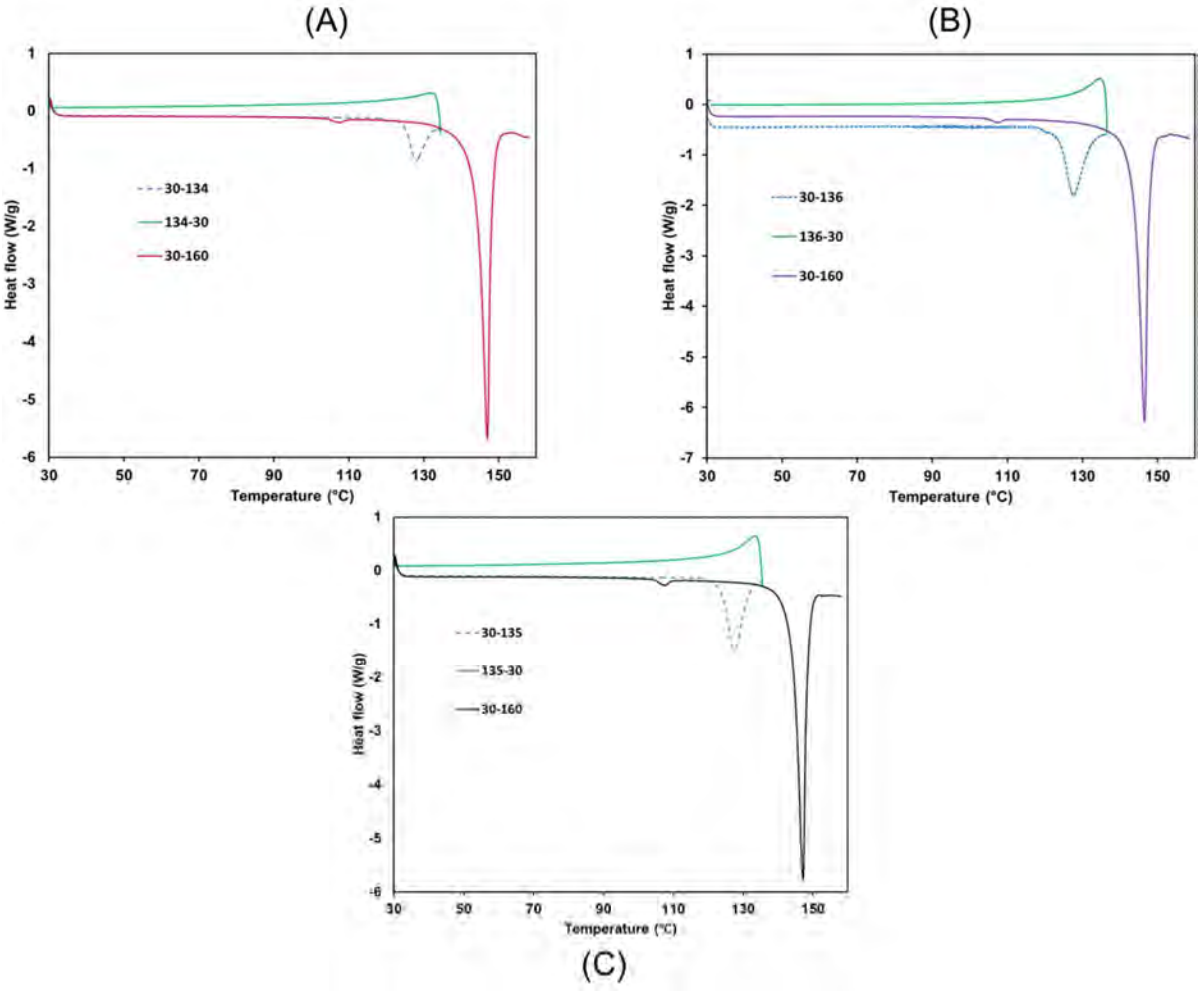

Figure 2: DSC curves for the PN-PCBA reheated samples (A) LAG_{MeOH} (B) LAG_{MeCN} (C) LAG_{EtOAc}